The Astronomical Journal, 166:198 (37pp), 2023 November https://doi.org/10.3847/1538-3881/acf768

ELemental abundances of Planets and brown dwarfs Imaged around Stars (ELPIS). I. Potential Metal Enrichment of the Exoplanet AF Lep b and a Novel Retrieval Approach for Cloudy Self-luminous Atmospheres

Zhoujian Zhang (张周健)[1,6], Paul Mollière[2], Keith Hawkins[3], Catherine Manea[3], Jonathan J. Fortney[1], Caroline V. Morley[3], Andrew Skemer[1], Mark S. Marley[4], Brendan P. Bowler[3], Aarynn L. Carter[1], Kyle Franson[3,7], Zachary G. Maas[5], and Christopher Sneden[3]
[1] Department of Astronomy & Astrophysics, University of California, Santa Cruz, CA 95064, USA
[2] Max-Planck-Institut für Astronomie, Königstuhl 17, D-69117 Heidelberg, Germany
[3] Department of Astronomy, The University of Texas at Austin, Austin, TX 78712, USA
[4] Lunar and Planetary Laboratory, University of Arizona, 1629 E. University Blvd., Tucson, AZ 85721, USA
[5] Department of Astronomy, Indiana University, Bloomington, IN 47405, USA

Received 2023 July 10; revised 2023 August 22; accepted 2023 August 31; published 2023 October 17

Abstract

AF Lep A+b is a remarkable planetary system hosting a gas-giant planet that has the lowest dynamical mass among directly imaged exoplanets. We present an in-depth analysis of the atmospheric composition of the star and planet to probe the planet's formation pathway. Based on new high-resolution spectroscopy of AF Lep A, we measure a uniform set of stellar parameters and elemental abundances (e.g., $[\mathrm{Fe/H}] = -0.27 \pm 0.31$ dex). The planet's dynamical mass ($2.8^{+0.6}_{-0.5}\ M_{\mathrm{Jup}}$) and orbit are also refined using published radial velocities, relative astrometry, and absolute astrometry. We use `petitRADTRANS` to perform chemically consistent atmospheric retrievals for AF Lep b. The radiative–convective equilibrium temperature profiles are incorporated as parameterized priors on the planet's thermal structure, leading to a robust characterization for cloudy self-luminous atmospheres. This novel approach is enabled by constraining the temperature–pressure profiles via the temperature gradient ($d \ln T / d \ln P$), a departure from previous studies that solely modeled the temperature. Through multiple retrievals performed on different portions of the 0.9–4.2 μm spectrophotometry, along with different priors on the planet's mass and radius, we infer that AF Lep b likely possesses a metal-enriched atmosphere ($[\mathrm{Fe/H}] > 1.0$ dex). AF Lep b's potential metal enrichment may be due to planetesimal accretion, giant impacts, and/or core erosion. The first process coincides with the debris disk in the system, which could be dynamically excited by AF Lep b and lead to planetesimal bombardment. Our analysis also determines $T_{\mathrm{eff}} \approx 800$ K, $\log(g) \approx 3.7$ dex, and the presence of silicate clouds and disequilibrium chemistry in the atmosphere. Straddling the L/T transition, AF Lep b is thus far the coldest exoplanet with suggested evidence of silicate clouds.

Unified Astronomy Thesaurus concepts: Exoplanet formation (492); Exoplanet atmospheres (487); Exoplanet atmospheric composition (2021); Extrasolar gaseous giant planets (509); Stellar abundances (1577)

Supporting material: figure sets

1. Introduction

Elemental abundances of exoplanets as measured from spectroscopy provide valuable insights into these planets' origins and formation processes (e.g., Marley et al. 2007a). By comparing the composition of planets to those of their host stars, we can investigate their birth location, the relative amounts of gas and dust accreted during their formation, and other phenomena such as late-stage planetesimal bombardment, pebble drift and evaporation, and core erosion (e.g., Öberg et al. 2011; Madhusudhan et al. 2014, 2017; Line et al. 2021; Schneider & Bitsch 2021a, 2021b; Mollière et al. 2022; Ohno & Fortney 2022, 2023). Our solar system serves as a convenient laboratory for contextualizing the composition of giant planets (e.g., Wong et al. 2004; Alibert et al. 2005; Fletcher et al. 2009; Fortney & Nettelmann 2010; Helled & Bodenheimer 2014). Such analysis has been also expanded to extrasolar planets as pioneered by Öberg et al. (2011), who used the carbon-to-oxygen ratio (C/O) as a metric to probe the planets' formation pathways.

Measurements of C/O and/or the bulk metallicity have been established for several directly imaged exoplanets, including β Pic b (e.g., GRAVITY Collaboration et al. 2020), YSES-1 b (e.g., Zhang et al. 2021b), HR 8799 bcde (e.g., Konopacky et al. 2013; Lavie et al. 2017; Mollière et al. 2020; Wang et al. 2020, 2023; Ruffio et al. 2021), GJ 504 b (e.g., Skemer et al. 2016), and 51 Eri b (e.g., Rajan et al. 2017; Samland et al. 2017; Brown-Sevilla et al. 2023; Whiteford et al. 2023). Similar measurements have been also made for substellar companions and free-floating brown dwarfs (e.g., Line et al. 2015, 2017; Zalesky et al. 2019; Burningham et al. 2021; Gonzales et al. 2021, 2022; Zhang et al. 2021a; Wang et al. 2022; Xuan et al. 2022; Zalesky et al. 2022), as well as for irradiated exoplanets (e.g., Line et al. 2021; Changeat et al. 2022; Fu et al. 2022; Ahrer et al. 2023; August et al. 2023; Boucher et al. 2023; Brogi et al. 2023; Finnerty et al. 2023). C/O is a popular abundance metric since the dominant oxygen

---

[6] NASA Sagan Fellow.
[7] NSF Graduate Research Fellow.

and carbon reservoirs, including H_2O, CO, CO_2, and CH_4, are also the main opacity sources in planetary atmospheres. Beyond C/O, other abundance ratios have also been suggested as robust tracers of planet formation, including the nitrogen-to-oxygen ratio and the refractory-to-volatile ratio (e.g., Piso et al. 2016; Cridland et al. 2020; Lothringer et al. 2021; Schneider & Bitsch 2021b; Mollière et al. 2022; Ohno & Fortney 2022, 2023). Ultimately, combining all these elemental abundance metrics will provide a more comprehensive understanding of planet formation.

To further our understanding of atmospheric composition and its diversity in the planet and star formation process, we are launching the ELemental abundances of Planets and brown dwarfs Imaged around Stars (ELPIS) program. This program aims to measure the composition of directly imaged planets, brown dwarf companions, and all their host stars through spectroscopy. By exploring the planet-to-star relative abundance as a function of planet mass (e.g., Miller & Fortney 2011; Thorngren et al. 2016; Thorngren & Fortney 2019; Hoch et al. 2023) and orbital separation, we aim to probe the dominant formation mechanisms in different planet mass regimes and birth locations within protoplanetary disks. The existing census of directly imaged exoplanets, as defined by the inclusion criteria of our program, contains about three dozen objects. Looking forward, this list of discoveries is expected to rapidly expand, particularly with the contributions from the Gaia mission (Gaia Collaboration et al. 2016). The use of the astrometric acceleration, or proper-motion anomaly, detected by the long-baseline astrometry from Hipparcos and Gaia has proven to be an efficient method for identifying parent stars of giant planets as compared to blind direct imaging surveys (Brandt 2018, 2021; Kervella et al. 2019, 2022). Recently, this method has led to new discoveries of imaged exoplanets and brown dwarfs (e.g., Bowler et al. 2021; Bonavita et al. 2022; Kuzuhara et al. 2022; Currie et al. 2023; Franson et al. 2023a).

One of the most recent exoplanet discoveries driven by astrometric acceleration is AF Lep b, which orbits the late-F star AF Lep A. This system was independently discovered by three groups (De Rosa et al. 2023; Franson et al. 2023b; Mesa et al. 2023). Using their own astrometry and spectrophotometry observed at different dates, these studies constrained the dynamical mass of the planet to a range of about 3–5 $M_{\rm Jup}$ and determined an orbital semimajor axis of 8–9 au. AF Lep b is the lowest-mass imaged exoplanet with a dynamical mass measurement to date. The AF Lep system is part of the β Pic young moving group with an estimated age of 24 ± 3 Myr (e.g., Bell et al. 2015). The system also hosts a debris disk located at 40–60 au (Pawellek et al. 2021; Pearce et al. 2022), resembling the Kuiper Belt of the solar system.

AF Lep b's dynamical mass and its host star's elemental abundance and age will provide key context for interpreting the emission spectrophotometry of the planet. Therefore, as the first target in the ELPIS program, the AF Lep system allows for a detailed study of the planet's atmospheric properties and formation history. We first describe our high-resolution spectroscopic observations of the host star AF Lep A (Section 2), followed by a uniform analysis of the stellar parameters and elemental abundances (Section 3). Combining published radial velocities (RVs), relative astrometry, absolute astrometry, and our newly measured stellar mass, we refine the dynamical mass of AF Lep b to $2.8^{+0.6}_{-0.5}$ $M_{\rm Jup}$ and update its orbital parameters (Section 4). With the atmospheric properties of AF Lep b contextualized by evolution models (Section 5), we then perform a retrieval analysis to determine the planet's key properties, including [Fe/H] and C/O (Sections 6 and 7). We also introduce a novel retrieval approach that can enable a robust characterization of self-luminous atmospheres, especially those shaped by clouds. Implications of our analysis are discussed in Section 8, followed by a summary in Section 9.[8]

2. Data

2.1. High-resolution Spectroscopy of the Host Star AF Lep A

We acquired optical (3800–8800 Å) spectra of AF Lep A on 2023 February 24 UT from the 2.7 m Harlan J. Smith Telescope at McDonald Observatory. The Tull Echelle Spectrograph was utilized in the TS23 mode with slit plug #4, leading to a spectral resolution of R ∼60,000. The instrument's encoders were configured to ensure the spectral lines of interest (e.g., the atomic lines of H, C, O, Mg, Si, and Li) fell within the detector's field of view. Calibration frames, including biases, flats, and thorium–argon lamp data, were collected at the beginning of the night. The data reduction followed the standard procedures, including bias subtraction, flat-fielding, bad-pixel masking, cosmic-ray removal (via `DCR` by Pych 2004), scattered light subtraction, and optimal spectral extraction. We normalized the continuum of each order assuming a second-order Chebyshev polynomial and then shifted the order-stitched spectrum to the stellar rest frame by cross-correlating it with a solar spectral template using `iSpec` (Blanco-Cuaresma et al. 2014; Blanco-Cuaresma 2019).

2.2. Published Spectrophotometry of the Exoplanet AF Lep b

The near-infrared spectra of AF Lep b were collected from Mesa et al. (2023) and De Rosa et al. (2023). Both studies used the VLT/SPHERE integral field spectrograph (IFS; Claudi et al. 2008). Mesa et al. (2023) observed the planet on two different dates: 2022 October 16 UT and 2022 December 20 UT. Their data were reduced through the SPHERE data center (Delorme et al. 2017), leading to an epoch-averaged spectrum spanning 0.94–1.65 μm ($R \sim 30$). De Rosa et al. (2023) observed AF Lep b on 2022 October 20 UT. They reduced data using `pyKLIP` (Wang et al. 2015) and extracted the spectrum over 1.24–1.65 μm ($R \sim 30$). Both studies also obtained the $K1$ (2.11 μm) and $K2$ (2.25 μm) photometry using the Infra-red Dual-beam Imager and Spectrograph (IRDIS; Dohlen et al. 2008) on the same nights of their IFS observations. In addition, Franson et al. (2023b) observed AF Lep b using the Keck/NIRC2 camera on 2021 December 21 UT and 2023 February 3 UT. They obtained L'-band (3.72 μm) photometry during these two epochs.

Figure 1 summarizes all the published spectrophotometry of AF Lep b, including two spectra, three sets of $K1/K2$ photometry, and two sets of L' photometry. It is notable that the fluxes of the two SPHERE/IFS spectra differ, with a reduced $\chi^2 = 3.2$ if their flux difference is assumed to be zero. In other words, the De Rosa et al. (2023) spectrum is approximately 1.9 times brighter than the Mesa et al. (2023)

---

[8] Throughout this work, we use subscripts "A" and "b" for physical and orbital properties of the host star and the planet, respectively, only in Sections 3–4. For the remaining sections, the physical properties refer to AF Lep b unless otherwise noted.

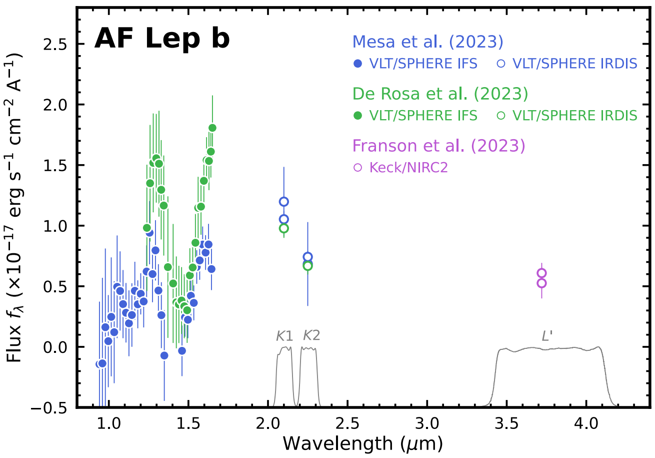

Figure 1. Spectrophotometry of AF Lep b from Mesa et al. (2023; blue), De Rosa et al. (2023; green), and Franson et al. (2023b; purple). Photometry is converted from magnitudes into fluxes (unless already reported in the literature as such) based on zero-points provided by Nielsen et al. (2017). Response curves of the $K1/K2/L'$ bands (gray) are obtained from the VLT/SPHERE and Keck/NIRC2 websites.

spectrum in overlapping wavelengths.[9] In contrast, the planet's $K1/K2/L'$ photometry from SPHERE/IRDIS and Keck/NIRC2, observed on different dates and processed by different pipelines, is consistent with each other within uncertainties.

The discrepant spectral fluxes of AF Lep b could potentially be attributed to atmospheric variability, which is common for young, low-gravity imaged planets and brown dwarfs (e.g., Zhou et al. 2016; Vos et al. 2019, 2022; Zhou et al. 2022). Variability tends to have a stronger impact on fluxes at shorter wavelengths. However, Mesa et al. (2023) measured the planet's photometry in the J and H bands by using their IFS data collected over two epochs (see their Table 4) and found that these photometric data are consistent within the uncertainties. In addition, the photometric measurements of AF Lep b in the $K1$, $K2$, and L' bands over multiple epochs show consistency (Figure 1). Therefore, the variability scenario cannot be confirmed based on the currently available data. Dedicated spectrophotometric monitoring of AF Lep b is warranted to investigate its top-of-atmosphere inhomogeneity.

An alternative explanation for the discrepant spectral fluxes could be the systematic differences in data reduction procedures between Mesa et al. (2023) and De Rosa et al. (2023). Speckle subtraction and flux calibration are both key sources of systematics in the resulting emission spectra of imaged planets. Negative or positive speckle residuals near the location of planet detection can contribute an additive offset to the spectrum, while uncertainties in the calibration of the planet's flux relative to the host star's flux can contribute a multiplicative scaling factor. The scaling factor of 1.9 between the two IFS spectra of AF Lep b suggests large calibration systematics of 90%, indicating that flux calibration might not be the primary source of the discrepancy. In addition, De Rosa et al. (2023) mentioned the presence of strong negative speckle residuals near AF Lep b in their reduced data and they suspected that these speckle-noise artifacts are responsible for the discrepant planet astrometry measured from their own IFS and IRDIS data. The negative speckle residuals might also lead to overestimated spectral fluxes. Moreover, it is worth noting that Mesa et al. (2023) performed spectral differential imaging (SDI), while De Rosa et al. (2023) deliberately skipped this procedure. SDI can introduce striping patterns that affect the extracted emission spectrum (e.g., Figure 1 of Mesa et al. 2023).

In our work, we assume that the discrepant IFS spectral fluxes between Mesa et al. (2023) and De Rosa et al. (2023) are impacted by the speckle residuals and SDI systematics. When combining both spectra for the subsequent atmospheric retrievals of AF Lep b, we incorporate an additive flux offset as a free parameter for each spectrum. We also perform retrievals for individual spectra, without incorporating any flux offsets. As discussed in Section 8.1.1, retrievals on different sets of spectra (the Mesa et al. 2023 spectrum, the De Rosa et al. 2023 spectrum, or both spectra combined by offsets) consistently predict a metal-enriched atmosphere of AF Lep b.

3. Stellar Parameters and Elemental Abundances of AF Lep A

3.1. Initial Spectroscopic Analysis

We measure the stellar parameters of AF Lep A, including its effective temperature $T_{\mathrm{eff,A}}$, surface gravity $\log(g_{\mathrm{A}})$,[10] iron abundance $[\mathrm{Fe/H}]_{\mathrm{A}}$, microturbulent velocity ξ_{A}, and spectral broadening (induced by the projected rotational velocity $v \sin i_{\star}$, macroturbulent velocity, and instrumental broadening). This measurement is established by analyzing the Tull spectrum of the host star using the Brussels Automatic Code for Characterizing High accUracy Spectra (`BACCHUS`; Masseron et al. 2016). The setup of `BACCHUS` and our spectral analysis follow Hawkins et al. (2020).

`BACCHUS` derives stellar atmospheric parameters using the standard excitation/ionization balance technique. This technique determines the effective temperature by ensuring that there is no correlation between the excitation potential of absorption features and their measured abundances. In addition, the surface gravity is constrained by balancing the abundances of Fe I and Fe II (i.e., ionization balance). The microturbulence velocity is derived by verifying there is no correlation between the abundance of Fe I and its reduced equivalent width (i.e., the equivalent width divided by the wavelength). The spectral broadening is constrained by ensuring that the Fe abundances derived by the equivalent widths (which are insensitive to the broadening effect) are consistent with those derived using the line core (which is sensitive to the broadening). The abundances of individual Fe lines are derived using both equivalent widths and χ^2 minimization between the observed spectrum and spectral synthesis. `BACCHUS` employs the `TURBOSPECTRUM` (Plez 2012) code for spectral synthesis, assuming local thermodynamic equilibrium and adopting the MARCS model atmosphere (Gustafsson et al. 2008).

The fifth version of the Gaia-ESO atomic line list (Heiter et al. 2021) is used in `BACCHUS`. Hyperfine-structure splitting is included for Sc I, V I, Mn I, Co I, Cu I, Ba II, Eu II, La II, Pr II, Nd II, and Sm II (see more details in Heiter et al. 2021). We also include the molecular line lists for CH (Masseron et al. 2014), SiH (from the Kurucz line lists[11]), and CN, NH, OH, MgH, and C_2 (T. Masseron, private communication).

---

[9] This scaling factor $k = 1.9$ was calculated by minimizing the χ^2 metric $\sum_{i=1}^{N_{\mathrm{pix}}}(f_{i,\mathrm{D}} - kf_{i,\mathrm{M}})^2 \big/ (\sigma_{i,\mathrm{D}}^2 + k^2\sigma_{i,\mathrm{M}}^2)$. The f_i and σ_i represent the spectral flux and uncertainty in a given pixel i (N_{pix} is the total number of pixels of the overlapping wavelengths), with subscripts "D" and "M" for the data set of De Rosa et al. (2023) and Mesa et al. (2023), respectively.

[10] Throughout this manuscript, we use "log()" and "ln()" for 10-based and natural logarithm, respectively.

[11] http://kurucz.harvard.edu/linelists/linesmol/

AF Lep A has a high rotational velocity ($v\sin i_\star$ of 50–55 km s^{-1}; e.g., Glebocki & Gnacinski 2005; Valenti & Fischer 2005; White et al. 2007; Schröder et al. 2009; Marsden et al. 2014; Zúñiga-Fernández et al. 2021). The stellar rotation period is $P_{\mathrm{rot}} = 1.007 \pm 0.009$ days (Franson et al. 2023b; also see Järvinen et al. 2015; De Rosa et al. 2023), which falls on the short-period end of the distribution of late-F stars (e.g., McQuillan et al. 2014). The fast rotation leads to line broadening and blending of spectral features, particularly for Fe I, Fe II, and other species of interest. This effect reduces the number of high-quality spectral lines available in our analysis. Therefore, our initial spectral analysis based on `BACCHUS` leads to stellar parameters with compromised precision, including an effective temperature of 5917 ± 259 K, a logarithmic surface gravity of 4.1 ± 0.7 dex, and an iron abundance of -0.25 ± 0.20 dex. To further improve the precision of these stellar parameters, we feed these initial spectroscopic $T_{\mathrm{eff,A}}$, $\log(g_{\mathrm{A}})$, and $[\mathrm{Fe/H}]_{\mathrm{A}}$ into the subsequent isochrone analysis (Section 3.2) to derive the adopted stellar properties. The results from the isochrone analysis are then used to refine and constrain the abundances of Fe and other elements (Section 3.3).

Table 1
Properties of AF Lep A

Parameter	Value	Reference
Spectral Type	F8	Gray06
Age (Myr)	24 ± 3	Bell15
	Astrometric Properties	
R.A.	05:27:04.78	Gaia16, Gaia22
Decl.	−11:54:04.26	Gaia16, Gaia22
Parallax[a] (mas)	37.254 ± 0.020	Gaia16, Gaia22
Distance (pc)	26.825 ± 0.014	Bail21
	Photometric Properties	
Tycho B (mag)	6.944 ± 0.015	Høg00
Tycho V (mag)	6.358 ± 0.010	Høg00
Hipparcos H_{p} (mag)	6.421 ± 0.002	Ande12
DR2 G (mag)	6.1803 ± 0.0008	Gaia16, Gaia18
DR2 BP (mag)	6.501 ± 0.003	Gaia16, Gaia18
DR2 RP (mag)	5.755 ± 0.002	Gaia16, Gaia18
2MASS J (mag)	5.268 ± 0.027	Cutr03
2MASS H (mag)	5.087 ± 0.026	Cutr03
2MASS K_{s} (mag)	4.926 ± 0.021	Cutr03
$W1$ (mag)	4.915 ± 0.179	Cutr14
$W2$ (mag)	4.783 ± 0.060	Cutr14
	Physical Properties	
T_{eff} (K)	5997 ± 147	This Work
$\log(g)$ (dex)	4.30 ± 0.05	This Work
M ($M_\odot$)	1.09 ± 0.06	This Work
R ($R_\odot$)	1.21 ± 0.06	This Work
$\log(L_{\mathrm{bol}}/L_\odot)$ (dex)	0.235 ± 0.010	This Work
ξ (km s^{-1})	2.2 ± 0.3	This Work
$v\sin(i_\star)$ (km s^{-1})	<61.5	This Work
	Elemental Abundances	
[Fe/H] (dex)	-0.27 ± 0.31	This Work
[Mg/H] (dex)	-0.11 ± 0.21	This Work
[Ca/H] (dex)	-0.32 ± 0.26	This Work

References. Høg00: Høg et al. (2000); Cutr03: Cutri et al. (2003); Gray06: Gray et al. (2006); Ande12: Anderson & Francis (2012); Cutr14: Cutri et al. (2021); Bell15: Bell et al. (2015); Gaia16: Gaia Collaboration et al. (2016); Gaia18: Gaia Collaboration et al. (2018); Bail21: Bailer-Jones et al. (2021); Gaia22: Gaia Collaboration et al. (2023).

[a] This parallax is the reported value in Gaia DR3. In our isochrone analysis (Section 3.2), we apply a zero-point of −0.024 mas and inflate its uncertainty by 30%.

3.2. Isochrone Analysis

We combine the spectroscopic $T_{\mathrm{eff,A}}$, $\log(g_{\mathrm{A}})$, and $[\mathrm{Fe/H}]_{\mathrm{A}}$ (from Section 3.1) with the broadband photometry and parallax of AF Lep A and model them using `isochrones` (Morton 2015). The MESA Isochrones and Stellar Tracks (MIST; Choi et al. 2016; Dotter 2016) are used. To construct the spectral energy distribution (SED) of AF Lep A, we collect its optical and infrared photometry from Tycho-2 (Høg et al. 2000), Hipparcos (Anderson & Francis 2012), Gaia DR2 (Gaia Collaboration et al. 2016, 2018), the Two Micron All Sky Survey (2MASS; Cutri et al. 2003), and AllWISE (Cutri et al. 2021). $W3$ and $W4$ from AllWISE are excluded to avoid contaminating flux from the debris disk in the same planet system (see Figure 1 of Pawellek et al. 2021). We adopt a photometric uncertainty floor of 0.03 mag if the reported magnitude in a given band is more precise, in order to account for any external calibration uncertainties of observed photometry, as well as systematic errors of synthetic photometry by `isochrones` (also see Anders et al. 2019; Fouesneau et al. 2022). The filter response curves of the G/BP/RP photometry and the G-band magnitude calibration are all from Maíz Apellániz & Weiler (2018). The parallax is taken from Gaia DR3 (Gaia Collaboration et al. 2016, 2023), with its uncertainty inflated by 30% (e.g., Brandt 2021; El-Badry et al. 2021; Fabricius et al. 2021; Zinn 2021) and the zero-point computed via `gaiadr3-zeropoint` (Lindegren et al. 2021).

We feed the spectroscopic $T_{\mathrm{eff,A}}$, $\log(g_{\mathrm{A}})$, and $[\mathrm{Fe/H}]_{\mathrm{A}}$, photometry, and parallax of AF Lep A into `isochrones`. This analysis infers the age, distance, equivalent evolutionary point, stellar mass (M_{A}), radius (R_{A}), and bolometric luminosity ($L_{\mathrm{bol,A}}$), and also refines the $T_{\mathrm{eff,A}}$, $\log(g_{\mathrm{A}})$, and $[\mathrm{Fe/H}]_{\mathrm{A}}$ obtained from the initial spectroscopic analysis. We fix the V-band extinction at zero. Beyond the default parameter priors set in `isochrones`, we adopt a log-uniform prior for the age parameter, over the 3σ confidence interval of the β Pic moving group's age of 24 ± 3 Myr (Bell et al. 2015). The `isochrones` code employs `PyMultiNest` (Feroz & Hobson 2008; Feroz et al. 2009, 2019; Buchner et al. 2014) and we set 10^4 live points to sample the parameter posteriors. Systematic uncertainties of 2.4% in $T_{\mathrm{eff,A}}$, 5% in M_{A}, and 2% in $L_{\mathrm{bol,A}}$ are incorporated as additional Gaussian noise into the derived stellar parameters, following suggestions by Tayar et al. (2022). We then recompute R_{A} and $\log(g_{\mathrm{A}})$ from the modified ($T_{\mathrm{eff,A}}$, $L_{\mathrm{bol,A}}$) and (M_{A}, R_{A}) posteriors, respectively.

This isochrone analysis provides a uniform set of stellar parameters for AF Lep A, with the adopted values and uncertainties summarized in Table 1. As discussed in Appendix A, our estimated stellar properties (particularly $[\mathrm{Fe/H}]_{\mathrm{A}}$) are consistent with those derived by previous work.

3.3. Elemental Abundances

To measure the elemental abundances of AF Lep A, the isochrone-based $T_{\mathrm{eff,A}}$ and $\log(g_{\mathrm{A}})$ (from Section 3.2) are used as input for `BACCHUS` to reanalyze the Tull spectrum. This analysis refines the $[\mathrm{Fe/H}]_{\mathrm{A}}$, microturbulent velocity, and spectral broadening (providing an upper limit for $v \sin i_{\star}$); also, the abundances of individual species, including C, O, Mg, Si, and Ca, are measured. For each spectral absorption feature of each element, we create a set of synthetic spectra corresponding to various [X/Fe] abundances spanning −0.6 dex to +0.6 dex. A χ^2 minimization is then performed between the observed and synthetic spectra. Our reported stellar [X/H] values are the median of the derived [X/H] across all lines for a given species. The uncertainty of [X/H] is taken as the dispersion in this ratio across all lines. If only one absorption line is used, we conservatively assume an [X/Fe] uncertainty of 0.10 dex.

We also determine the propagated uncertainty in [X/H] due to the uncertainties of the stellar effective temperature, surface gravity, and microturbulent velocity. Specifically, we perturb $T_{\mathrm{eff,A}}$, $\log(g_{\mathrm{A}})$, and ξ_{A} one at a time by their 1σ uncertainties listed in Table 1 and redetermine [X/H]. Changes in abundances due to these perturbations allow us to determine the uncertainty in [X/H] due to the uncertainties of the stellar parameters. We find that the uncertainty in [Fe/H] is ±0.08 dex, ±0.04 dex, and ±0.05 dex for perturbations of $\Delta T_{\mathrm{eff,A}} = 150$ K, $\Delta \log(g_{\mathrm{A}}) = 0.05$ dex, and $\Delta\xi = 0.30$ km s^{-1}, respectively. Furthermore, for perturbations in $T_{\mathrm{eff,A}}$, $\log(g_{\mathrm{A}})$, and ξ at the same level listed above, we find that the uncertainty in [Mg/H] is ±0.20 dex, ±0.02 dex, and ±0.06 dex, respectively; the uncertainty in [Ca/H] is ±0.16 dex, ±0.02 dex, and ±0.07 dex, respectively. Thus, we incorporate in quadrature an additional uncertainty of 0.08 dex in [Fe/H], 0.20 dex in [Mg/H], and 0.16 dex in [Ca/H].

Due to the rotational broadening in the stellar spectrum, the abundances of C, O, and Si cannot be reliably measured. Therefore, the stellar C/O is not determined. We are able to constrain the abundances of Fe, Mg, and Ca, as listed in Table 1.

4. Refined Dynamical Mass and Orbit of AF Lep b

The dynamical mass of AF Lep b provides key constraints on this planet's atmospheric properties (see Section 7). However, previous orbit analyses of this planetary system have led to different mass estimates, including $4.3^{+2.9}_{-1.2}$ M_{Jup} by De Rosa et al. (2023), $3.2^{+0.7}_{-0.6}$ M_{Jup} by Franson et al. (2023b), and $5.24^{+0.09}_{-0.10}$ M_{Jup} by Mesa et al. (2023). This discrepancy occurred mainly because the relative astrometry used in these studies was measured at different epochs over different baselines. Here we combine all published relative RVs of the host star and the relative and absolute astrometry of the system, as well as our newly measured stellar mass (Section 3), to provide the latest updates to the dynamical mass and orbit of AF Lep b.

4.1. RVs, Relative Astrometry, and Absolute Astrometry

We obtain all 20 epochs of RVs of AF Lep A measured by Butler et al. (2017) using Keck/HIRES. Among these RVs, 6 and 14 epochs were observed before and after the HIRES CCD upgrade on 2004 August 18 UT, respectively. These two sets of RV measurements are thus treated as measurements from separate instruments.[12] The pre-upgrade RVs span 1.1 yr, with a linear trend of 149 ± 50 m s^{-1} yr^{-1} and an rms of 100 m s^{-1}. The post-upgrade RVs span 9.1 yr, with a linear trend of -14 ± 5 m s^{-1} yr^{-1} and an rms of 162 m s^{-1}. De Rosa et al. (2023) also measured the RVs of AF Lep A using the ARC Echelle Spectrograph at Apache Point Observatory over five epochs in late 2022. These latest RVs have a typical uncertainty (≈1.2 km s^{-1}) that is about 20 times larger than that of Keck/HIRES measurements (≈62 m s^{-1}), and are thus excluded in our analysis.

For the relative astrometry between the A and b components, we collect all individual measurements by Franson et al. (2023b), De Rosa et al. (2023), and Mesa et al. (2023) based on VLT/SPHERE and Keck/NIRC2, spanning a baseline of 1.1 yr. The orbital motion of AF Lep b is demonstrated by its increasing position angle with a rate of $6\overset{\circ}{.}8 \pm 1\overset{\circ}{.}2$ yr^{-1}, although this planet's angular separation from its host star remains nearly constant during the monitoring (with a slope of -2 ± 10 mas yr^{-1}). There is also a significant difference between the Gaia and the joint Hipparcos–Gaia long-term proper motions of AF Lep A (the reduced χ^2 is 77 for a constant-proper-motion model; Brandt 2021), suggesting this star has an astrometric acceleration of 2.5 ± 0.3 m s^{-1} yr^{-1} caused by the planet's gravitational perturbation.

4.2. Orbit Analysis

We use `orvara` (Brandt et al. 2021) to constrain the dynamical mass and orbit of AF Lep b by fitting all available RVs, relative astrometry, and absolute astrometry (Section 4.1). There are 15 free parameters in our orbit analysis: the mass of the host star (M_{A}), the dynamical mass of the planet (M_{b}), the semimajor axis of the planetary system (a), eccentricity (e_{b}), inclination (i_{b}), the position angle of the ascending node of the planet's orbit (Ω_{b}), the argument of the periastron of the host star's orbit ($\omega_{\star}$), the mean longitude of the host star's orbit at epoch J2010.0 ($\lambda_{\mathrm{ref},\star}$), the marginalized parallax (ϖ) and proper motion ($\mu_{\alpha}\cos(\delta)$ and μ_{δ}) of the system, and the zero-points (ZP) and jitter terms (σ_{jit}) for the pre- and post-upgrade Keck/HIRES RV measurements. The adopted priors for these parameters are summarized in Table 2. In particular, we assume a Gaussian prior for M_{A}, with the mean and standard deviation being $1.09 \pm 0.06\,M_{\odot}$ based on the stellar analysis (Section 3.2).

This analysis employs the parallel-tempering Markov Chain Monte Carlo (MCMC) sampler (Foreman-Mackey et al. 2013; Vousden et al. 2016). We run the MCMC with 50 temperatures and 100 walkers over 5×10^5 steps. Chains are saved every 50 steps, and the first 5000 samples from each walker of the thinned chains are removed as burn-in.

The resulting orbital solution for AF Lep b is bimodal due to the lack of information about the orbital RV of the planet, i.e., the relative RV between the planet and the host star $\Delta RV_{\mathrm{b-A}} \equiv RV_{\mathrm{b}} - RV_{\mathrm{A}}$ (e.g., Pearce et al. 2020; Do et al. 2023; Zhang et al. 2023). We compute $\Delta RV_{\mathrm{b-A}}$ at a reference epoch J2024.0 based on the MCMC chains and the following equation:

$$\Delta RV_{\mathrm{b-A,ref}} = -\frac{2\pi \sin i \sqrt{M_{\mathrm{A}} + M_{\mathrm{b}}}}{\sqrt{a(1-e^2)}} \times [\cos(\nu_{\mathrm{ref}} + \omega_{\star}) + e\cos(\omega_{\star})] \quad (1)$$

where ν_{ref} is the true anomaly of the planet at epoch J2024.0. The inferred orbital parameters can be divided into two subsets corresponding to positive and negative $\Delta RV_{\mathrm{b-A,ref}}$ values. The

---

[12] These RVs were treated as having been derived from the same instrument in previous studies of AF Lep, although our orbit analysis implies that relative RVs alone do not provide tight constraints on the orbital architecture of this system.

Table 2
Orbit Analysis of AF Lep

Parameter[a]	Unit	Median $\pm 1\sigma$	2σ Confidence Interval	Adopted Prior
Fitted Parameters				
Mass of AF Lep A M_A	$M_\odot$	$1.09^{+0.07}_{-0.07}$	(0.94, 1.23)	$\mathcal{N}(\mu = 1.07, \sigma^2 = 0.06^2)$
Mass of AF Lep b M_b	$M_{\rm Jup}$	$2.8^{+0.6}_{-0.5}$	(1.8, 4.1)	$1/M$ (log-flat)
Semimajor axis a	au	$8.2^{+1.3}_{-1.7}$	(5.8, 11.6)	$1/a$ (log-flat)
$\sqrt{e_b}\,\sin\omega_\star$	…	$0.04^{+0.55}_{-0.62}$	(-0.82, 0.82)	Uniform
$\sqrt{e_b}\,\cos\omega_\star$	…	$0.03^{+0.38}_{-0.38}$	(-0.68, 0.67)	Uniform
Inclination i_b	deg	55^{+8}_{-13}	(26, 69)	$\sin(i)$ with $i \in [0, 180°]$
PA of the ascending node[b] Ω_b				
Ω_b component 1 ($\Delta RV_{b-A,\rm ref} > 0$)	deg	243^{+18}_{-26}	(182, 333)	Uniform
Ω_b component 2 ($\Delta RV_{b-A,\rm ref} < 0$)	deg	63^{+16}_{-28}	(-1, 168)	Uniform
Mean longitude at J2010.0[b] $\lambda_{\rm ref,\star}$				
$\lambda_{\rm ref,\star}$ component 1 ($\Delta RV_{b-A,\rm ref} > 0$)	deg	340^{+41}_{-100}	(177, 416)	Uniform
$\lambda_{\rm ref,\star}$ component 2 ($\Delta RV_{b-A,\rm ref} < 0$)	deg	165^{+36}_{-104}	(-35, 231)	Uniform
Parallax ϖ	mas	$37.25^{+0.02}_{-0.02}$	(37.21, 37.29)	$\mathcal{N}(\mu = 37.254, \sigma^2 = 0.019^2)$
System barycentric proper motion in R.A. $\mu_\alpha \cos(\delta)$	mas yr^{-1}	$17.11^{+0.03}_{-0.03}$	(17.05, 17.17)	Uniform
System barycentric proper motion in decl. μ_δ	mas yr^{-1}	$-49.19^{+0.03}_{-0.03}$	(-49.24, -49.13)	Uniform
RV jitter for pre-upgrade HIRES $\sigma_{\rm jit,pre-HIRES}$	m s^{-1}	124^{+67}_{-43}	(38, 320)	$1/\sigma_{\rm jit,pre-HIRES}$ (log-flat)
RV zero-point for pre-upgrade HIRES ZP$_{\rm pre-HIRES}$	m s^{-1}	-143^{+11}_{-11}	(-164, -121)	Uniform
RV jitter for post-upgrade HIRES $\sigma_{\rm jit,post-HIRES}$	m s^{-1}	168^{+46}_{-33}	(109, 280)	$1/\sigma_{\rm jit,pre-HIRES}$ (log-flat)
RV zero-point for post-upgrade HIRES ZP$_{\rm post-HIRES}$	m s^{-1}	64^{+12}_{-15}	(45, 80)	Uniform
Derived Parameters				
Eccentricity e_b	...	$0.4^{+0.3}_{-0.2}$	(0.0, 0.8)	…
Period P_b	yr	$22.3^{+5.6}_{-6.7}$	(13.4, 38.3)	…
Argument of periastron[b] $\omega_\star$				
$\omega_\star$ component 1 ($\Delta RV_{b-A,\rm ref} > 0$)	deg	50^{+45}_{-85}	(-92, 131)	…
$\omega_\star$ component 2 ($\Delta RV_{b-A,\rm ref} < 0$)	deg	231^{+44}_{-85}	(65, 306)	…
Time of periastron[c] T_0	JD	$2, 456, 906^{+720}_{-358}$	(2,455,810, 2,462,691)	…
Periastron separation $a_b(1 - e_b)$	au	$5.3^{+2.3}_{-2.7}$	(1.4, 9.0)	…

Notes.

[a] Orbital parameters all correspond to the orbit of AF Lep b except for a, $\omega_\star$, and $\lambda_{\rm ref,\star}$. The first parameter a corresponds to the system's (instead of the individual components') semimajor axis, and the latter two parameters correspond to the orbit of the host star AF Lep A.

[b] Posteriors of Ω, $\lambda_{\rm ref,\star}$, and $\omega_\star$ are bimodal. We divide each parameter posterior into two components, each corresponding to a positive or a negative $\Delta RV_{b-A,\rm ref}$. Here $\Delta RV_{b-A,\rm ref}$ denotes the relative RV between the exoplanet and its host star at epoch 2024.0. The parameter confidence interval of each component is reported separately.

[c] T_0 is computed as $t_{\rm ref} - P \times (\lambda_{\rm ref,\star} - \omega_\star)/360°$, where $t_{\rm ref} = 2{,}455{,}197.5$ JD (i.e., epoch J2010.0).

two solution modes for the orbit of AF Lep b produce nearly identical confidence intervals for most parameters, except for Ω, $\omega_\star$, and $\lambda_{\rm ref,\star}$, which have different median values by approximately 180° between the two modes. Representative orbits for these two solution modes are shown in Figure 2.

We have refined the dynamical mass of AF Lep b to $M_b = 2.8^{+0.6}_{-0.5}\ M_{\rm Jup}$. Several orbital parameters of the planet have also been updated, with median values and confidence intervals summarized in Table 2. Parameter posteriors and the comparison between the observed data and fitted orbits are shown in Appendix B.

We also reassess the spin–orbit alignment of the AF Lep system by using the planet's updated orbital parameters and stellar properties. Adopting a $v \sin(i_\star) = 50 \pm 5$ km s^{-1} (Glebocki & Gnacinski 2005), a stellar radius of $1.21 \pm 0.06\,R_\odot$ (Table 1), and a stellar rotation period of 1.007 ± 0.009 days (Franson et al. 2023b), we follow Bowler et al. (2023) and infer that the inclination of the stellar spin axis is $i_\star = 60^{\circ}{}^{+14^\circ}_{-10^\circ}$. If we switch to a different $v \sin(i_\star)$ of 54.7 ± 0.5 km s^{-1} (Marsden et al. 2014), which has better precision and is among the highest values in the literature, then the inferred $i_\star = 67^{\circ}{}^{+10^\circ}_{-6^\circ}$. These estimated inclinations of the stellar spin axis are consistent with the planet's orbital inclination ($i_b = 55^{\circ}{}^{+8^\circ}_{-13^\circ}$) within 1σ. Thus, the minimum misalignment angle between the spin axis of AF Lep A and the orbit of AF Lep b, $|i_\star - i_b|$, is consistent with zero (also see Section 2 of Bowler et al. 2023). Given that the orientation of the stellar spin axis is unknown, the true spin–orbit misalignment angle can be potentially larger. Therefore, as previously suggested by Franson et al. (2023b), the architecture of the AF Lep system could be consistent with either spin–orbit alignment or spin–orbit misalignment.

5. Contextualizing the Properties of AF Lep b via Evolution Models

In preparation for the atmospheric retrievals of AF Lep b, an analysis of this planet's properties predicted by evolution models is performed. This analysis serves several purposes, including providing important context for the retrieval analysis and helping to avoid inferring unphysical solutions that often

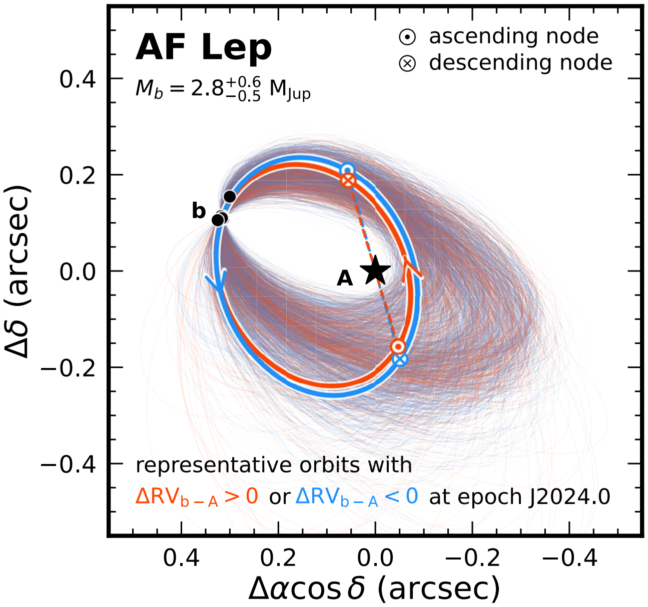

Figure 2. Fitted orbits of AF Lep b, with the red and blue colors denoting positive and negative $\Delta RV_{\rm b-A}$ at epoch J2024.0, respectively. A positive (negative) $\Delta RV_{\rm b-A}$ value means the planet moves, relative to its host star, away from (toward) the observer at a given epoch. Specific signs and values of $\Delta RV_{\rm b-A}$ have not been observed to date. Thin lines are random orbits drawn from the posteriors, and each thick line corresponds to the maximum-likelihood orbital solution for a given sign of $\Delta RV_{\rm b-A}$. The orbital solutions with positive and negative $\Delta RV_{\rm b-A}$ values have similar shapes but the locations of their ascending and descending nodes are nearly swapped. We use a black star to show AF Lep A and black circles to trace the observed relative astrometry of AF Lep b.

occur in atmospheric studies, such as an excessively small radius and/or a high surface gravity of gas-giant exoplanets. The detailed motivation for this evolution model analysis is described in Section 5.1, and the results of the analysis are presented in Section 5.2.

5.1. Motivation: On the Discrepancies between Atmospheric and Evolution Model Predictions

Characterizing properties of directly imaged planets and brown dwarfs usually relies on two types of models: atmospheric models and thermal evolution models. Atmospheric models involve retrievals (a.k.a. inverse modeling; e.g., Line et al. 2015; Burningham et al. 2017; Mollière et al. 2019; also see MacDonald & Batalha 2023) or precomputed temperature–pressure (T–P) composition profiles in radiative–convective equilibrium (RCE), and corresponding synthetic spectra over a grid of parameters (a.k.a. forward modeling; e.g., Burrows et al. 1997; Saumon & Marley 2008; Allard et al. 2012; Morley et al. 2012; Charnay et al. 2018; Phillips et al. 2020; Karalidi et al. 2021; Marley et al. 2021; Mukherjee et al. 2023). These models are fitted to observed spectrophotometry to constrain atmospheric physical properties, such as effective temperature, surface gravity, and radius.

Thermal evolution models adopt the upper boundary condition set by RCE and are typically provided as tables, which calculate an object's effective temperature, bolometric luminosity, and radius, as a function of age, for a given set of modeled masses (e.g., Baraffe et al. 2003; Marley et al. 2007b; Fortney et al. 2008; Saumon & Marley 2008; Spiegel & Burrows 2012; Phillips et al. 2020; Marley et al. 2021). Measurements of any two variables from the set of {mass, age, bolometric luminosity} can provide estimates of the evolution-based properties, including $T_{\rm eff}$, $\log(g)$, and R.

While ideally, atmospheric and evolution models would yield consistent predictions, discrepancies often arise in practice. Zhang et al. (2020, 2021e) found differences between atmospheric properties, inferred from spectra and atmospheric models, and evolution model predictions, inferred from the objects' bolometric luminosities and their host stars' ages. These differences can be significant, with variations of up to 120 K in $T_{\rm eff}$ and 0.5 dex in $\log(g)$. Also, studies on large samples of free-floating late-T and Y dwarfs have noted discrepancies between spectroscopic $\log(g)$ and values based on evolution models (e.g., Zalesky et al. 2019, 2022; Zhang et al. 2021f). Some brown dwarfs have atmospheric $\log(g)$ that would imply unphysical ages (e.g., older than the Universe) according to evolution models. In addition, the "small-radius problem" has been encountered in retrieval analyses of brown dwarfs, where retrieved radii from spectra are much smaller than radii based on evolution given these objects' ages (e.g., Gonzales et al. 2020; Burningham et al. 2021; Lueber et al. 2022; Xuan et al. 2022; Hood et al. 2023).

These discrepancies highlight the systematics of atmospheric models, including uncertainties in opacities (e.g., alkali and $\rm CH_4$ line lists) and assumptions about the chemical (dis)equilibrium, thermal structure, and clouds. Evolution models, although not entirely free of systematics (e.g., Dupuy et al. 2009; Beatty et al. 2018; Brandt et al. 2020; Franson et al. 2023a), provide important context for atmospheric model predictions. Considering the predictions of evolution models is crucial when interpreting parameters inferred from retrieval or forward-modeling analyses, as it helps to account for these discrepancies and provide additional insights into the objects' properties.

5.2. Evolution Model Analysis

To contextualize our subsequent retrieval analysis of AF Lep b, we derive the properties of this planet using the following evolution models.[13]

1. The hot-start Saumon & Marley (2008) evolution models with two versions: $f_{\rm sed} = 2$ and the hybrid version. Both versions assume solar metallicity.
2. The hot-start and cold-start Sonora Bobcat by Marley et al. (2021), with $[{\rm Fe/H}] = -0.5$, 0, and +0.5. The cold-start models are available only at solar metallicity (also see Section 5.5 of Nielsen et al. 2019).
3. The hot-start and cold-start models by Spiegel & Burrows (2012). Cloudless atmospheres are assumed for the solar metallicity models, while cloudy atmospheres are assumed for the 3 × solar metallicity models.
4. The hot-start ATMO2020 models by Phillips et al. (2020) with solar metallicity.
5. The hot-start AMES-COND models by Baraffe et al. (2003) with solar metallicity.

Assuming AF Lep b is coeval with its host star ($t = 24 \pm 3$ Myr; Bell et al. 2015), the planet's dynamical mass

---

[13] The AMES-DUSTY (Chabrier et al. 2000; Baraffe et al. 2002) and the BHAC15 evolution models (Baraffe et al. 2015) are commonly used but are not applicable for AF Lep b, given that more than half of the posteriors of this planet's dynamical mass and age are outside the parameter space of these two sets of evolution models.

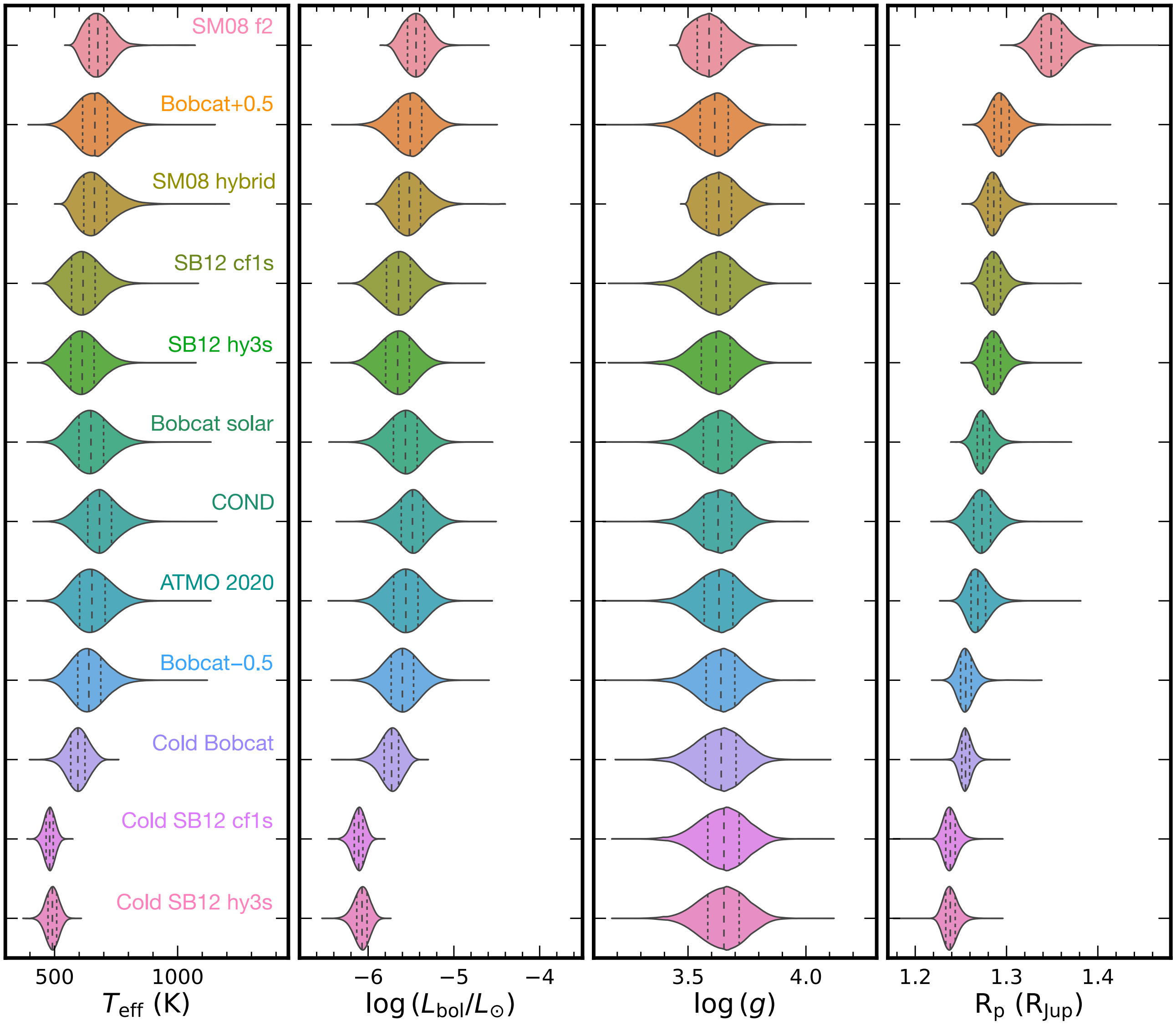

Figure 3. Violin plot for the physical properties of AF Lep b inferred by various evolution models (sorted by radii), based on the planet's dynamical mass and age. The vertical dashed line inside each component highlights the median value of the parameter, while the two dotted lines mark the first and third quartiles of the distribution. The labels and the parameter confidence intervals are shown in Table 3.

($M = 2.8^{+0.6}_{-0.5}\ M_{\rm Jup}$) is combined with this assumed age to determine $T_{\rm eff}$, $\log(L_{\rm bol}/L_\odot)$, $\log(g)$, and R.[14] We use the MCMC chain of dynamical mass from the orbit analysis (Section 4) and generate an equal-size distribution of 1.5×10^6 random ages, sampled from a normal distribution $\mathcal{N}(\mu = 24$ Myr, $\sigma = 3$ Myr) truncated at zero. The evolution models are interpolated in linear scales for $\log(g)$ and $\log(L_{\rm bol}/L_\odot)$ and in logarithmic scales for $T_{\rm eff}$, R, M, and t. No extrapolation is conducted outside the convex hull of each model grid.

Figure 3 and Table 3 summarize the inferred physical properties of AF Lep b using various evolution models. The effective temperature and bolometric luminosity estimates are consistent among all hot-start models. The cold-start models predict slightly lower values since these models assume lower initial entropies at a given planet mass. Surface gravities are similar across all models and the radii are consistent.

Considering that the formation and accretion process of the planet can occur over a few Myr along with the dispersal of the protoplanetary disk (e.g., Alexander et al. 2014), it is likely that AF Lep b is younger than its host star. While the typical disk lifetime is about 3 Myr (e.g., Mamajek 2009; also see reviews by Williams & Cieza 2011 and Drazkowska et al. 2022), here we explore a slightly more extreme case where AF Lep b formed 10 Myr after its host star did. We thus derive another set of physical properties by assuming a planet age of $t = 14 \pm 3$ Myr. Compared to the results assuming coevality with the host star, all evolution models predict 30–120 K hotter $T_{\rm eff}$, 0.01–0.03 dex lower $\log(g)$, 0.01–0.05 $R_{\rm Jup}$ larger R, and 0.1–0.3 dex brighter $\log(L_{\rm bol}/L_\odot)$. These inferred planet parameters are summarized in Appendix C.

Regardless of the assumed age of AF Lep b, the 3σ confidence intervals of the planet's radius inferred from the

---

[14] As explained in Section 5.1, evolution-based properties of objects can be derived by any two variables from the set of $\{M, t, L_{\rm bol}\}$. Here we use mass and age since AF Lep b's bolometric luminosity might not be reliably measured from the spectrophotometry observed to date, which has short-wavelength coverage. Also, the bolometric correction for this young planet requires assumptions built on large uncertainties (e.g., spectral type), compared to those of the dynamical mass and age for this planet.

Table 3
Properties of AF Lep b Based on Evolution Models (Assuming Planet and Host Star Are Coeval)

Label[a]	Evolution Model	$T_{\rm eff}$ (K)	$\log(L_{\rm bol}/L_{\odot})$ (dex)	$\log(g)$ (dex)	R ($R_{\rm Jup}$)
	Hot-start Models				
SM08 f2	Saumon & Marley (2008): cloudy ($f_{\rm sed} = 2$) and [Fe/H] = 0	675^{+54}_{-50}	$-5.44^{+0.15}_{-0.14}$	$3.59^{+0.08}_{-0.07}$	$1.349^{+0.017}_{-0.015}$
SM08 hybrid	Saumon & Marley (2008): hybrid and [Fe/H] = 0	661^{+76}_{-60}	$-5.52^{+0.20}_{-0.17}$	$3.63^{+0.08}_{-0.07}$	$1.286^{+0.011}_{-0.009}$
Bobcat −0.5	Marley et al. (2021): cloudless and [Fe/H] = −0.5	639^{+72}_{-65}	$-5.60^{+0.19}_{-0.19}$	$3.64^{+0.09}_{-0.09}$	$1.255^{+0.009}_{-0.008}$
Bobcat solar	Marley et al. (2021): cloudless and [Fe/H] = 0	647^{+76}_{-70}	$-5.57^{+0.20}_{-0.20}$	$3.63^{+0.08}_{-0.09}$	$1.274^{+0.011}_{-0.009}$
Bobcat +0.5	Marley et al. (2021): cloudless and [Fe/H] = +0.5	663^{+76}_{-71}	$-5.51^{+0.20}_{-0.20}$	$3.61^{+0.08}_{-0.09}$	$1.294^{+0.013}_{-0.011}$
SB12 cf1s	Spiegel & Burrows (2012): cloudless and [Fe/H] = 0	615^{+73}_{-67}	$-5.65^{+0.20}_{-0.21}$	$3.62^{+0.09}_{-0.09}$	$1.286^{+0.011}_{-0.010}$
SB12 hy3s	Spiegel & Burrows (2012): hybrid and [Fe/H] = +0.5	612^{+71}_{-66}	$-5.66^{+0.20}_{-0.21}$	$3.62^{+0.09}_{-0.09}$	$1.286^{+0.011}_{-0.010}$
ATMO2020	Phillips et al. (2020): cloudless and [Fe/H] = 0	651^{+79}_{-71}	$-5.56^{+0.21}_{-0.21}$	$3.63^{+0.09}_{-0.09}$	$1.269^{+0.013}_{-0.011}$
COND	Baraffe et al. (2003): cloudless and [Fe/H] = 0	682^{+73}_{-70}	$-5.48^{+0.19}_{-0.20}$	$3.63^{+0.08}_{-0.09}$	$1.273^{+0.014}_{-0.013}$
	Cold-start Models				
Cold Bobcat	Marley et al. (2021): cloudless and [Fe/H] = −0.5	594^{+42}_{-42}	$-5.73^{+0.12}_{-0.13}$	$3.64^{+0.09}_{-0.10}$	$1.255^{+0.007}_{-0.006}$
Cold SB12 cf1s	Spiegel & Burrows (2012): cloudless and [Fe/H] = 0	480^{+21}_{-21}	$-6.11^{+0.07}_{-0.08}$	$3.65^{+0.09}_{-0.10}$	$1.238^{+0.008}_{-0.007}$
Cold SB12 hy3s	Spiegel & Burrows (2012): hybrid and [Fe/H] = +0.5	491^{+25}_{-26}	$-6.07^{+0.08}_{-0.09}$	$3.65^{+0.09}_{-0.10}$	$1.238^{+0.008}_{-0.007}$

Note.
[a] The label of each evolution model shown in Figure 3.

evolution models fall within the range of 1.20–1.55 $R_{\rm Jup}$. This range will be implemented as a uniform prior for R in the subsequent retrieval analysis to address the "small-radius problem" encountered in other recent retrieval studies.[15]

6. Atmospheric Retrieval Framework

To characterize the atmospheric composition of AF Lep b, we use the `petitRADTRANS` code (Mollière et al. 2019) to perform chemically consistent retrievals for the planet's spectrophotometry (Section 2.2). A novel parameterization approach for the *T–P* profile is also introduced (Sections 6.1–6.2) that can lead to a robust characterization of cloudy self-luminous atmospheres for giant planets and brown dwarfs.

6.1. Temperature Model

We model the thermal profile of AF Lep b by dividing its atmosphere into six layers that are evenly spaced in a logarithmic scale of pressure, ranging from 10^3 bar to 10^{-3} bar. The temperature gradient, $d\ln T/d\ln P$, is fitted at each of these layers (Figure 4). Another free parameter $T_{\rm bottom}$ is added for the temperature of the bottom layer at 10^3 bar. With a given set of $d\ln T/d\ln P$ at the six layers, a quadratic interpolation is performed to obtain the temperature gradient over a finer grid consisting of 1000 evenly spaced layers. The temperature, T_j, at each layer is then calculated as

$$\begin{aligned} T_1 &= T_{\rm bottom} \\ T_{j+1} &= \exp\left[\ln T_j + (\ln P_{j+1} - \ln P_j) \times \left(\frac{d\ln T}{d\ln P}\right)_j\right] \\ &\quad \text{with } j = 1, 2, 3,\ldots,1000 \end{aligned} \tag{2}$$

where a larger j corresponds to a level with a higher altitude (or a lower pressure). An upper atmosphere with pressures below 10^{-3} bar is assumed to be isothermal.

This new parameterization of the *T–P* profile differs from the typical thermal model employed in retrieval analyses of exoplanets and brown dwarfs, where the temperature is explicitly modeled as a function of pressure (e.g., Line et al. 2015, 2017; Burningham et al. 2017, 2021; Lavie et al. 2017; Zalesky et al. 2019, 2022; Mollière et al. 2020; Wang et al. 2020; Gonzales et al. 2021, 2022; Zhang et al. 2021a, 2021b; Brown-Sevilla et al. 2023; Xuan et al. 2022; Gaarn et al. 2023; Hood et al. 2023; Whiteford et al. 2023). Piette & Madhusudhan (2020) developed a similar *T–P* parameterization to our approach, though their framework models the temperature differences among a predefined grid of pressure layers. As shown in the next subsection (Section 6.2) and in Section 8.3, modeling *T–P* profiles via the temperature gradient enables the incorporation of the RCE as parameterized priors on the planet's thermal structure; this novel approach leads to a robust characterization of self-luminous atmospheres, especially those influenced by clouds.

6.2. Coupling T–P Profiles with RCE

Near the L/T transition, giant planets and brown dwarfs undergo significant changes in their spectrophotometric properties (e.g., Golimowski et al. 2004; Radigan et al. 2014; Vos et al. 2019; Best et al. 2021; Kirkpatrick et al. 2021), which are thought to be related to the formation, condensation, and dissipation of clouds containing refractory species such as silicate and iron (e.g., Lodders & Fegley 2006;

---

[15] Our subsequent retrieval analysis suggests that AF Lep b likely has a metal-enriched atmosphere with [Fe/H] above 1.0 dex (see Table 6 and Section 8.1.1). This high metallicity value is beyond the [Fe/H] grid of the existing evolution models of exoplanets and brown dwarfs (see Table 3). Future modeling efforts that self-consistently combine the planet interior models and atmospheric models with significant metal enrichment are warranted to provide context for the radius of planets such as AF Lep b.

Table 4
Atmospheric Model Grids Investigated in Section 6.2

Forward Model Grid	Parameters						Assumptions	
	$T_{\rm eff}$	log(g)	[Fe/H]	C/O	log(K_{zz})	Cloud	Clouds?	Chem. Eq.?
ATMO2020	[200, 3000]	[2.5, 5.5]	0	0.55	multiple[a]	⋯	cloudless	CEQ + NEQ
Sonora Bobcat	[200, 2400]	[3.0, 5.5]	[−0.5, +0.5]	[0.229, 0.687]	⋯	⋯	cloudless	CEQ
Sonora Cholla	[500, 1300]	[3.5, 5.0]	0	0.458	[2, 9]	⋯	cloudless	NEQ
Mukherjee et al. (2022)	[400, 1000]	[4.5, 5.5]	0	0.458	multiple[b]	⋯	cloudless	NEQ
Lacy & Burrows (2023)	[200, 600]	[3.5, 5.0]	[−0.5, +0.5]	0.55	6	multiple[c]	cloudy	CEQ + NEQ

Notes.
[a] The K_{zz} of the ATMO2020 chemical disequilibrium models is a function of the surface gravity (see Figure 1 of Phillips et al. 2020).
[b] The disequilibrium chemistry in the Mukherjee et al. (2022) models is described in terms of (1) the varying K_{zz} in the radiative zones by factors of 100, 1, and 0.01 from the Moses et al. (2022) parameterization, and (2) the varying convective mixing lengths set by 1 × and 0.1 × the scale height.
[c] Water clouds of the Lacy & Burrows (2023) models are described by different shapes of the vertical opacity profiles.

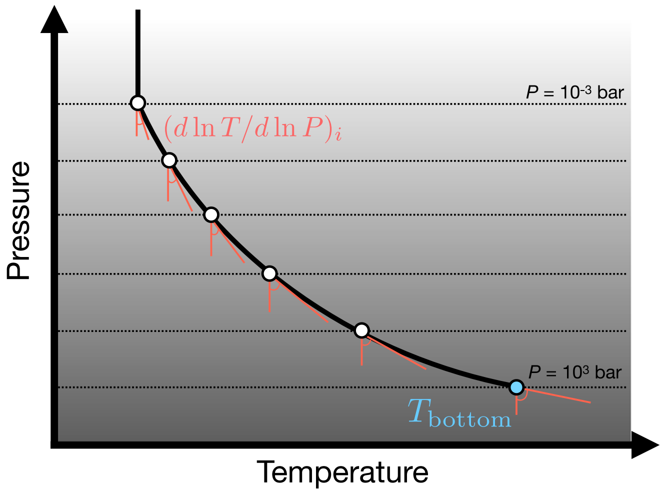

Figure 4. Sketch of the temperature model described in Section 6.1.

Marley & Robinson 2015). However, retrievals of these cloudy objects sometimes result in a cloudless solution with a more isothermal T–P profile compared to the profile calculated under the assumption of RCE using the same $T_{\rm eff}$, log(g), and composition (e.g., Burningham et al. 2017; Mollière et al. 2020; Brown-Sevilla et al. 2023; Whiteford et al. 2023). This retrieved T–P profile converges with the RCE profile near the photosphere, but the former features relatively cooler temperatures in deeper atmospheres and warmer temperatures in upper atmospheres. The reduced temperature gradient of the retrieved T–P profiles mimics the effect of clouds by reddening the emergent spectra. Admittedly, the more isothermal T–P profile is consistent with a scenario proposed by Tremblin et al. (2016, 2019), where thermocompositional instabilities could explain the atmospheric properties of giant planets and brown dwarfs without invoking clouds. However, it is expected that cloud formation occurs in the ultracool, molecule-rich atmospheres of these objects. Observations from Spitzer and the recently launched JWST also probe the spectral features of silicate clouds near 10 μm across the L/T transition (Cushing et al. 2006; Suárez & Metchev 2022; Miles et al. 2023).

To address the "cloudless isothermal T–P problem" encountered in retrievals, we propose a new approach, which involves coupling the T–P profiles with RCE during the retrieval process. Since the shape of T–P profiles and cloud properties are degenerate, our strategy is to add priors to the temperature gradient, $d\ln T/d\ln P$, that follow the shape expected by the RCE. These priors of the T–P profiles retrospectively constrain the cloud properties.

To establish these priors, we examine the T–P profiles generated by various sets of atmospheric model grids that are all precomputed under the RCE assumption. For each model set, we examine the T–P profile at each grid point within the corresponding parameter space and investigate the temperature gradient as a function of pressure. This investigation results in quantitative perspectives about the distribution of $(d\ln T/d\ln P)_{\rm RCE}$ at a given pressure layer. Our retrieval framework directly fits the $d\ln T/d\ln P$ values at six pressure layers throughout the atmosphere (Section 6.1), and thus, the $(d\ln T/d\ln P)_{\rm RCE}$ distributions in these six pressure levels provide priors to our $d\ln T/d\ln P$ parameters.

Five sets of atmospheric models are used to examine the $(d\ln T/d\ln P)_{\rm RCE}$ distributions:

1. The ATMO2020 models (Phillips et al. 2020)
2. The Sonora Bobcat models (Marley et al. 2021)
3. The Sonora Cholla models (Karalidi et al. 2021)
4. The models presented by Mukherjee et al. (2022)
5. The models presented by Lacy & Burrows (2023)

The parameter space and assumptions of these grids are listed in Table 4. Figure 5 presents the median and confidence intervals of the $(d\ln T/d\ln P)_{\rm RCE}$ profile by combining all grid points of each model set. While the temperature gradient profiles of these model grids are similar, they are not identical due to their different assumptions about clouds and chemical (dis)equilibrium.

We adopt the following Gaussian priors for $(d\ln T/d\ln P)$ at each of the six pressure layers:

$$\begin{aligned}
&\frac{d\ln T}{d\ln P}(P = 10^3 \text{ bar}) \sim \mathcal{N}(\mu = 0.250,\, \sigma = 0.025)\\
&\frac{d\ln T}{d\ln P}(P \approx 63 \text{ bar}) \sim \mathcal{N}(\mu = 0.250,\, \sigma = 0.045)\\
&\frac{d\ln T}{d\ln P}(P \approx 4 \text{ bar}) \sim \mathcal{N}(\mu = 0.260,\, \sigma = 0.050)\\
&\frac{d\ln T}{d\ln P}(P \approx 0.3 \text{ bar}) \sim \mathcal{N}(\mu = 0.200,\, \sigma = 0.050)\\
&\frac{d\ln T}{d\ln P}(P \approx 0.02 \text{ bar}) \sim \mathcal{N}(\mu = 0.120,\, \sigma = 0.045)\\
&\frac{d\ln T}{d\ln P}(P = 10^{-3} \text{ bar}) \sim \mathcal{N}(\mu = 0.070,\, \sigma = 0.070).
\end{aligned} \tag{3}$$

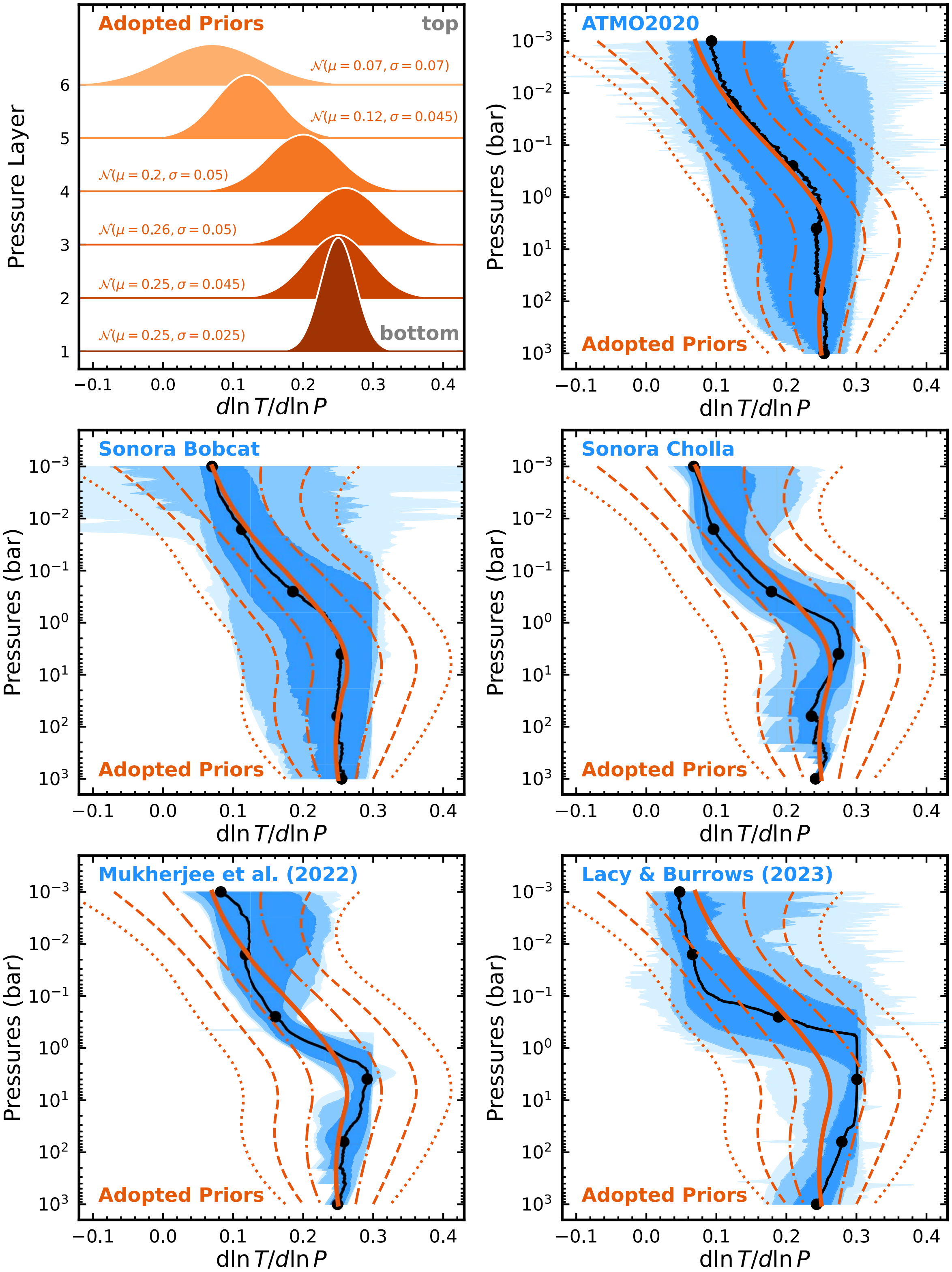

Figure 5. Top left: Our adopted Gaussian priors for the temperature gradient ($d\ln T/d\ln P$) at six pressure layers, with layer numbers one and six corresponding to the bottom and top of the atmosphere with $P = 10^3$ bar and 10^{-3} bar, respectively. Top right: The $(d\ln T/d\ln P)_{\rm RCE}$ profile of the ATMO2020 model grid. The black line is the median profile among all grid points and the blue shaded regions represent (from dark to light) the 1σ, 2σ, and 3σ confidence intervals. Black circles mark the $(d\ln T/d\ln P)_{\rm RCE}$ value of the six pressure layers. Overlaid orange lines (solid: median; dashed–dotted: 1σ boundary; dashed: 2σ boundary; dotted: 3σ boundary) represent our adopted priors. For these prior profiles, the median and confidence intervals at the six pressure layers are described in the top left panel, and the values between these layers are calculated via a quadratic interpolation (in logarithmic scale of pressure). Middle and bottom: These panels share the format of the top right panel but with different forward model grids as summarized in Table 4.

The mean and standard deviation of these Gaussian distributions are visually determined such that the confidence intervals of the temperature gradient profiles are qualitatively consistent between the grid models and the priors. The pressures of each layer are rounded in Equation (3), but the exact pressure values are used in the retrievals.

Our $(d\ln T/d\ln P)$ priors have been established using grid models that encompass a much broader parameter space than the one centered on the properties of AF Lep b. Consequently, the priors presented in Equation (3) may be applied to a more diverse sample of directly imaged exoplanets and brown dwarfs. We also recommend users to customize the number of layers and the prior values by using different sets of forward models that align with their individual targets.

6.3. Chemistry and Cloud Models

The chemistry and cloud models used in the retrievals are based on the approach described in Mollière et al. (2020), with a brief summary below.

We first compute the abundances of all opacity sources at each atmospheric layer under the equilibrium chemistry. This calculation involves adding [Fe/H] and C/O as free parameters and combining them with the T–P profiles in the retrievals (also see Mollière et al. 2017). To account for the effect of chemical disequilibrium, the logarithmic quench pressure $\log(P_{\rm quench})$ is added as a free parameter. The abundances (or mass fractions) of H_2O, CO, and CH_4 with $P < P_{\rm quench}$ are then reset to the abundances with $P = P_{\rm quench}$ (e.g., Zahnle & Marley 2014). Thus, a higher $P_{\rm quench}$ value suggests that the disequilibrium chemistry impacts a wider vertical extent of the atmosphere.

The line species in our retrievals include H_2O (Polyansky et al. 2018), CO (Kurucz 1993; Rothman et al. 2010), CO_2 (Yurchenko et al. 2020), CH_4 (Hargreaves et al. 2020), NH_3 (Coles et al. 2019), Na (Allard et al. 2019), K (Allard et al. 2016), PH_3 (Sousa-Silva et al. 2015), VO and TiO (B. Plez, private communication; see Mollière et al. 2019), FeH (Wende et al. 2010), and H_2S (Azzam et al. 2016). We also include H_2 and He as opacity sources of Rayleigh scattering (Dalgarno & Williams 1962; Chan & Dalgarno 1965) and H_2–H_2 and H_2–He as sources of collision-induced absorption (J. Borysow et al. 1988; Borysow & Frommhold 1989; A. Borysow et al. 1989, 2001; Borysow 2002; Richard et al. 2012).

Cloud opacity is described by the mass fraction profile $X(P)$ of each cloud species, the mean size of the cloud particles r_g, and the width of the lognormal cloud particle size distribution σ_g (Mollière et al. 2019). For a given condensate, the cloud mass fraction profile is defined above the pressure of the cloud base $P_{\rm base}$, determined by the intersection between the T–P profile and the corresponding saturation vapor pressure curve. The $X(P)$ profile is computed as $X_0(P/P_{\rm base})^{f_{\rm sed}}$, with X_0 being the cloud mass fraction at the base pressure and $f_{\rm sed}$ being the sedimentation efficiency. The mean size of cloud particles r_g is determined by $f_{\rm sed}$ and the eddy diffusion coefficient K_{zz} (assumed to be independent of pressure) following the Ackerman & Marley (2001) prescription. As explained by Mollière et al. (2020), the K_{zz} parameter (in our framework) only helps to determine the cloud particle size distribution; it might be inconsistent with $\log(P_{\rm quench})$, which is a dedicated parameter for the disequilibrium chemistry.

The cloud species considered in our retrievals are $MgSiO_3$, Fe, and KCl, with irregular shapes and crystalline structures. The former two condensates are important for objects near the L/T transition (e.g., Lunine et al. 1986; Tsuji et al. 1996; Allard et al. 2001; Marley et al. 2002, 2012; Lodders & Fegley 2006). Also, with the cool effective temperature of AF Lep b ($T_{\rm eff} \approx 650$ K, Table 3), chloride and sulfide clouds become nonnegligible (e.g., Morley et al. 2012). According to the microphysics models by Gao et al. (2020), KCl cloud formation is more efficient than the formation of sulfide clouds given the fast nucleation rates of the former, so KCl clouds are added in our retrievals. All cloud condensates are assumed to share the K_{zz} and σ_g. Each species corresponds to an independent combination of $(X_0, f_{\rm sed})$, amounting to a total of eight free parameters in the cloud model.

6.4. Emission Spectroscopy

In the retrievals, emission spectra are generated via `petitRADTRANS` by combining the T–P profile, the line/continuum/cloud opacities, cloud scattering (see Mollière et al. 2020), and the planet's surface gravity $\log(g)$. The computed spectrum is then scaled by a factor of $(R/d)^2$ for comparison with the observed data, where $d = 26.8$ pc is the distance of AF Lep A and R is the planet radius as a free parameter. When analyzing the two sets of IFS spectra of AF Lep b collected by De Rosa et al. (2023) and Mesa et al. (2023), an additive flux offset is implemented for each spectrum ($\Delta f_{\rm D23}$ and $\Delta f_{\rm M23}$) as a free parameter (see discussion in Section 2.2). However, when analyzing only one spectrum, the originally observed flux is used. In addition, when photometric data are included in the retrievals, we compute the $K1/K2/L'$ photometry from the modeled emission spectrum by using the response curves obtained from the VLT/SPHERE[16] and Keck/NIRC2[17] websites (also see Figure 1).

Examples of the emission spectra are shown in Figure 6. These forward-modeled spectra are calculated over a small parameter space around AF Lep b's properties, with $T_{\rm eff}$ = 700–900 K, $\log(g)$ = 3.5–4.5 dex, [Fe/H] = 0–1 dex, C/O = 0.3–0.8, and $\log(P_{\rm quench}/1\ {\rm bar}) = 3$. Clouds of $MgSiO_3$ and Fe are incorporated, with $\log(X_0) = -2$ dex and -4 dex, respectively, and $f_{\rm sed} = 2$ and $\log(K_{zz}) = 8$ for both condensates. Each spectrum is generated based on a self-consistent T–P profile computed under RCE using `petitCODE` (Mollière et al. 2015, 2017). These forward-modeled spectra are not used for the analysis of AF Lep b but are provided as examples to illuminate the effect of different physical parameters on spectral morphology.

6.5. Free Parameters and Nested Sampling

Table 5 summarizes all free parameters and their corresponding priors used in the retrievals. `PyMultiNest` (Buchner et al. 2014), building on `MultiNest` (Feroz & Hobson 2008; Feroz et al. 2009, 2019), is employed by `petitRADTRANS` for nested sampling. We adopt 4000 live points to sample the parameter posteriors and set a 0.05 sampling efficiency under the constant-efficiency mode of `MultiNest`.

7. Retrieval Analysis of AF Lep b

We perform retrievals on three sets of input data:

1. all published $K1/K2/L'$ photometry and the Mesa et al. (2023) spectrum,

---

[16] https://www.eso.org/sci/facilities/paranal/instruments/sphere/inst/filters.html

[17] https://www2.keck.hawaii.edu/inst/nirc2/filters.html

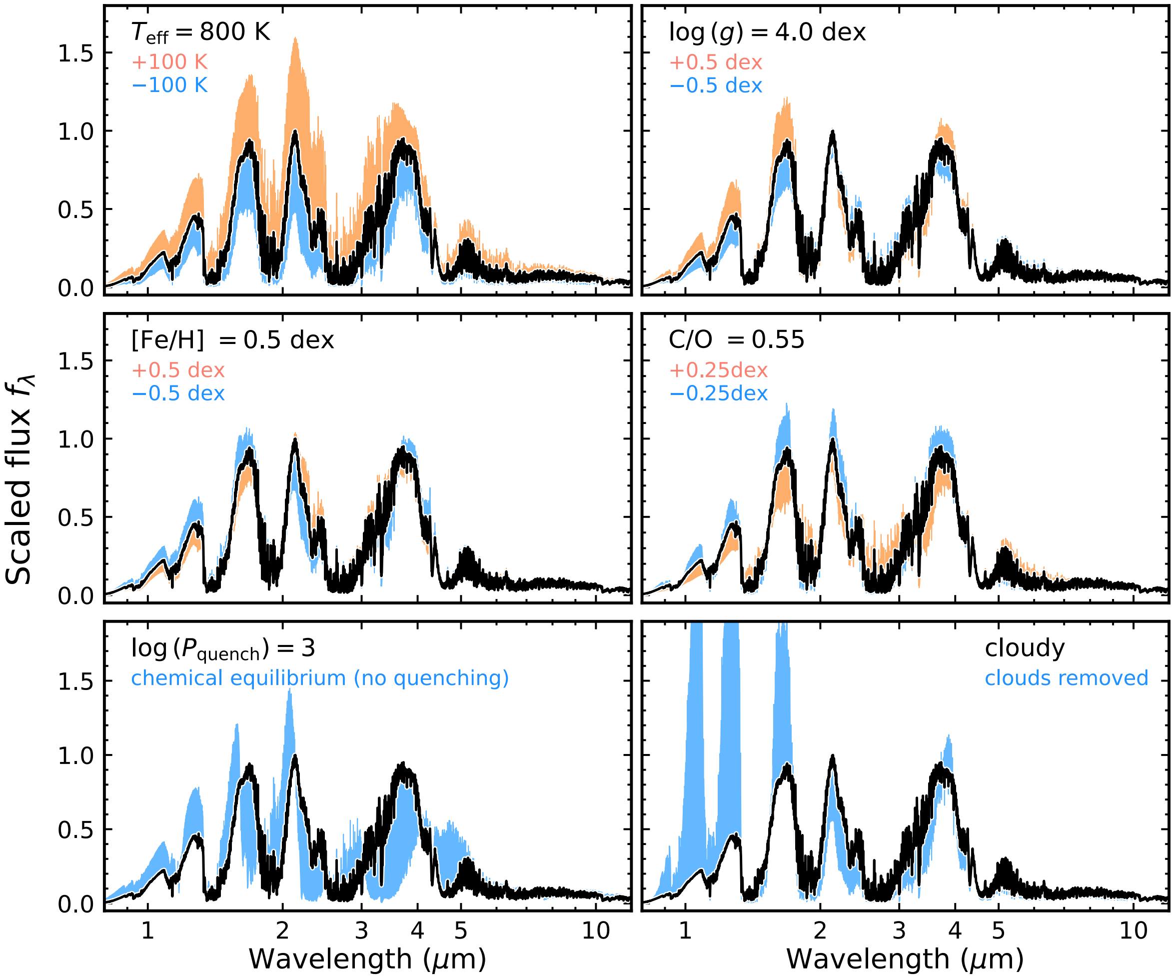

Figure 6. The forward-modeled emission spectra ($R = 1000$) over a mini-grid of parameter space in the vicinity of AF Lep b's properties (Section 6.4). The black spectrum corresponds to a cloudy model with $T_{\rm eff} = 800$ K, $\log(g) = 4.0$ dex, [Fe/H] = 0.5 dex, C/O = 0.55 dex, $\log(P_{\rm quench}/1\ {\rm bar}) = 3$, and $f_{\rm sed} = 2$ and $\log(K_{zz}) = 8$ for both $MgSiO_3$ and Fe clouds, whose mass fractions at the base pressures are $\log(X_0) = -2$ dex and -4 dex, respectively. In each panel, we use orange/blue colors to show the spectral effect when a certain parameter is increased/decreased by the labeled amount (top and middle panels) or is removed (bottom panels).

2. all $K1/K2/L'$ photometry and the De Rosa et al. (2023) spectrum, and
3. all $K1/K2/L'$ photometry and the spectra from both Mesa et al. (2023) and De Rosa et al. (2023).

For each data set, three sets of parameter priors are adopted:

1. We first use the default priors listed in Table 5.
2. On the basis of Table 5, a Gaussian prior is adopted for the planet mass (M) based on the directly measured dynamical mass (Section 4): $\mathcal{N}(\mu = 2.8\ M_{\rm Jup}, \sigma = 0.6\ M_{\rm Jup})$. This new prior is more constrained compared to the default mass prior of $\mathcal{U}(0.03\ M_{\rm Jup}, 797\ M_{\rm Jup})$ in Table 5, as converted from the default $\log(g)$ and R priors.
3. On the basis of Table 5, we add constrained priors on both the planet mass, $\mathcal{N}(\mu = 2.8\ M_{\rm Jup}, \sigma = 0.6\ M_{\rm Jup})$, and the planet radius, $\mathcal{U}(1.20\ R_{\rm Jup}, 1.55\ R_{\rm Jup})$. This new radius prior is contextualized by various evolution models (Section 5.2).

In total, we perform nine retrieval runs (given three data sets and three sets of priors). The bolometric luminosity and effective temperature are further derived after each retrieval run. Specifically, we use `petitRADTRANS` to generate emission spectra over a wavelength range of 0.6–250 μm based on parameters sampled from the inferred posteriors. Then we extrapolate each spectrum to zero flux at 0 μm and append a Rayleigh–Jeans tail toward longer wavelengths up to 1000 μm. $L_{\rm bol}$ is computed by integrating the spectrum and $T_{\rm eff}$ is derived by combining $L_{\rm bol}$ with the retrieved R following the Stefan–Boltzmann law.

In Figures 7–9, we present the results of our retrieval analysis for each input data set, with the constrained M and R priors incorporated. Similar figures for other combinations of input data sets and priors can be found in Appendix D. Figure 10 presents the parameter posteriors for two selected retrieval runs. Figure 11 summarizes and compares the posteriors of key physical parameters from all these nine retrievals. The median and 1σ confidence intervals of all the parameters are listed in Table 6. For the rest of this section, we discuss our retrieval results on each input data set with each set of priors.

7.1. Retrievals on the $K1/K2/L'$ Photometry and the Mesa et al. (2023) Spectrum

When analyzing all available photometry and the Mesa et al. (2023) spectrum of AF Lep b, regardless of whether the constrained priors on M and R are adopted, the retrievals

Table 5
Free Parameters of Retrievals

Parameter	Prior	Description
Temperature Model (Sections 6.1–6.2)		
$T_{\rm bottom}$	$\mathcal{U}(2 \times 10^3$ K, 10^4 K)	Temperature at $P = 10^3$ bar
$(d\ln T/d\ln P)_1$	$\mathcal{N}(\mu = 0.250, \sigma = 0.025)$	Temperature gradient at $P = 10^3$ bar
$(d\ln T/d\ln P)_2$	$\mathcal{N}(\mu = 0.250, \sigma = 0.045)$	Temperature gradient at $P \approx 63$ bar
$(d\ln T/d\ln P)_3$	$\mathcal{N}(\mu = 0.260, \sigma = 0.050)$	Temperature gradient at $P \approx 4$ bar
$(d\ln T/d\ln P)_4$	$\mathcal{N}(\mu = 0.200, \sigma = 0.050)$	Temperature gradient at $P \approx 0.3$ bar
$(d\ln T/d\ln P)_5$	$\mathcal{N}(\mu = 0.120, \sigma = 0.045)$	Temperature gradient at $P \approx 0.02$ bar
$(d\ln T/d\ln P)_6$	$\mathcal{N}(\mu = 0.070, \sigma = 0.070)$	Temperature gradient at $P = 10^{-3}$ bar
Chemistry Model (Section 6.3)		
[Fe/H]	$\mathcal{U}(-1$ dex, 2 dex)	Iron abundance (relative to solar) of the exoplanet atmosphere
C/O	$\mathcal{U}(0.1, 1.6)$	Absolute carbon-to-oxygen ratio of the exoplanet atmosphere
$\log(P_{\rm quench}/1$ bar)	$\mathcal{U}(-6$ dex, 3 dex)	Quench pressure of H_2O, CH_4, and CO
Cloud Model (Section 6.3)		
$\log(X_{0,{\rm MgSiO_3}})$	$\mathcal{U}(-10$ dex, 0 dex)	Mass fraction of the $MgSiO_3$ cloud at base pressure
$f_{\rm sed,MgSiO_3}$	$\mathcal{U}(0, 10)$	Sedimentation efficiency of the $MgSiO_3$ cloud
$\log(X_{0,{\rm Fe}})$	$\mathcal{U}(-10$ dex, 0 dex)	Mass fraction of the Fe cloud at base pressure
$f_{\rm sed,Fe}$	$\mathcal{U}(0, 10)$	Sedimentation efficiency of the Fe cloud
$\log(X_{0,{\rm KCl}})$	$\mathcal{U}(-10$ dex, 0 dex)	Mass fraction of the KCl cloud at base pressure
$f_{\rm sed,KCl}$	$\mathcal{U}(0, 10)$	Sedimentation efficiency of the KCl cloud
$\log(K_{zz})$	$\mathcal{U}(5$ dex, 13 dex)	Vertical eddy diffusion coefficient of clouds
σ_g	$\mathcal{U}(1.02, 3)$	Width of the lognormal cloud particle size distribution
Other Physical Parameters[a] (Section 6.4)		
$\log(g)$	$\mathcal{U}(2.5$ dex, 5.5 dex)	Surface gravity of the planet
R	$\mathcal{U}(0.5\ R_{\rm Jup}, 2.5\ R_{\rm Jup})$	Radius of the planet
Combined Spectral Data Set[b] (Section 6.4)		
$\Delta f_{\rm M23}$	$\mathcal{U}(-3 \times f_{\rm max,M23}, 3 \times f_{\rm max,M23})$	Flux offset for the Mesa et al. (2023) IFS spectrum
$\Delta f_{\rm D23}$	$\mathcal{U}(-3 \times f_{\rm max,D23}, 3 \times f_{\rm max,D23})$	Flux offset for the De Rosa et al. (2023) IFS spectrum

Notes.
[a] Some of our retrieval runs adopt narrower and well-constrained priors on mass and radius (see Section 7).
[b] The fluxes $f_{\rm max,D23}$ and $f_{\rm max,M23}$ represent the maximum flux of the De Rosa et al. (2023) and Mesa et al. (2023) IFS spectra, respectively.

consistently predict higher [Fe/H] values of the planet compared to those of its host star (Figure 11). The enhanced metallicity of the planet is potentially linked to its formation history and will be discussed in Section 8.1. The retrieved C/O values all have large uncertainties and are consistent with solar abundance. The relative C/O between the planet and its host star is unknown, given that the stellar C/O cannot be reliably measured due to the fast stellar rotation (Section 3). The precision of the retrieved $\log(g)$ improves when a constrained M prior is included. When a narrow R prior is also adopted, the resulting $\log(g)$ posterior primarily reflects the M and R priors.

With a default radius prior of $\mathcal{U}(0.5\ R_{\rm Jup}, 2.5\ R_{\rm Jup})$, the retrieved R of the planet falls in the range of 0.8–1.1 $R_{\rm Jup}$. This radius is considered slightly small given the planet's dynamical mass and its young age based on evolution models (Section 5.2). This "small-radius problem" also occurred in other spectroscopic studies of brown dwarfs and giant planets (e.g., Gonzales et al. 2020; Burningham et al. 2021; Zhang et al. 2021f; Lueber et al. 2022; Xuan et al. 2022; Hood et al. 2023). The underestimated radius of the planet leads to an overestimated effective temperature, given that the derived bolometric luminosity is mostly consistent among the different retrieval runs (Figure 11). After incorporating a constrained and narrower R prior, the resulting $T_{\rm eff}$ decreases from ≈900 K to ≈800 K.

Retrievals of the input data set also imply that the atmosphere of AF Lep b is likely impacted by the disequilibrium chemistry, as the retrieved $\log(P_{\rm quench}/1$ bar) consistently hovers around 2.3 dex in all three runs with different sets of parameter priors. Turning off the disequilibrium chemistry in our best-fit model spectrum results in an excessive CH_4 absorption that is incompatible with the observed spectrophotometry. The effect of disequilibrium chemistry on the resulting profiles of H_2O, CO, and CH_4 abundances is also demonstrated by Figure 12.

In addition, AF Lep b likely has silicate clouds (e.g., $MgSiO_3$) in the atmosphere with a sedimentation efficiency of $f_{\rm sed} = 2$–3 and a high mass fraction of $\log(X_0) \approx -1.5$. The properties of the other two cloud species, Fe and KCl, cannot be well constrained, as their retrieved $f_{\rm sed}$ and $\log(X_0)$

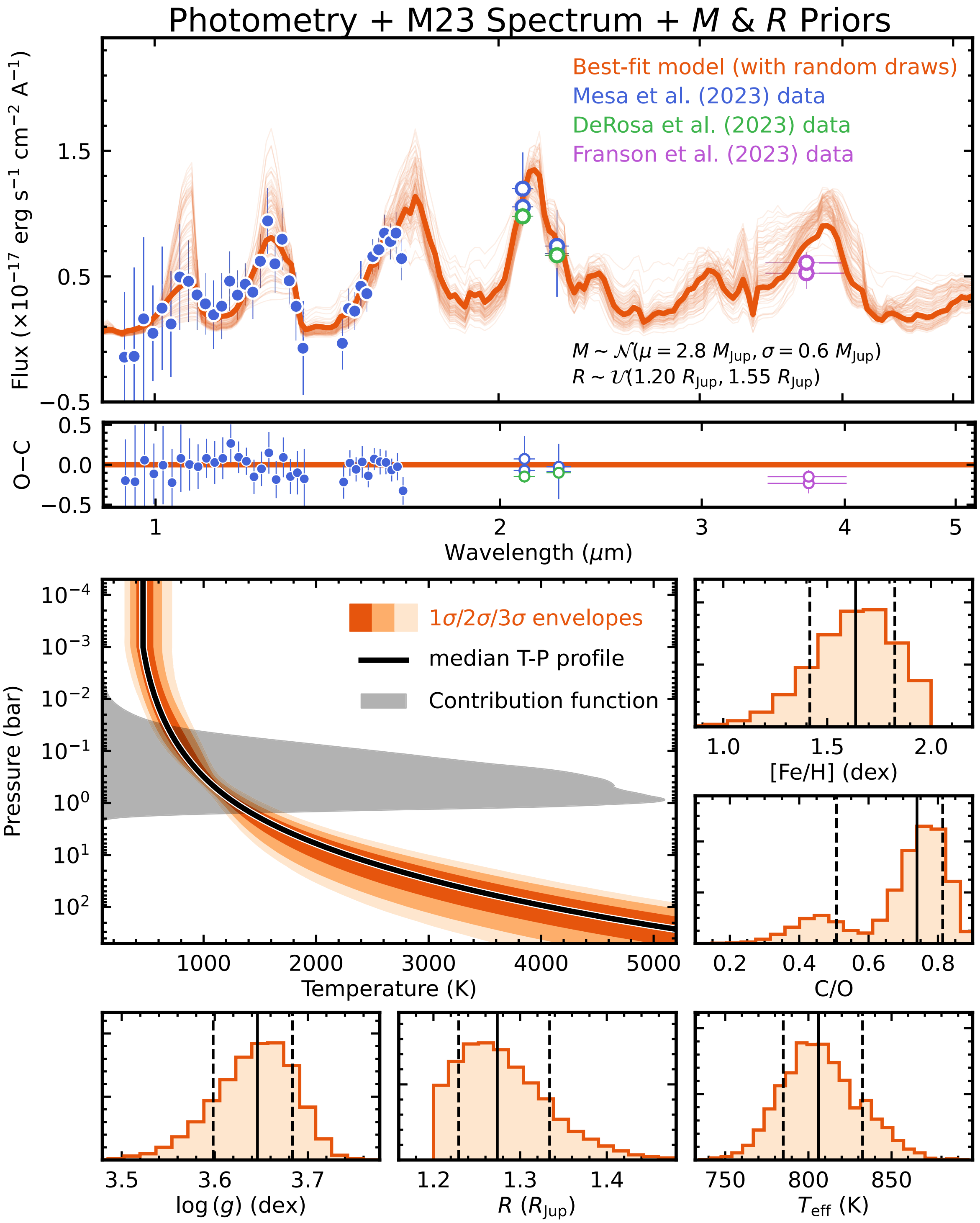

Figure 7. Results of the retrieval analysis on $K1/K2/L'$ photometry and the Mesa et al. (2023) spectrum of AF Lep b (Section 7.1). In the top two panels, we compare the observed spectrophotometry (colored circles with the same format as Figure 1; the wavelength error bars of the $K1/K2/L'$ photometric data represent the half effective widths of the corresponding filters) with the emission spectrum corresponding to the best-fit model (thick orange line). Emission spectra generated at 100 random draws from the parameter posteriors (thin orange lines) are overlaid. In the middle section, on the left panel, we present the $1\sigma/2\sigma/3\sigma$ confidence intervals (orange shades) of our retrieved T–P profiles. A profile with median T–P parameters is shown in black and the corresponding weighted contribution function (computed over the same wavelength range as the input data) is shown as a gray shade. The remaining panels present the posterior distributions of key physical parameters: [Fe/H], C/O, log(g), R, and $T_{\rm eff}$. The median and confidence intervals of all parameters are summarized in Table 6.

posteriors remain close to the adopted priors. The presence of clouds is also supported by the very red slope of the spectrophotometry, especially considering the relatively flat slope of the Mesa et al. (2023) spectrum in the Y and J bands, as well as the comparable or brighter $K1/K2$ photometry relative to the fluxes at shorter wavelengths (Figure 7).

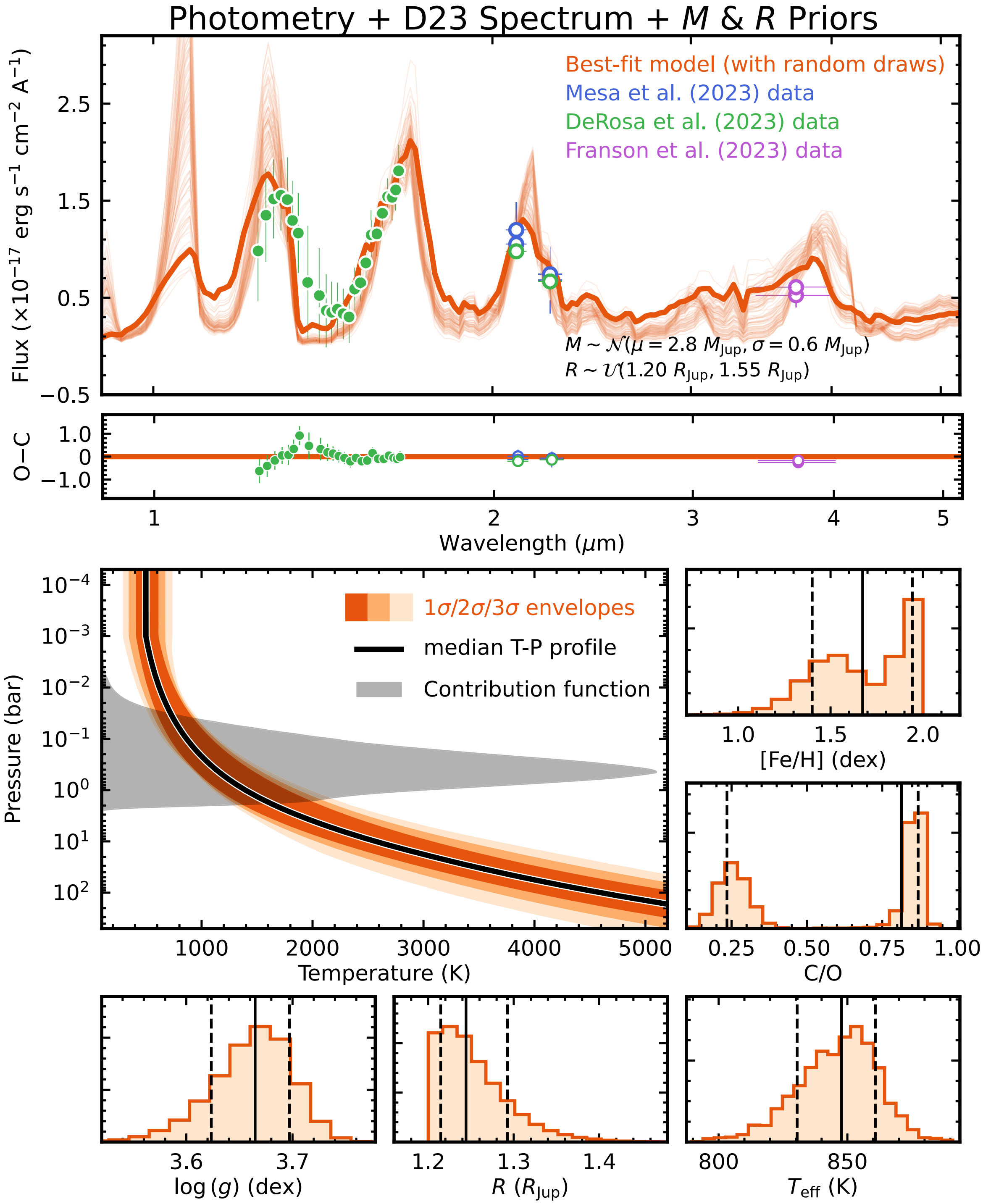

Figure 8. Results of the retrieval analysis on $K1/K2/L'$ photometry and the De Rosa et al. (2023) spectrum of AF Lep b (Section 7.2), with the same format as Figure 7.

7.2. Retrievals on the $K1/K2/L'$ Photometry and the De Rosa et al. (2023) Spectrum

When analyzing $K1/K2/L'$ photometry and the De Rosa et al. (2023) spectrum with default M and R priors, our retrieval results show that the atmospheric [Fe/H] of AF Lep b is consistent with the metallicity of its host star. However, in this retrieval run, the derived planet radius of $R = 0.67^{+0.07}_{-0.06}\ R_{\rm Jup}$ is unphysically small. When combined with the derived $\log(g) = 2.87^{+0.37}_{-0.23}$ dex, this radius implies a very low planet mass ($0.13^{+0.17}_{-0.05}\ M_{\rm Jup}$) that contradicts the observed astrometric properties of the system (Section 4). By incorporating more constrained and physics-driven priors for M, or both M and R, the retrieved [Fe/H] of AF Lep b becomes higher than that of its host star, as seen from the retrievals obtained with the Mesa et al. (2023) spectrum (Section 7.1). Also, impact from the disequilibrium chemistry is still likely, given that $\log(P_{\rm quench}/1\ {\rm bar})$ spans 1.1–1.6 dex with constrained M and/or R priors.

When default parameter priors are adopted, the presence of any type of cloud is not suggested by this data set. Unlike the

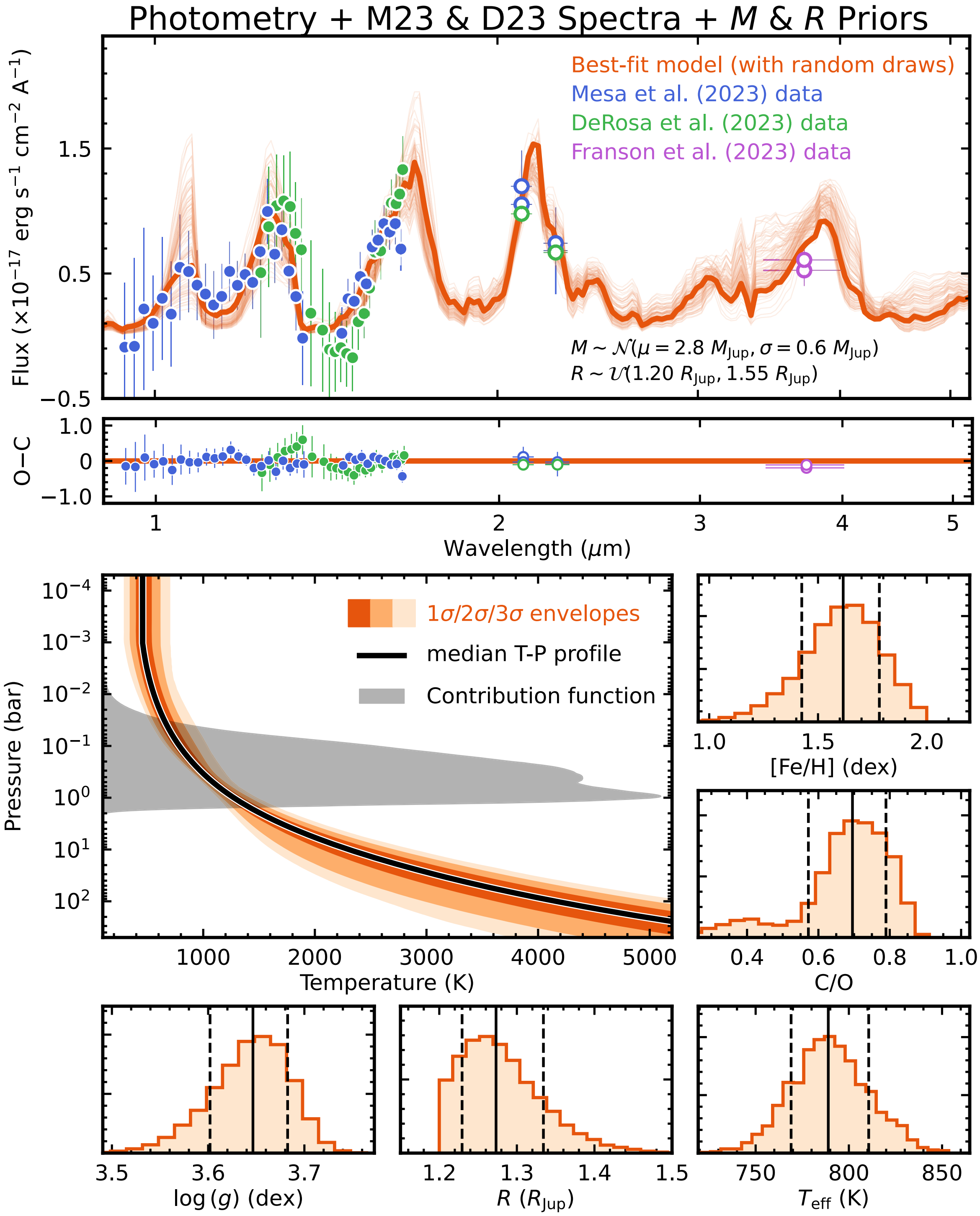

Figure 9. Results of the retrieval analysis on $K1/K2/L'$ photometry and both the Mesa et al. (2023) and De Rosa et al. (2023) spectra of AF Lep b (Section 7.2), with the same format as Figure 7.

spectrum by Mesa et al. (2023), the De Rosa et al. (2023) spectrum has overall higher fluxes (Figure 1) and the fluxes near the peaks of the J and H bands are slightly higher than the $K1/K2$ photometry, leading to a spectral slope indicative of a cloudless atmosphere. However, with constrained priors on M and/or R, the mass fraction of the $\mathrm{MgSiO_3}$ cloud significantly increases from −5.2 dex to −1.8 dex at the base pressure. This result suggests that the silicate cloud plays a more crucial role than Fe and KCl in shaping the planet's emission spectrum, as also suggested by the retrievals described in Section 7.1.

7.3. Retrievals on the $K1/K2/L'$ Photometry and Both the Mesa et al. (2023) and De Rosa et al. (2023) Spectra

By including an additive flux offset to each IFS spectrum, our retrieval analysis successfully explains all available photometry and spectra of AF Lep b with the fitted model spectra (Figure 9). Similar to the retrievals described in Sections 7.1 and 7.2, the retrieved [Fe/H] of AF Lep b is enhanced as compared to its host star's metallicity and this planet's atmosphere is likely influenced by silicate clouds (e.g.,

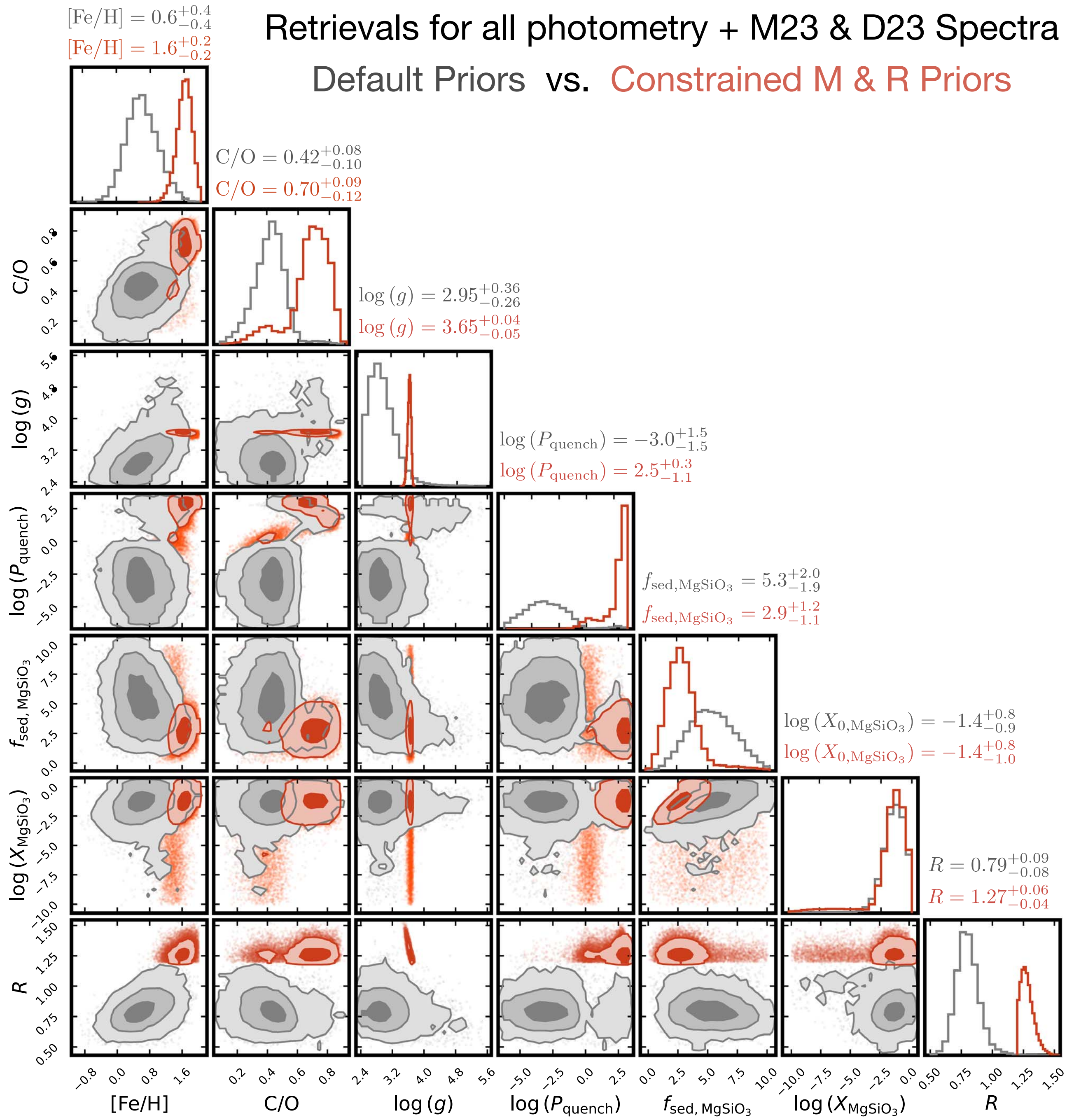

Figure 10. Corner plot for the retrieval runs performed with default parameter priors (gray) and with constrained priors on the planet's mass, $\mathcal{N}(\mu = 2.8\ M_{\mathrm{Jup}}, \sigma = 0.6\ M_{\mathrm{Jup}})$, and radius, $\mathcal{U}(1.20\ R_{\mathrm{Jup}}, 1.55\ R_{\mathrm{Jup}})$ (orange). We show $1\sigma/2\sigma/3\sigma$ confidence intervals for parameters inferred by the former retrieval (with default priors), but only present $1\sigma/2\sigma$ confidence intervals for the latter in order to prevent visual overlap. Both retrieval runs are performed on $K1/K2/L'$ photometry and both the Mesa et al. (2023) and De Rosa et al. (2023) spectra (Section 7.3).

$\mathrm{MgSiO_3}$), with a mass fraction around −1.4 dex at base pressure and an f_{sed} around 3. The presence of disequilibrium chemistry is strongly suggested only when the constrained priors on both M and R are adopted. In addition, our retrievals suggest that a positive flux offset for the Mesa et al. (2023) spectrum and a negative flux offset for the De Rosa et al. (2023) spectrum are required for the models to simultaneously explain all the spectrophotometry of AF Lep b.

For the interpretation of our analysis in the following section, we adopt the retrieval results inferred by combining all archival photometry and spectroscopy, with constrained priors for both M and R incorporated (unless otherwise noted). However, we note that if any atmospheric properties have vastly inconsistent inferred values among all the nine retrieval runs (e.g., C/O), then these parameters should be interpreted with caution.

8. Discussion

8.1. Formation Pathway of AF Lep b

8.1.1. Potential Metal Enrichment

After investigating the population-level trends between the masses of gas-giant exoplanets and the metallicities of their

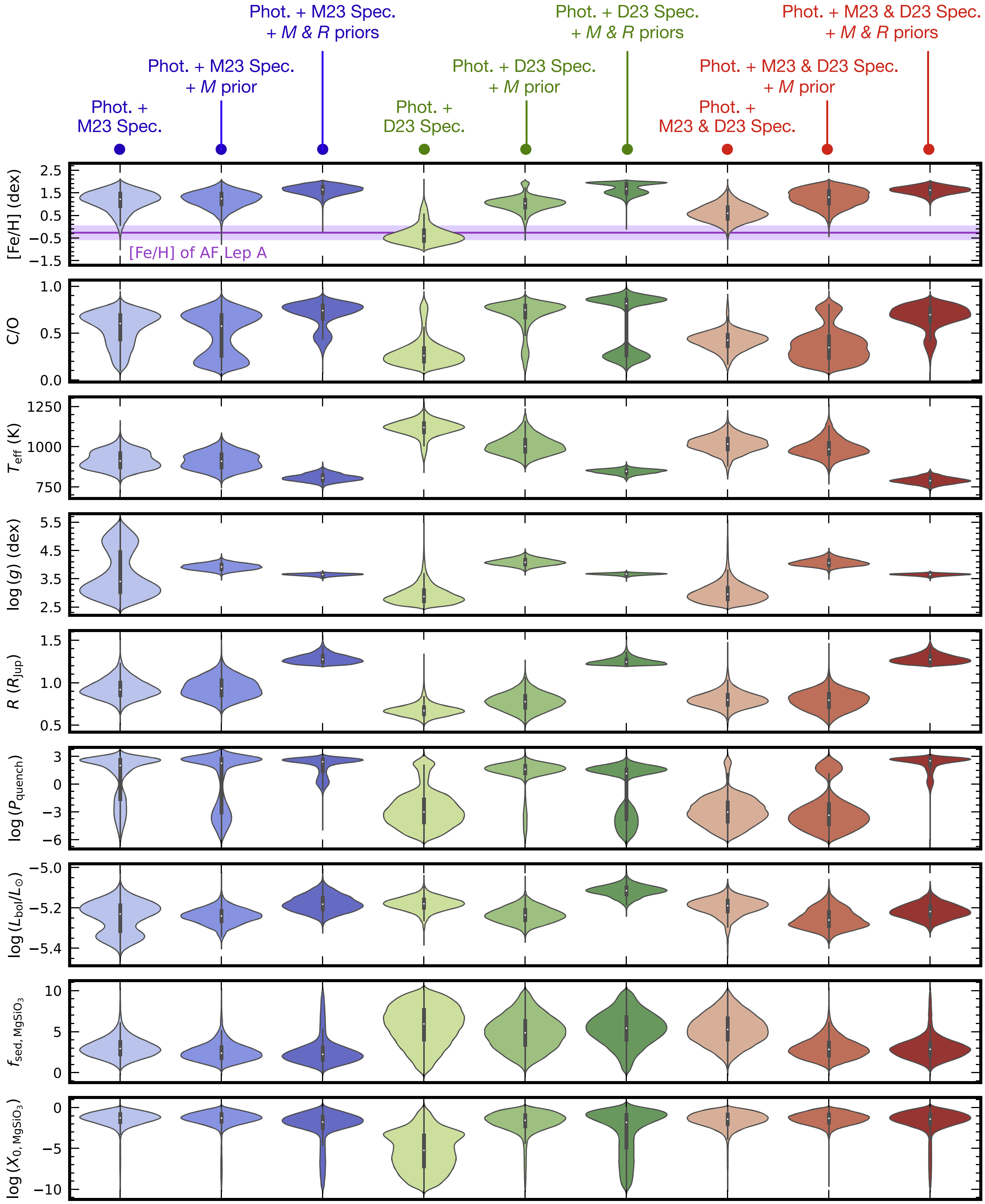

Figure 11. Violin plot for the posteriors of several key physical and chemical parameters derived from all the nine retrieval runs (Section 7). The left three columns (blue) correspond to the retrievals on the $K1/K2/L'$ photometry and the Mesa et al. (2023) spectrum (Section 7.1). The middle three columns (green) correspond to the retrievals on the $K1/K2/L'$ photometry and the De Rosa et al. (2023) spectrum (Section 7.2). The right three columns (red) correspond to the retrievals on the $K1/K2/L'$ photometry and both the Mesa et al. (2023) and De Rosa et al. (2023) spectra. Plots with darker blue/green/red colors suggest the addition of narrower and constrained priors on M (slightly darker) or both M and R (much darker). The measured [Fe/H] of the host star AF Lep A (-0.27 ± 0.31 dex, Section 3) is shown as a purple shade in the top panel.

Table 6
Retrieved Atmospheric Properties of AF Lep b

Parameter	Default Priors (Table 5)			Plus Constrained M Prior			Plus Constrained M and R Priors		
	Phot. + M23 Spec.	Phot. + D23 Spec.	Phot. + M23&D23 Spec.	Phot. + M23 Spec.	Phot. + D23 Spec.	Phot. + M23&D23 Spec.	Phot. + M23 Spec.	Phot. + D23 Spec.	Phot. + M23&D23 Spec.
Retrieved Physical and Chemical Properties									
[Fe/H]	$1.2^{+0.4}_{-0.5}$	$-0.4^{+0.5}_{-0.3}$	$0.6^{+0.4}_{-0.4}$	$1.2^{+0.3}_{-0.4}$	$1.0^{+0.2}_{-0.3}$	$1.3^{+0.4}_{-0.4}$	$1.6^{+0.2}_{-0.2}$	$1.7^{+0.3}_{-0.3}$	$1.6^{+0.2}_{-0.2}$
C/O	$0.60^{+0.12}_{-0.26}$	$0.26^{+0.14}_{-0.09}$	$0.42^{+0.08}_{-0.10}$	$0.57^{+0.15}_{-0.37}$	$0.75^{+0.06}_{-0.17}$	$0.34^{+0.19}_{-0.15}$	$0.74^{+0.07}_{-0.23}$	$0.82^{+0.05}_{-0.58}$	$0.70^{+0.09}_{-0.12}$
$\log(g)$	$3.40^{+1.37}_{-0.51}$	$2.87^{+0.37}_{-0.23}$	$2.95^{+0.36}_{-0.26}$	$3.92^{+0.12}_{-0.12}$	$4.08^{+0.13}_{-0.12}$	$4.06^{+0.14}_{-0.11}$	$3.65^{+0.04}_{-0.05}$	$3.66^{+0.03}_{-0.04}$	$3.65^{+0.04}_{-0.05}$
R	$0.92^{+0.13}_{-0.10}$	$0.67^{+0.07}_{-0.06}$	$0.79^{+0.09}_{-0.08}$	$0.93^{+0.13}_{-0.12}$	$0.78^{+0.10}_{-0.11}$	$0.79^{+0.11}_{-0.12}$	$1.27^{+0.06}_{-0.04}$	$1.24^{+0.05}_{-0.03}$	$1.27^{+0.06}_{-0.04}$
$\log(P_{\rm quench}/1\ {\rm bar})$	$2.0^{+0.7}_{-4.8}$	$-3.0^{+2.0}_{-1.6}$	$-3.0^{+1.5}_{-1.5}$	$2.3^{+0.6}_{-6.1}$	$1.6^{+0.5}_{-0.7}$	$-3.4^{+2.3}_{-1.4}$	$2.4^{+0.3}_{-1.9}$	$1.1^{+0.6}_{-5.6}$	$2.5^{+0.3}_{-1.1}$
Derived Physical Properties									
$T_{\rm eff}$	912^{+67}_{-52}	1120^{+41}_{-45}	1017^{+50}_{-52}	910^{+60}_{-53}	1002^{+63}_{-50}	984^{+62}_{-46}	806^{+26}_{-21}	848^{+13}_{-17}	789^{+22}_{-20}
$\log(L_{\rm bol}/L_\odot)$	$-5.23^{+0.06}_{-0.11}$	$-5.18^{+0.03}_{-0.03}$	$-5.19^{+0.04}_{-0.04}$	$-5.24^{+0.04}_{-0.04}$	$-5.24^{+0.04}_{-0.04}$	$-5.26^{+0.06}_{-0.04}$	$-5.18^{+0.05}_{-0.04}$	$-5.11^{+0.03}_{-0.03}$	$-5.22^{+0.04}_{-0.04}$
Cloud Properties									
$f_{\rm sed,MgSiO_3}$	$2.9^{+1.3}_{-1.0}$	$5.9^{+2.4}_{-2.9}$	$5.3^{+2.0}_{-1.9}$	$2.4^{+1.1}_{-0.9}$	$4.9^{+2.2}_{-2.1}$	$2.8^{+1.3}_{-1.1}$	$2.2^{+1.4}_{-0.9}$	$5.4^{+2.0}_{-2.1}$	$2.9^{+1.2}_{-1.1}$
$f_{\rm sed,Fe}$	$5.3^{+2.4}_{-2.5}$	$6.4^{+2.1}_{-2.7}$	$5.3^{+2.5}_{-2.6}$	$5.8^{+2.3}_{-2.8}$	$5.4^{+2.7}_{-2.8}$	$5.3^{+2.5}_{-2.6}$	$5.6^{+2.4}_{-2.7}$	$5.5^{+2.7}_{-2.9}$	$5.8^{+2.3}_{-2.6}$
$f_{\rm sed,KCl}$	$4.6^{+2.7}_{-2.4}$	$4.7^{+2.9}_{-2.7}$	$4.5^{+2.7}_{-2.5}$	$4.8^{+2.7}_{-2.4}$	$5.2^{+2.8}_{-2.9}$	$5.1^{+2.7}_{-2.8}$	$4.6^{+2.8}_{-2.5}$	$5.2^{+2.9}_{-3.0}$	$5.1^{+2.6}_{-2.7}$
$\log(X_{0,{\rm MgSiO_3}})$	$-1.3^{+0.7}_{-0.8}$	$-5.2^{+2.4}_{-2.7}$	$-1.4^{+0.8}_{-0.9}$	$-1.3^{+0.7}_{-0.8}$	$-1.6^{+0.9}_{-1.1}$	$-1.3^{+0.7}_{-0.8}$	$-1.8^{+0.9}_{-1.5}$	$-1.8^{+1.2}_{-4.7}$	$-1.4^{+0.8}_{-1.0}$
$\log(X_{0,{\rm Fe}})$	$-5.6^{+2.7}_{-2.3}$	$-3.2^{+1.7}_{-3.4}$	$-6.1^{+2.7}_{-2.1}$	$-5.1^{+2.9}_{-2.7}$	$-5.5^{+3.0}_{-2.6}$	$-5.3^{+2.7}_{-2.5}$	$-5.6^{+2.8}_{-2.5}$	$-5.4^{+3.0}_{-2.8}$	$-4.6^{+2.6}_{-2.8}$
$\log(X_{0,{\rm KCl}})$	$-6.1^{+2.2}_{-2.0}$	$-5.4^{+2.8}_{-2.6}$	$-4.6^{+2.5}_{-2.7}$	$-5.6^{+2.2}_{-2.2}$	$-6.2^{+2.2}_{-2.1}$	$-5.8^{+2.3}_{-2.2}$	$-6.3^{+2.2}_{-2.0}$	$-6.2^{+2.6}_{-2.3}$	$-6.4^{+2.1}_{-1.9}$
$\log(K_{zz})$	$8.1^{+1.6}_{-1.3}$	$8.8^{+1.8}_{-1.9}$	$8.6^{+1.9}_{-1.9}$	$8.9^{+1.5}_{-1.8}$	$8.5^{+1.6}_{-1.8}$	$8.5^{+1.5}_{-1.7}$	$8.7^{+1.5}_{-1.4}$	$8.0^{+2.7}_{-1.8}$	$8.5^{+1.6}_{-1.5}$
σ_g	$1.2^{+0.4}_{-0.1}$	$1.2^{+0.5}_{-0.2}$	$1.2^{+0.5}_{-0.2}$	$1.2^{+0.5}_{-0.2}$	$1.2^{+0.5}_{-0.2}$	$1.2^{+0.5}_{-0.2}$	$1.2^{+0.5}_{-0.2}$	$1.3^{+0.6}_{-0.2}$	$1.3^{+0.5}_{-0.2}$
Flux Offsets of Spectroscopic Data Set									
$\Delta f_{\rm M23} \times 10^{18}$	…	…	$1.3^{+0.9}_{-0.7}$	…	…	$1.3^{+0.8}_{-0.6}$	…	…	$0.4^{+0.5}_{-0.5}$
$\Delta f_{\rm D23} \times 10^{18}$	…	…	$-3.6^{+0.9}_{-0.8}$	…	…	$-3.6^{+0.8}_{-0.6}$	…	…	$-4.6^{+0.6}_{-0.6}$
T–P Profile Properties									
$T_{\rm bottom}$	8257^{+984}_{-1996}	8719^{+721}_{-915}	8908^{+605}_{-728}	8043^{+979}_{-990}	7113^{+1031}_{-845}	8578^{+728}_{-954}	7205^{+1065}_{-1230}	8015^{+1285}_{-1100}	7392^{+908}_{-996}
$(d\ln T/d\ln P)_1$	$0.25^{+0.02}_{-0.02}$	$0.25^{+0.02}_{-0.02}$	$0.25^{+0.02}_{-0.02}$	$0.25^{+0.02}_{-0.02}$	$0.25^{+0.02}_{-0.02}$	$0.25^{+0.02}_{-0.02}$	$0.25^{+0.02}_{-0.02}$	$0.25^{+0.02}_{-0.02}$	$0.25^{+0.02}_{-0.02}$
$(d\ln T/d\ln P)_2$	$0.24^{+0.02}_{-0.02}$	$0.25^{+0.03}_{-0.02}$	$0.24^{+0.02}_{-0.02}$	$0.25^{+0.02}_{-0.02}$	$0.25^{+0.03}_{-0.03}$	$0.24^{+0.02}_{-0.02}$	$0.25^{+0.03}_{-0.03}$	$0.24^{+0.03}_{-0.03}$	$0.25^{+0.02}_{-0.03}$
$(d\ln T/d\ln P)_3$	$0.27^{+0.03}_{-0.03}$	$0.24^{+0.03}_{-0.03}$	$0.26^{+0.02}_{-0.02}$	$0.26^{+0.03}_{-0.03}$	$0.26^{+0.04}_{-0.04}$	$0.26^{+0.03}_{-0.03}$	$0.25^{+0.03}_{-0.05}$	$0.27^{+0.04}_{-0.04}$	$0.26^{+0.03}_{-0.04}$
$(d\ln T/d\ln P)_4$	$0.18^{+0.05}_{-0.03}$	$0.15^{+0.02}_{-0.02}$	$0.16^{+0.02}_{-0.02}$	$0.18^{+0.04}_{-0.03}$	$0.19^{+0.04}_{-0.04}$	$0.17^{+0.03}_{-0.03}$	$0.19^{+0.04}_{-0.08}$	$0.20^{+0.02}_{-0.03}$	$0.20^{+0.03}_{-0.04}$
$(d\ln T/d\ln P)_5$	$0.10^{+0.03}_{-0.03}$	$0.10^{+0.03}_{-0.03}$	$0.08^{+0.02}_{-0.02}$	$0.12^{+0.03}_{-0.04}$	$0.13^{+0.04}_{-0.04}$	$0.11^{+0.04}_{-0.05}$	$0.13^{+0.03}_{-0.04}$	$0.13^{+0.03}_{-0.04}$	$0.13^{+0.03}_{-0.03}$
$(d\ln T/d\ln P)_6$	$0.07^{+0.05}_{-0.05}$	$0.07^{+0.05}_{-0.05}$	$0.06^{+0.05}_{-0.05}$	$0.07^{+0.05}_{-0.05}$	$0.07^{+0.06}_{-0.06}$	$0.08^{+0.05}_{-0.05}$	$0.07^{+0.05}_{-0.05}$	$0.07^{+0.06}_{-0.06}$	$0.06^{+0.05}_{-0.05}$

Notes. The properties listed in the last column are recommended as the nominal atmospheric properties of AF Lep b, given that these results are determined by combining all of the planet's available spectrophotometry with its independently measured dynamical mass and age incorporated. However, we note that if any atmospheric properties have vastly inconsistent inferred values among all these nine retrieval runs (e.g., C/O), then they should be interpreted with caution.

host stars, Schlaufman (2018) suggested that core accretion and gravitational instabilities—the two dominant planet formation mechanisms—might operate at distinct mass regimes. They found gas giants with masses below 4–10 $M_{\rm Jup}$ likely formed via core accretion, while those with higher masses likely formed via gravitational instabilities. Although such critical planet mass differs in other studies (e.g., Sahlmann et al. 2011; Santos et al. 2017), the range of 4–10 $M_{\rm Jup}$ is among the lowest values. Therefore, based on the dynamical mass measurement of $2.8^{+0.6}_{-0.5}$ $M_{\rm Jup}$, AF Lep b is likely a product of core accretion according to Schlaufman (2018).

The enhanced metallicity of AF Lep b as compared to its host star, as revealed by our study, also lines up with the core accretion formation scenario. As shown in Figure 11, our retrieved [Fe/H] of AF Lep b is higher than the [Fe/H] of AF Lep A at a 1.9σ–5.3σ significance, regardless of (1) whether the individual spectrum from Mesa et al. (2023) or De Rosa et al. (2023), or both spectra are included in the retrievals, and (2) whether constrained and physically driven priors on the planet's mass, or both mass and radius, are adopted.[18] The only exception occurs when we perform a retrieval run using all the photometry and only the De Rosa et al. (2023) spectrum, without constrained priors on the planet's mass or radius; in this case, the inferred [Fe/H] of the planet and the host star are consistent within 0.4σ. However, this run also predicts a mass of $0.13^{+0.17}_{-0.05}$ $M_{\rm Jup}$ based on the retrieved $\log(g)$ and R, which is 4.3σ lower than the planet's

---

[18] As a reminder, the constrained mass prior is a Gaussian prior based on the directly measured dynamical mass, $\mathcal{N}(\mu = 2.8\ M_{\rm Jup},\ \sigma = 0.6\ M_{\rm Jup})$, and the constrained radius prior is a uniform prior contextualized by the evolution model analysis, $\mathcal{U}(1.20\ R_{\rm Jup},\ 1.55\ R_{\rm Jup})$; these are introduced in Section 7. Incorporating these priors allows the retrieval results to become consistent with observations beyond spectrophotometry and match the physical expectations.

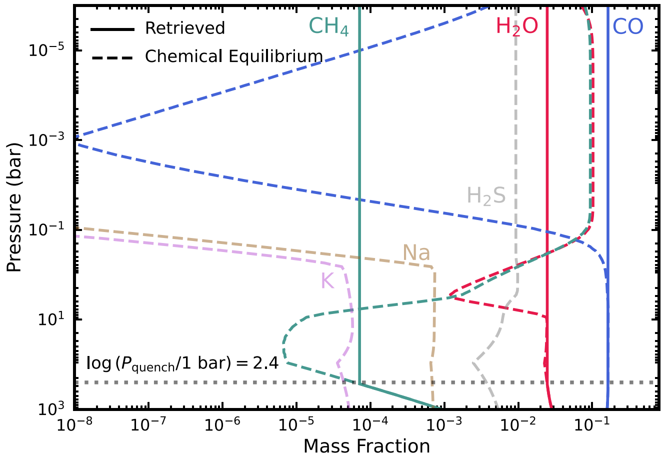

Figure 12. The abundance of several key species (solid) inferred from the retrieval performed on the $K1/K2/L'$ photometry and the Mesa et al. (2023) spectrum, along with constrained priors on the planet's mass and radius (Section 7.1). These profiles correspond to the median values of the parameters as summarized in Table 6, including a quenching pressure at $10^{2.4}$ bar. Dashed lines present the abundances under chemical equilibrium. For H_2O, CO, and CH_4, our retrieved profiles suggest evidence of disequilibrium chemistry in the atmosphere of AF Lep b; for the other species (e.g., Na, K, and H_2S), we assume their abundances follow the equilibrium chemistry in our retrievals (see Section 6.3).

measured dynamical mass, thus undermining the accuracy of its inferred planet metallicity. The enhanced [Fe/H] of AF Lep b is also supported by the brighter K-band flux compared to the fluxes at shorter wavelengths, as seen in the retrievals for the Mesa et al. (2023) spectrum and both spectra (with offsets applied). The photosphere with a metal-rich composition resides at lower pressures, where the collision-included absorption of H_2–H_2 and H_2–He becomes weaker, leading to higher K-band fluxes (e.g., Fortney et al. 2008; also see Figure 6).

Metal enrichment is consistent with the predictions of core accretion models of planet formation and has been suggested for the solar system's giant planets (e.g., Alibert et al. 2005; Helled & Bodenheimer 2014), as well as for extrasolar planets (e.g., Miller & Fortney 2011; Mordasini et al. 2014; Thorngren et al. 2016; Thorngren & Fortney 2019). Building on the work of Miller & Fortney (2011), Thorngren et al. (2016) studied the composition of a sample of transiting planets with directly measured masses and radii, finding an anticorrelation between the metal enrichment of gas-giant planets ($Z_{\rm planet}/Z_{\rm star}$) and the planets' mass (also see Teske et al. 2019). The enhanced metallicity of gas giants can result from the accretion of pebbles and planetesimals (Owen et al. 1999; Alibert et al. 2005; Zhou & Lin 2007; Helled & Bodenheimer 2014; Atreya et al. 2016; Mousis et al. 2021; Schneider & Bitsch 2021b), which are composed of volatile and refractory materials with slightly different characteristics. Pebbles are coupled to gas and can be accreted into gas giants' atmospheres along with the gas until the planet is sufficiently massive to open a gap. Also, pebbles can drift inward across ice lines within the protoplanetary disk, followed by the evaporation that alters the chemical content of the disk gas and thereby the gas-giant planets' atmospheres (e.g., Schneider & Bitsch 2021a). In contrast, planetesimals have larger sizes and are less affected by aerodynamic gas drag, allowing planetesimal accretion to occur during the late stage of planet formation when pebble accretion is halted (see reviews by Helled et al. 2014; Drazkowska et al. 2022).

Indeed, planetesimal accretion and the resulting metal enrichment of planets are not an exclusive outcome of core accretion, but can also occur for planets formed via gravitational instabilities (e.g., Guillot & Gladman 2000; Helled et al. 2006; Helled & Schubert 2009; Boley & Durisen 2010; Helled & Bodenheimer 2010). In addition, as discussed in Thorngren et al. (2016), metal enrichment might result from the gap opening of planets and the subsequent starvation of gas accretion.

Based on our analysis, AF Lep b has an enhanced metallicity as compared to its host star by a factor of $Z_{\rm planet}/Z_{\rm star} = 75^{+94}_{-42}$.[19] At a mass of approximately 2.8 $M_{\rm Jup}$, this inferred metal enrichment of AF Lep b is higher than the median level of the exoplanet sample studied in Thorngren et al. (2016), although several planets in that work exhibited similarly high metal enrichment. It is possible that both pebble and planetesimal accretion impact the formation and early evolution of AF Lep b, leading to its enhanced metallicity. In particular, the late-stage planetesimal accretion also coincides with the presence of a debris disk in the planetary system at 40–60 au (Pawellek et al. 2021; Pearce et al. 2022), which suggests a potentially large metal reservoir in the disk. As discussed by Franson et al. (2023b), at its currently observed orbit, AF Lep b has a sufficient mass to dynamically stir the debris disk, triggering planetesimal collisions that potentially replenish the dust. We note that some of these planetesimals may be scattered inward and bombard the planet's atmosphere to enrich its atmospheric metallicity.

An alternative explanation for AF Lep b's enhanced atmospheric metallicity is the possibility of giant impacts and planetary mergers (e.g., Ginzburg & Chiang 2020; Ali-Dib et al. 2022). These events could be common occurrences during the advanced evolution stages of protoplanetary disks and might also lead to core erosion, the stripping of planets' hydrogen and helium envelopes, and altered orbital architecture of planetary systems (e.g., Lin & Ida 1997; Li et al. 2010; Liu et al. 2015; Biersteker & Schlichting 2019; Frelikh et al. 2019; Liu et al. 2019).

In addition, it is likely that AF Lep b has a diluted core, similar to gas and ice giants in the solar system (e.g., Marley et al. 1995; Helled et al. 2011; Wahl et al. 2017; Debras & Chabrier 2019) and likely to exoplanets as well (e.g., Thorngren & Fortney 2019). In this scenario, heavy elements from the planetary interior mix with the atmospheres, leading to enhanced atmospheric metallicity. Thorngren & Fortney (2019) studied the metal enrichment of exoplanets as a function of planet mass with different levels of interior-atmosphere mixing. At a mass of 2.8 $M_{\rm Jup}$, our inferred $Z_{\rm planet}/Z_{\rm star}$ of AF Lep b lines up with the maximum metal enrichment values, as shown in Thorngren & Fortney (2019), when assuming the interior and the atmosphere are fully mixed.

Beyond [Fe/H], comparing the C/O of AF Lep b and AF Lep A provides additional constraints to the planet formation pathways, including the initial formation location and the relative gas and dust accreted to assemble the planet's mass (e.g., Öberg et al. 2011; Madhusudhan et al. 2014, 2017; Schneider & Bitsch 2021b; Mollière et al. 2022). However,

---

[19] To derive this metal enrichment factor, we use the [Fe/H] chain retrieved from a run that incorporates all archival photometry and both spectra of AF Lep b, with constrained priors on the planet's mass and radius. We randomly draw the host star's [Fe/H] from a Gaussian distribution with an equal sample size to the planet's [Fe/H].

studying the C/O for this particular system is complicated by the difficulty in constraining the stellar C/O due to strong stellar rotation, which weakens and blends the characteristic lines of C and O (Section 3.3). In addition, the inferred C/O values of AF Lep b are less consistent among the different retrieval runs compared to the case of [Fe/H] (Figure 11). Also, when retrieving the De Rosa et al. (2023) spectrum with constrained priors on the planet's mass and radius, a bimodal distribution is seen in the C/O posterior. These two modes correspond to a supersolar and a subsolar C/O, even though the host star does not necessarily have a solar C/O. Extending the spectrophotometry of AF Lep b to a wider range of wavelengths with a higher signal-to-noise ratio (S/N) and/or spectral resolution may help to further constrain the planet's C/O and refine other atmospheric parameters.

8.1.2. Planet Formation at a Later Epoch?

Here we compare the physical properties of AF Lep b inferred by the evolution models (Section 5 and Table 3) and atmospheric retrievals (Section 7 and Table 6). As discussed in Section 5.1, discrepancies between evolution models and atmospheric models are well recognized in the field. One specific example of discrepancy is that the radii and surface gravities inferred by atmospheric models can be inconsistent with the object's independently known age and mass. Indeed, as shown in Table 6, if constrained priors on the planet's mass and radius are not incorporated, then our retrievals can derive unphysically small radii (down to 0.67 $R_{\rm Jup}$) or too low $\log(g)$ that lead to a Saturn-like mass, which is incompatible with the planet's orbit.

It is these discrepancies that have motivated us to adopt constrained priors on the planet's M and R, in order to reliably characterize the atmospheric properties. However, even with these constrained priors, there are still differences between the retrieved effective temperature and bolometric luminosity and those estimated by various evolution models. Specifically, our retrievals infer 100–350 K hotter effective temperature and 0.2–1.0 dex brighter bolometric luminosity, when compared to those of the evolution models analyzed in Section 5 (i.e., comparing the last three columns of Table 6 to Table 3).

One possibility to reconcile these differences is if AF Lep b formed later than its host star, which would lead to a younger age of the planet and consequently increase the evolution-based $T_{\rm eff}$ and $L_{\rm bol}$. For hot-start evolution models, a 10 Myr younger age of AF Lep b significantly resolves the discrepancies (see Table 7), even though such a delayed planet formation timescale exceeds the typical lifetime of protoplanetary disks (e.g., Mamajek 2009). This scenario was also previously suggested by Franson et al. (2023b) albeit based on comparisons among a different set of parameters. Specifically, they found that if AF Lep b formed 5–15 Myr after its host star did, then this planet's directly measured dynamical mass would be consistent with the mass predicted by several hot-start evolution models at the planet's age and an estimated bolometric luminosity.[20] For cold-start evolution models (Spiegel & Burrows 2012; Marley et al. 2021; see Table 7), however, a 10 Myr younger age for the planet only slightly reduces the discrepancies between our retrieved and evolution-based $T_{\rm eff}$ and $L_{\rm bol}$ by about 30%.

Another possibility is the occurrence of giant impacts and planetary mergers during the evolution history of AF Lep b, which is also a candidate explanation of the planet's metal enrichment (see Section 8.1.1). In this scenario, the dissipation of kinematic energy into the planet's atmosphere and interior might act as a mechanism of rejuvenation, by altering its entropy state (also see Ginzburg & Chiang 2020). This process can potentially result in elevated values for both the bolometric luminosity and the effective temperature that deviate from the predictions of evolution models at the planet's current age. A thorough quantitative analysis would be useful to assess the viability of this hypothesis.

Acquiring new spectrophotometry of AF Lep b with a wider wavelength coverage than that of the existing data will provide more detailed information about the spectrum and bolometric flux of this planet. Such observation might in turn help to refine the $T_{\rm eff}$ and $\log(L_{\rm bol}/L_{\odot})$ inferred by retrievals. Also, ongoing theoretical advancements in the evolution models for planets formed via core accretion, incorporating different assumptions about the planetary atmospheres, will lead to a better understanding of the physical properties of such planets (e.g., Mordasini et al. 2017; Emsenhuber et al. 2021). The combination of observational and theoretical progress of exoplanets will be a topic of continuing research, and will bring insights into the discrepancies between the predictions of retrievals and evolution models as seen in AF Lep b.

8.2. AF Lep b as an Exceptional Planet Straddling the L/T Transition

8.2.1. Refined Spectral Type of AF Lep b

To derive the spectral type of AF Lep b, Mesa et al. (2023) compared their observed SPHERE/IFS spectrum and the $K1/K2$ photometry to a spectral library of ultracool dwarfs, finding that spectral templates with L6–L6.5 types yield the best match. De Rosa et al. (2023) performed a similar analysis using their own observations and found a spectral type of L9–T0.5. The difference in spectral type inferred by these two studies is mainly caused by the distinct fluxes of their observed spectra (Figure 1). By accounting for the directly measured dynamical mass of the planet and the age of the planetary system, our retrieval analysis has now determined flux offsets that effectively combine the two sets of spectra. Therefore, in this section, we refine the spectral type of AF Lep b by combining all its observed spectrophotometry. The flux offset of each IFS spectrum is set to the best-fit value determined by the retrieval run that uses all observations and adopts constrained priors on the planet's mass and age (see Section 7.3).

We compare the SED of AF Lep b to IRTF/SpeX spectra of M5–T9 ultracool dwarfs over a wavelength range of 0.9–2.3 μm following Zhang et al. (2021c). A total of 930 ultracool dwarfs, or spectral templates, are selected from the UltracoolSheet (Best et al. 2020b) as long as they are not resolved/candidate binaries and have good-quality spectra with $S/N > 20$ per pixel in the J band. A scale factor for each template is computed to minimize the χ^2. As shown in Figure 13, the fitted templates with the lowest χ^2 have L6.5–L7 types and are all unusually red and young planetary-mass objects, including WISEP J004701.06

---

[20] Franson et al. (2023b) estimated the bolometric luminosity of AF Lep b as $\log(L_{\rm bol}/L_{\odot}) = -4.81 \pm 0.13$ dex, using the L'-band absolute magnitude, with a bolometric correction assumed to match that of HR 8799 b. Their estimated bolometric luminosity is significantly brighter than the values inferred by our retrievals based on different portions of the planet's spectrophotometry (e.g., -5.22 ± 0.04 dex; Table 6); it is possible that the bolometric corrections required by HR 8799 b and AF Lep b are different. New spectroscopy or photometry in longer wavelengths will be useful to refine the planet's bolometric luminosity.

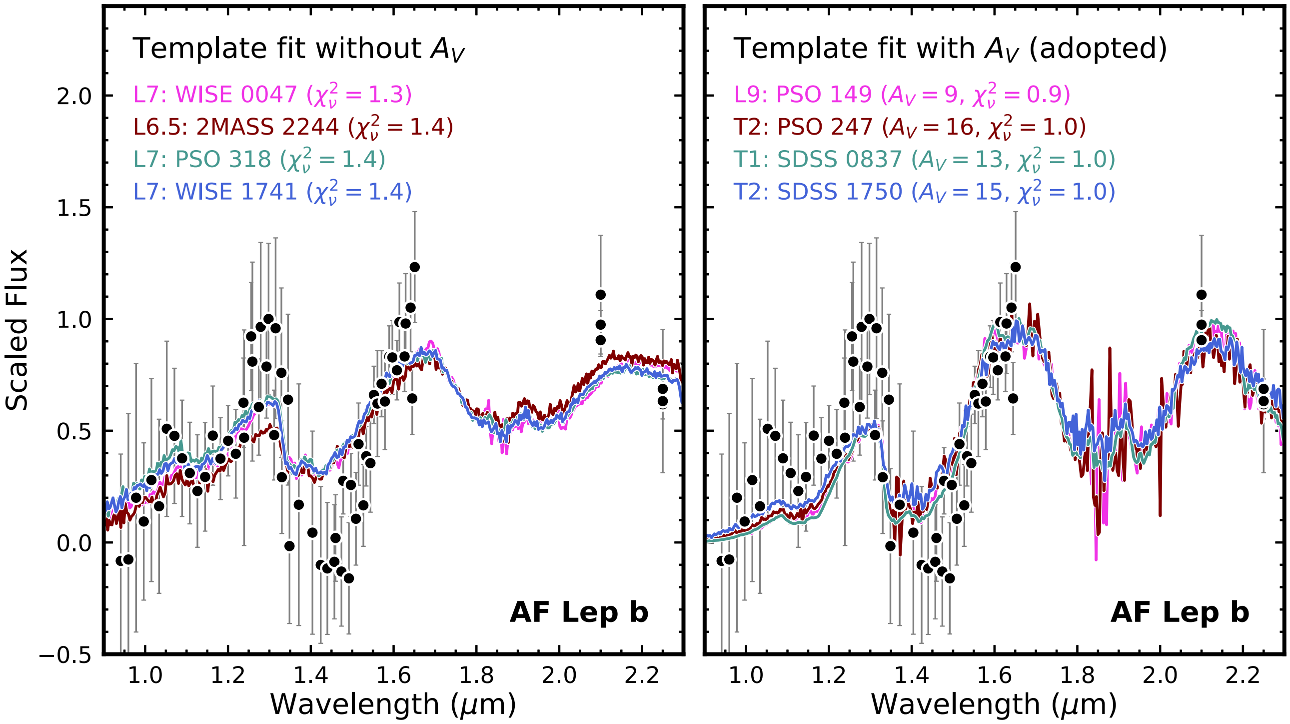

Figure 13. Spectrophotometry of AF Lep b (black) compared to the top four best-matched ultracool dwarfs obtained from the template fitting that does not (left) and does (right) incorporate the reddening law of the interstellar medium, which we use to mimic the cloud effect for the purpose of spectral typing.

+680352.1 (Gizis et al. 2012), 2MASSW J2244316+204343 (Dahn et al. 2002), PSO J318.5338−22.8603 (Liu et al. 2013), and WISE J174102.78−464225.5 (Schneider et al. 2014).

However, mid-L templates cannot reproduce all the spectral features of AF Lep b. The H_2O absorption between the J and H bands of AF Lep b appears to be much deeper, suggestive of a colder effective temperature or a later spectral type. Also, the significant drop in flux from $K1$ to $K2$ is not well explained by the relatively flat spectral shape of the L6.5–L7 templates. This blue $K1$–$K2$ color lines up with a strong CH_4 absorption bandhead at 2.2 μm, indicative of a late-L and early-T type. These properties, along with the overall red spectral morphology of AF Lep b, suggest a cloudy object of an approximately T0 spectral type. However, such empirical spectral templates with high-quality S/N are lacking, particularly near the L/T transition, where ultracool dwarfs are inherently rare (e.g., Best et al. 2021).

To account for the cloud effect in the spectral typing process, the above template fitting is repeated with the Schlafly & Finkbeiner (2011) reddening law incorporated. This extinction law is developed for the interstellar medium and might qualitatively (though not quantitatively) demonstrate the effect of clouds on the emission spectroscopy (e.g., Figure 6). For each template, we explore a grid of V-band extinction spanning 0–30 mag with steps of 0.1 mag and identify the A_V that leads to the minimum χ^2. The inclusion of reddening leads to best-fit templates with L9–T2 types (Figure 13), which match better with AF Lep b in terms of the blue wing of the H band (shaped by H_2O absorption) and the blue $K1$–$K2$ color (potentially shaped by the CH_4 absorption). In the Y and J bands, the reddened templates appear to be systematically fainter, likely due to the extinction law of the interstellar medium not fully accounting for the cloud effect on self-luminous gas-giant planets. Nevertheless, the qualitatively good match in the H and K bands (which are less affected by clouds than shorter wavelengths) suggests a spectral type for AF Lep b near T0.

Based on the observed spectrophotometry, we adopt a spectral type of L8–T3 for AF Lep b. This range covers the top 5% of best-matched (reddened) spectral templates. This spectral type range is also later than the result inferred by the template fit not incorporating A_V, which cannot fully explain the deep H_2O absorption and blue $K1$–$K2$ color.

8.2.2. The Unusual Atmospheric Properties of AF Lep b

AF Lep b is an exceptional giant planet straddling the L/T transition. As shown in Figure 14, compared to older ultracool dwarfs with similar spectral types but higher surface gravities and larger masses, this planet has a 450–600 K colder effective temperature and a 0.6–0.9 dex fainter bolometric luminosity. Notably, AF Lep b is thus far the coldest object with suggested evidence of silicate clouds.

The peculiar properties of AF Lep b line up with its very low surface gravity (Table 3). As discussed in Zhang et al. (2020), the properties of objects near the L/T transition depend on their surface gravities. Objects with lower surface gravities tend to have colder $T_{\rm eff}$, fainter absolute magnitudes in the J and H bands, and slightly fainter bolometric luminosities than their older counterparts. This gravity dependence is particularly significant in late-L types but becomes weaker toward early-T types. With an L8–T3 spectral type (Section 8.2.1), AF Lep b maintains significant peculiarities, likely due to its remarkably low surface gravity of $\log(g) \approx 3.6$ dex. This $\log(g)$ is even 0.7 dex lower than those of previously known young and low-gravity T0–T5 ultracool dwarfs, including SIMP J013656.5+093347.3, 2MASS J13243553+6358281, GU Psc b, and SDSSp J111010.01+011613.1. Across the L and T spectral types, gas-giant planets that have the coldest $T_{\rm eff}$ and the faintest

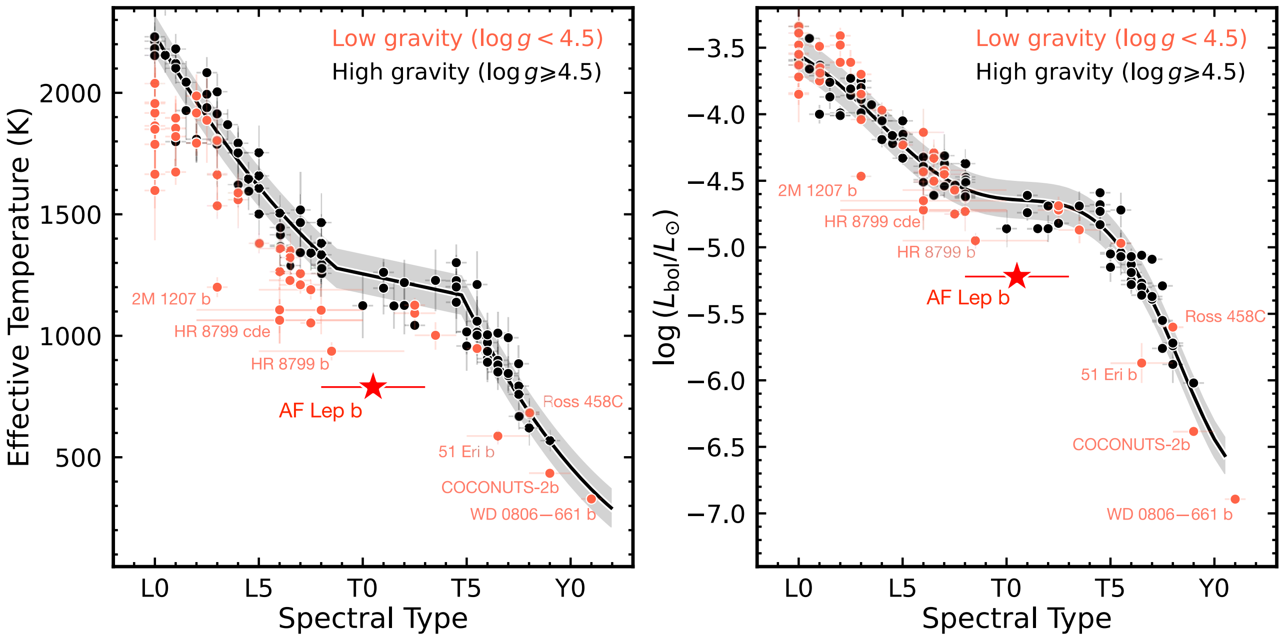

Figure 14. Effective temperature (left) and bolometric luminosity (right) of AF Lep b (red star) compared to those of other directly imaged planets, free-floating planets, and brown dwarfs, which are color-coded by their surface gravities (orange and black for $\log(g)$ below and above 4.5 dex, respectively); these $\log(g)$ of the comparison sample are obtained from Filippazzo et al. (2015) and Zhang et al. (2020, 2021c, 2021d). The plotted properties of AF Lep b are inferred by our retrieval analysis performed for the full spectrophotometry with constrained priors for the planet's mass and radius (i.e., the last column of Table 6). In both panels, we use black lines and gray shades to show the polynomials that convert spectral types to $T_{\rm eff}$ (Table 13 of Kirkpatrick et al. 2021) and to $L_{\rm bol}$ (footnote 16 of Zhang et al. 2020) in the high-gravity regime. AF Lep b is thus far the coldest exoplanet with suggested evidence of silicate clouds.

$L_{\rm bol}$ are consistently associated with the lowest surface gravities. Examples include 2MASS 1207 b ($\log(g) = 3.8 \pm 0.1$ dex, Filippazzo et al. 2015), HR 8799 b ($\log(g) = 4.1 \pm 0.2$ dex, Zhang et al. 2020) and cde ($\log(g) = 4.2 \pm 0.2$ dex, Zhang et al. 2020), AF Lep b ($\log(g) \approx 3.6$ dex, Table 3), 51 Eri b ($\log(g) = 3.55^{+0.55}_{-0.03}$ dex, Zhang et al. 2020), and COCONUTS-2b ($\log(g) = 4.11^{+0.11}_{-0.18}$ dex, Zhang et al. 2021d). The unusual physical properties of AF Lep b might be also linked to its metal-enriched atmosphere, suggesting the L/T transition is potentially metallicity dependent.

8.3. Retrieving Thermal Structures of Cloudy Atmospheres: Modeling Temperature or Temperature Gradient?

In the context of studying the thermal structure of imaged planets and brown dwarfs, retrieval studies often employ models that describe the temperature as a function of pressure to analyze observed data. Some studies parameterize the T–P profiles using explicit equations (e.g., Burningham et al. 2017, 2021; Lavie et al. 2017; Mollière et al. 2020; Wang et al. 2020; Gonzales et al. 2021, 2022; Brown-Sevilla et al. 2023; Xuan et al. 2022; Gaarn et al. 2023; Whiteford et al. 2023), while others directly fit the temperature at different atmospheric layers (e.g., Line et al. 2015, 2017; Zalesky et al. 2019, 2022; Zhang et al. 2021a, 2021b; Hood et al. 2023). In this work, we adopt an approach that models the temperature gradient, ($d \ln T / d \ln P$), which allows for the novel incorporation of RCE during the retrievals (Sections 6.1–6.2).

In this section, we conduct a comparative retrieval analysis for spectrophotometry of AF Lep b. There are two sets of retrievals: (1) we model the thermal structure in terms of the temperature gradient, as already established in Section 7, and (2) we explicitly model the temperature. We then compare the resulting thermal structures and atmospheric properties from these two approaches. For this experiment, we use all available photometry and both spectra from Mesa et al. (2023) and De Rosa et al. (2023), with an additive flux offset applied for each spectrum.

In the "modeling temperatures" approach, we use the thermal model of Mollière et al. (2020). The atmosphere is divided into the following three regions based on pressure P or optical depth τ, with a conversion of $\tau = \delta P^{\alpha}$; both δ and α are free parameters in this retrieval framework and P is in units of dyn cm^{-2}.

1. The photosphere region spans $\tau = 0.1$ to the radiative–convective boundary. The Eddington approximation is adopted, with the internal temperature $T_{\rm internal}$ added as a free parameter.
2. The low-altitude, troposphere region spans the bottom of the photosphere region to the bottom of the atmosphere (assumed as $P = 10^3$ bar). The T–P profile is forced on the moist adiabat.
3. The high-altitude region spans $P = 10^{-6}$ bar down to the top of the photosphere region and is divided into three layers evenly spaced in $\log(P)$. The temperatures of these layers, T_1, T_2, T_3 (from top to bottom), are all free parameters. A cubic spline interpolation is used to describe the thermal structure of this region.

There are six T–P parameters in total (δ, α, $T_{\rm internal}$, T_1, T_2, and T_3), and we set the same priors as Mollière et al. (2020) did in their retrieval analysis of the directly imaged planet HR 8799 e. The same chemistry and cloud models described in Section 6 are used. In addition, we adopt constrained priors for the planet's mass, $\mathcal{N}(\mu = 2.8\ M_{\rm Jup}, \sigma = 0.6\ M_{\rm Jup})$, and radius, $\mathcal{U}(1.20\ R_{\rm Jup}, 1.55\ R_{\rm Jup})$.

Figure 15 presents the retrieved T–P profiles from the two types of retrievals. While both retrieval analyses predict

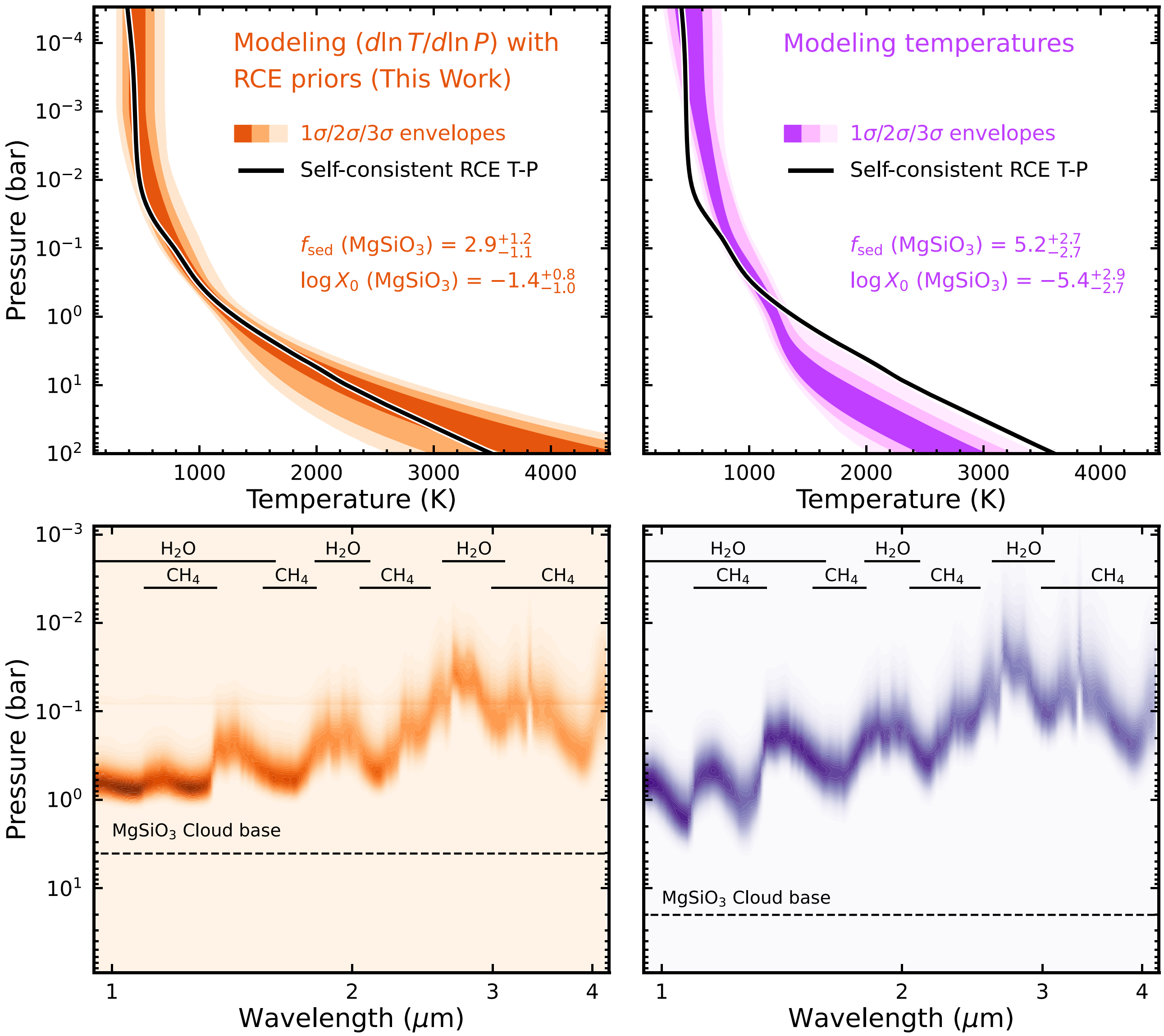

Figure 15. Top left: The retrieved *T*–*P* profiles (orange) with the atmospheric thermal structure modeled via the temperature gradient. The input data include the $K1/K2/L'$ photometry and both spectra of AF Lep b, with constrained *M* and *R* priors; thus, the retrieved *T*–*P* profiles shown here are exactly the same as the middle left panel of Figure 9. The $1\sigma/2\sigma/3\sigma$ confidence intervals are shown as orange shades. Overlaid is an RCE *T*–*P* profile (black) created at the median values of all parameters, which is consistent with the retrieved *T*–*P* profiles. Bottom left: Contribution function of the best-fit model for the retrieval shown in the top left panel. The 1–4 μm photosphere is located above 1 bar due to the cloud effect; the retrieved silicate cloud has a base pressure near 3 bar with a relatively small $f_{\rm sed}$ and large mass fraction. Top and bottom right: Retrieved *T*–*P* profiles and contribution function of the best-fit model (purple), with the atmospheric thermal structure modeled in terms of the temperature. In comparison, modeling the thermal structure via the temperature gradient offers the flexibility to incorporate an RCE prior and thereby better constraints on cloud properties.

emission spectra that match the observed spectrophotometry of AF Lep b, the “modeling temperatures” approach returns a more isothermal *T*–*P* profile compared to a self-consistent RCE profile generated at median parameter values. In addition, properties of cloud condensates cannot be constrained under this approach, with $f_{\rm sed}$ and $\log(X_0)$ primarily set by the priors. This result is consistent with the scenario proposed by Tremblin et al. (2016). Under this scenario, the atmospheres of L/T transition objects are impacted by the thermocompositional instabilities arising from the CO $\rightleftharpoons$ CH_4 disequilibrium chemistry, leading to a more isothermal *T*–*P* profile without invoking clouds (although this scenario has been challenged by Leconte 2018). However, the retrieved $\log(P_{\rm quench}) = -3.5^{+3.5}_{-1.5}$ dex from this approach does not strongly suggest evidence of chemical disequilibrium in the photosphere of AF Lep b, which does not line up with the Tremblin et al. (2016) scenario.[21]

In contrast, the “modeling temperature gradients” approach (corresponding to the last column in Table 6) returns *T*–*P* profiles that are consistent with the RCE profile within 1σ–2σ thanks to the RCE prior based on self-consistent forward models (Section 6.2). This approach suggests the presence of silicate clouds and the top layers of these clouds likely truncate the retrieved contribution function at around 1 bar (Figure 15).

This experiment does not aim to assess whether the Tremblin et al. (2016) scenario is applicable to the atmosphere of

---

[21] As a side note, this retrieval approach infers an [Fe/H] = 1.6 ± 0.2 dex for AF Lep b, consistent with the findings of our established analysis about this planet’s potential metal enrichment (Table 6).

AF Lep b, given that the S/N and wavelength span of this object's spectrophotometry is yet to be improved in the near future. Instead, this test indicates that when retrieving properties for a self-luminous planet or a brown dwarf that is expected to possess clouds, modeling the T–P profiles in terms of the temperature gradient ($d\ln T/d\ln P$) enables the incorporation of the RCE as parameterized priors for the object's thermal structure. These RCE priors can break the degeneracy between clouds and the shape of T–P profiles and lead to a robust characterization of the object's cloud properties.

Another advantage of modeling the atmospheric thermal structure using temperature gradients is that the resulting T–P profiles are inherently smooth. Such smoothness is achieved because the temperature gradient throughout the atmosphere is obtained from the quadratic interpolation of ($d\ln T/d\ln P$) at six input layers (Section 6.1). In retrieval studies that directly fit temperatures at multiple layers (e.g., Line et al. 2015, 2017; Zalesky et al. 2019, 2022; Hood et al. 2023), a "smoothing" hyperparameter is often used to prevent temperature oscillations as a function of pressures (e.g., Equation (5) of Line et al. 2015). Such a hyperparameter is not required when modeling T–P profiles using temperature gradients.

8.4. Implications for Studies of Directly Imaged Exoplanets

Here we list several valuable lessons learned from our work on AF Lep b that may have broader implications for the study of directly imaged exoplanets:

1. Performing end-to-end reduction for the same set of direct imaging data by using different pipelines, along with self-consistently computed covariance matrices, can provide a less biased perspective about the planets' properties (also see Greenbaum et al. 2018; Xuan et al. 2022; Brown-Sevilla et al. 2023; Nasedkin et al. 2023). For AF Lep b, the emission spectra observed and reduced by Mesa et al. (2023) and De Rosa et al. (2023) are distinct from each other. As seen in Figure 11, the retrieval analysis performed for each spectrum leads to different atmospheric properties including the $T_{\rm eff}$, the cloud properties, the presence of disequilibrium chemistry, and tracers of planet formation, such as C/O (also see Table 6). Some of these differences are pipeline-dependent and would be otherwise unknown if only one pipeline were adopted for data reduction.
2. Dynamical mass provides key constraints to the planets' radii and surface gravities, and thereby to other atmospheric properties. When retrieving each spectrum of Mesa et al. (2023) and De Rosa et al. (2023) using default priors, several inferred parameters are very different between the two data sets, including [Fe/H] and $\log(P_{\rm quench})$. However, after incorporating a constrained mass prior based on the dynamical mass, the inferred parameters for these two spectra become consistent. In addition, the surface gravity and metallicity of gas-giant planets and brown dwarfs are often degenerate based on low-resolution spectral analysis (e.g., Burgasser et al. 2006; Leggett et al. 2007; Liu et al. 2007; Burningham et al. 2009; Zhang et al. 2021f). Such degeneracy is also revealed by our retrieval analysis when adopting the default parameter priors (Figure 10). Directly measured dynamical mass can provide informative priors on $\log(g)$, which can retrospectively constrain the objects' atmospheric metallicity.
3. It is useful to contextualize the atmospheric characterization of directly imaged planets using evolution models. These evolution models provide expected ranges of planets' properties based on the objects' dynamical masses, ages, and/or bolometric luminosities. Incorporating these predictions can help suppress the "small-radius problem" that often occurs in retrievals and forward-modeling analyses, thus improving the accuracy of other atmospheric properties.
4. Spectrophotometry with a wide wavelength coverage is essential to constraining the properties of directly imaged planets. In Appendix E, we present nine more retrieval runs of AF Lep b similar to those described in Section 7, but with all $K1/K2/L'$ photometry excluded. Without these photometric data, a large scatter is seen in fitted model spectra with wavelengths beyond 2 μm, which also leads to large uncertainties of the planet's [Fe/H] and C/O.
5. Spectrophotometric monitoring of imaged planets is essential to revealing their atmospheric variability. Dedicated observations and analyses of time-series spectrophotometry will bring new insights into the formation and evolution of gas-giant planets.

9. Summary

AF Lep A+b is a remarkable planetary system hosting a gas-giant planet, AF Lep b, with the lowest dynamical mass among directly imaged exoplanets. In order to investigate the formation pathway of AF Lep b, we have performed an in-depth analysis of the orbital and atmospheric properties of both the star and the planet. Our main findings are summarized below.

1. Using our newly observed high-resolution spectroscopy of AF Lep A, we constrain a uniform set of stellar parameters and elemental abundances including a mass of $1.09 \pm 0.06\,M_{\odot}$ and an iron abundance of -0.27 ± 0.31 dex. Measurements of the stellar C/O are challenged by the fast stellar rotation that causes line broadening and blending of the characteristic C and O features (Section 3).
2. We have updated the orbit and dynamical mass of AF Lep b, by combining published RVs, relative astrometry, and absolute astrometry, as well as the newly determined stellar mass (Section 4). The refined planet's dynamical mass is $2.8^{+0.6}_{-0.5}\,M_{\rm Jup}$, with a semimajor axis of 8.2 au. The architecture of the AF Lep system is consistent with a spin–orbit alignment (or misalignment) as previously suggested (Franson et al. 2023b).
3. Several evolution models are adopted to contextualize the atmospheric properties of AF Lep b using its directly measured dynamical mass and the system's age. All these models predict consistent planet properties, although the hot-start models ($T_{\rm eff} = 610$–680 K, with $\log(L_{\rm bol}/L_{\odot})$ of -5.7 dex to -5.4 dex) suggest slightly hotter effective temperatures and brighter bolometric luminosities than those inferred by cold-start models ($T_{\rm eff} = 480$–600 K, with $\log(L_{\rm bol}/L_{\odot})$ of -6.1 dex to -5.7 dex). The radius of AF Lep b is estimated to span a range of 1.2–1.55 $R_{\rm Jup}$ (Section 5).

4. We have performed chemically consistent retrievals for AF Lep b using `petitRADTRANS` (Sections 6 and 7) and developed a new retrieval approach that can lead to a robust characterization for cloudy self-luminous atmospheres (Section 8.3). Specifically, we incorporate the RCE temperature profiles as parameterized priors on the planet's thermal structure during the retrievals. This novel approach is enabled by constraining the T–P profiles via the temperature gradient ($d\ln T/d\ln P$), a departure from previous studies that solely modeled the temperature.
5. We have analyzed all published emission spectra and photometry of AF Lep b, spanning 0.9–4.2 μm. Multiple runs are conducted using different portions of the planet's spectrophotometry, along with different priors on the planet's mass and radius. These retrievals consistently suggest that AF Lep b likely has a metal-enriched atmosphere ([Fe/H] $>$ 1.0 dex or $Z_{\rm planet}/Z_{\rm star} = 75^{+94}_{-42}$) compared to the metallicity of its host star. Our analysis also determines $T_{\rm eff} \approx 800$ K, $\log(g) \approx 3.7$ dex, and the presence of silicate clouds and disequilibrium chemistry in the atmosphere of AF Lep b.
6. The potential metal enrichment of AF Lep b might be explained by planetesimal accretion, giant impacts, and/or core erosion. The first process also coincides with the presence of a debris disk in the system located at 40–60 au. At its observed orbit, AF Lep b has a sufficient mass to dynamically excite the debris disk, causing planetesimal scattering and bombardment onto the planet's atmosphere (Section 8.1).
7. If AF Lep b formed a few Myr later than its host star, then the planet's retrieved effective temperature and bolometric luminosity would be consistent with predictions of hot-start evolution models. When compared to predictions of cold-start evolution models, our retrieved $T_{\rm eff}$ and $L_{\rm bol}$ appear to be much higher regardless of whether the planet is coeval with the host star or formed 10 Myr later (Section 8.1).
8. If giant impacts and planetary mergers occurred during the evolution history of AF Lep b, these processes might have acted as a mechanism of rejuvenation, by altering the planet's entropy state. In this scenario, the noted discrepancies between the retrieved and evolution-based $T_{\rm eff}$ and $L_{\rm bol}$ of AF Lep b can be potentially resolved.
9. We have refined the spectral type of AF Lep b to L8–T3. Compared to higher-mass brown dwarfs with similar spectral types, AF Lep b has 450–600 K colder $T_{\rm eff}$ and 0.6–0.9 dex fainter $L_{\rm bol}$. These peculiar properties of AF Lep b are likely linked to its very low surface gravity and high atmospheric metallicity. Notably, AF Lep b is the coldest object with suggested evidence of silicate clouds to date (Section 8.2).
10. Our analysis of AF Lep b also leads to several valuable lessons that may have broader implications for the atmospheric study of directly imaged exoplanets. Specifically, we highlight the value of (1) performing end-to-end reduction for the same set of direct imaging data by using different pipelines, (2) measuring the planet's dynamical mass based on orbital monitoring, (3) contextualizing the planet's atmospheric properties by using evolution models, (4) acquiring the planet's spectrophotometry with a broad wavelength coverage, and (5) studying the planet's top-of-atmosphere inhomogeneities based on variability monitoring.

For future work, it is essential to acquire spectrophotometry of AF Lep b with a higher S/N and/or spectral resolution over a broader wavelength range (e.g., VLTI/GRAVITY). Also, consistent reduction procedures should be applied to the existing SPHERE data (from Mesa et al. 2023 and De Rosa et al. 2023) to improve the quality of the emission spectra. These efforts will help improve the accuracy and precision of the inferred atmospheric properties of AF Lep b, allowing for a reassessment of the formation pathway of this remarkable planetary system.

A Zenodo repository at doi:[10.5281/zenodo.8267466] contains the data sets from this work. This includes the Tull spectrum of AF Lep A (Section 2), the stellar parameters of AF Lep A inferred from `isochrones` (Section 3), the AF Lep b orbital analysis (Section 4), the RCE T–P profiles of several sets of forward models (Section 6.2), and a mini-grid of the modeled emission spectroscopy (Section 6.4). In addition, fitted T–P profiles, fitted model spectra, and parameter posteriors from multiple retrieval runs (Section 7) are available.

Acknowledgments

Z.Z. and P.M. thank Michiel Min for the idea of parameterizing the thermal structure using the temperature gradient. Z.Z. thanks Artem Aguichine, William Balmer, Bertram Bitsch, Douglas Lin, Evert Nasedkin, Kazumasa Ohno, and Daniel Thorngren for very helpful discussions. We thank the referee for suggestions that improved the manuscript. Support for this work was provided by NASA through the NASA Hubble Fellowship grant HST-HF2-51522.001-A awarded by the Space Telescope Science Institute, which is operated by the Association of Universities for Research in Astronomy, Inc., for NASA, under contract NAS5-26555. B.P.B. acknowledges support from the National Science Foundation grant AST-1909209, the NASA Exoplanet Research Program grant 20-XRP20_2-0119, and the Alfred P. Sloan Foundation. This work has benefited from the UltracoolSheet at http://bit.ly/UltracoolSheet, maintained by Will Best, Trent Dupuy, Michael Liu, Rob Siverd, and Zhoujian Zhang, and developed from compilations by Dupuy & Liu (2012), Dupuy & Kraus (2013), Liu et al. (2016), and Best et al. (2018, 2021). This work has made use of data from the European Space Agency mission Gaia (https://www.cosmos.esa.int/gaia), processed by the Gaia Data Processing and Analysis Consortium (DPAC, https://www.cosmos.esa.int/web/gaia/dpac/consortium). Funding for the DPAC has been provided by national institutions, in particular the institutions participating in the Gaia Multilateral Agreement.

Facilities: Smith (Tull), Keck:I (HIRES), Keck:II (NIRC2), VLT:Melipal (SPHERE).

Software: `DCR` (Pych 2004), `iSpec` (Blanco-Cuaresma et al. 2014; Blanco-Cuaresma 2019), `BACCHUS` (Masseron et al. 2016), `TURBOSPECTRUM` (Plez 2012), `isochrones` (Morton 2015), `gaiadr3-zero-point` (Lindegren et al. 2021), `orvara` (Brandt et al. 2021), `petitRADTRANS` (Mollière et al. 2019), `petitCODE` (Mollière et al. 2015, 2017), `PyMultiNest` (Buchner et al. 2014), `MultiNest` (Feroz & Hobson 2008; Feroz et al. 2009, 2019), `corner.py` (Foreman-Mackey 2016), Astropy (Astropy Collaboration et al. 2013, 2018), IPython (Pérez & Granger 2007), NumPy (Oliphant 2006), SciPy (Jones et al. 2001), Matplotlib (Hunter 2007).

Appendix A
Literature Comparison for Our Stellar Parameters of AF Lep A

As shown in Figure 16, our inferred mass, iron abundance, effective temperature, surface gravity, and radius for AF Lep A (Table 1) are generally consistent with those determined in the literature. When collecting the literature values, we exclude studies that cataloged or averaged stellar parameters measured by other work.

In this work, M_A is a key parameter for constraining the orbit and dynamical mass of AF Lep b. Several studies have measured slightly higher M_A than our adopted value, including Valenti & Fischer (2005), Takeda et al. (2007), Wright et al. (2011), Kervella et al. (2019), and Pearce et al. (2022); the latter four studies did not measure the stellar [Fe/H]. As detailed below, the different M_A estimates between their work and ours are likely due to the systematic differences of the adopted stellar model spectra and isochrones (with different atomic/molecular line lists), the input photometry (single band versus multiple bands), the assumption about the stellar age, and whether all input parameters are simultaneously or separately constrained by the stellar models.

1. Valenti & Fischer (2005) estimated the bolometric luminosity of AF Lep A via the V-band magnitude with a bolometric correction and derived other stellar parameters by fitting the observed spectrum using the Kurucz (1992) model atmospheres; they then updated the stellar mass by modeling the $L_{\rm bol}$ and $T_{\rm eff}$ via the Yonsei–Yale isochrones (Demarque et al. 2004). Their resulting M_A, $[{\rm Fe/H}]_A$, $T_{\rm eff,A}$, and $\log(g_A)$ are all among the highest (and their derived R_A is among the smallest) in the literature.
2. The analysis of Takeda et al. (2007) is tied to that of Valenti & Fischer (2005). Briefly, Takeda et al. (2007) derived the mass and radius of AF Lep A (along with about 1000 cool stars) by modeling this object's parallax, V-band magnitude, and the Valenti & Fischer (2005) $T_{\rm eff}$, $\log(g)$, and [Fe/H] measurements using the Yale Rotational Evolution Code.

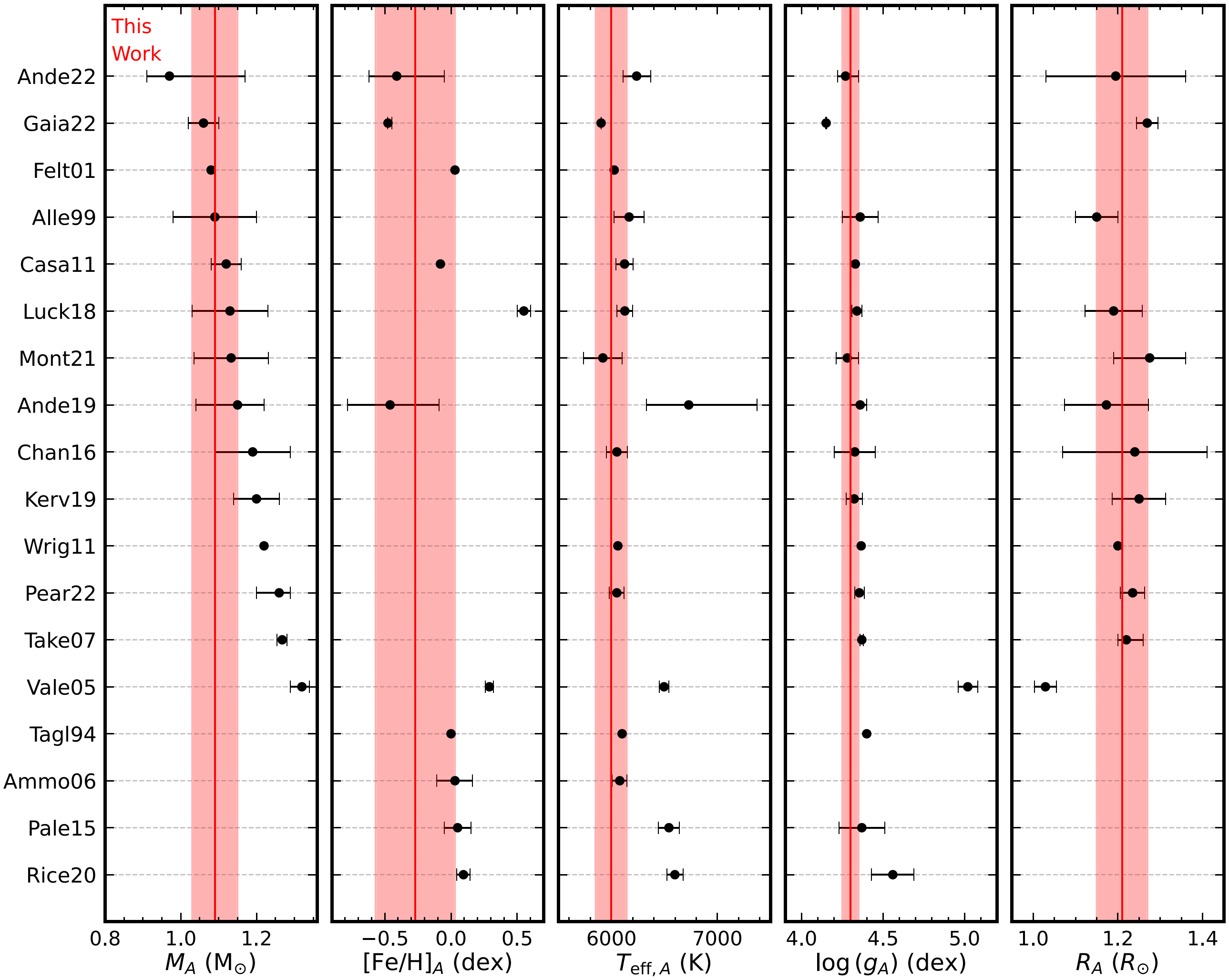

Figure 16. Our measured stellar parameters of AF Lep A (verticle red line with shadow) compared to those in the literature (black; sorted by M_A, and then by $[{\rm Fe/H}]_A$ if M_A is not reported). References for labels shown on the y-axis are as follows. Tagl94: Tagliaferri et al. (1994); Alle99: Allende Prieto & Lambert (1999); Felt01: Feltzing et al. (2001); Vale05: Valenti & Fischer (2005); Ammo06: Ammons et al. (2006); Take07: Takeda et al. (2007); Casa11: Casagrande et al. (2011); Wrig11: Wright et al. (2011); Pale15: Paletou et al. (2015); Chan16: Chandler et al. (2016); Luck18: Luck (2018); Ande19: Anders et al. (2019); Kerv19: Kervella et al. (2019); Rice20: Rice & Brewer (2020); Mont21: Montalto et al. (2021); Ande22: Anders et al. (2022); Gaia22: Gaia Collaboration et al. (2023); Pear22: Pearce et al. (2022).

3. Wright et al. (2011) first estimated a bolometric luminosity based on the V-band magnitude and a bolometric correction guided by the object's $V - K_s$ color. Assuming AF Lep A has a much older age of 1 Gyr (compared to its age of 24 ± 3 Myr), they then used the bolometric luminosity and the Siess et al. (2000) isochrones to derive the stellar M_A, R_A, and $T_{\mathrm{eff,A}}$.
4. Kervella et al. (2019) estimated the radius of AF Lep A using the V-band magnitude, $V - K_s$ color, and parallax. Then they derived M_A by using the Girardi et al. (2000) isochrones.
5. Pearce et al. (2022) determined the effective temperature and bolometric luminosity of AF Lep A by fitting the PHOENIX (Husser et al. 2013) model atmospheres (with a blackbody component to account for the debris disk) to the observed multiband photometry. They then modeled these inferred $T_{\mathrm{eff,A}}$ and $L_{\mathrm{bol,A}}$ using the MIST evolution models to derive M_A.

Appendix B
Parameter Posteriors and Data–Model Comparison of Our Orbit Analysis

In Figure 17, we present the posteriors for masses of AF Lep A and b, as well as the planet's orbital parameters. Figure 18 compares our input observational data with the fitted orbits.

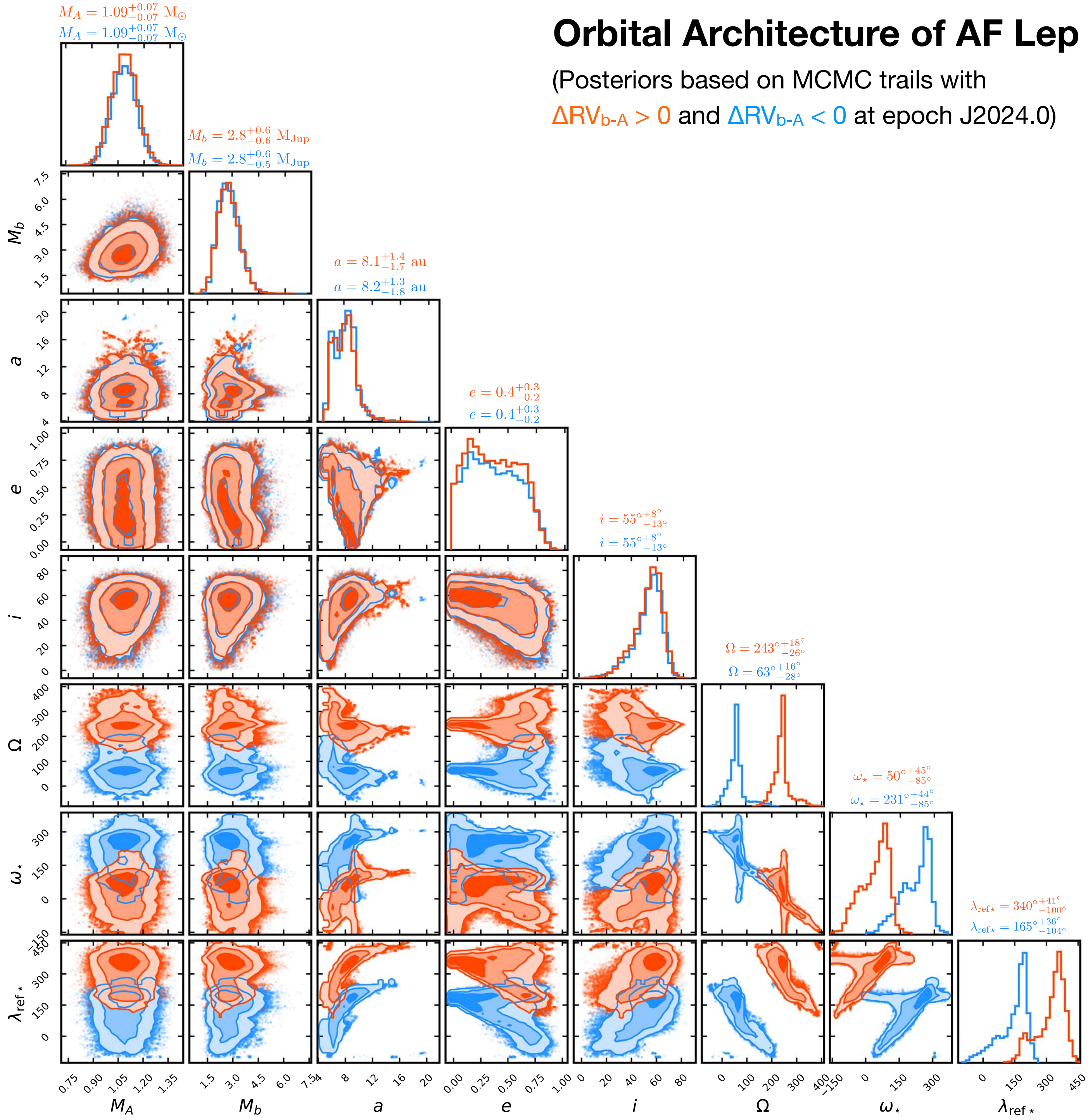

Figure 17. Parameter posteriors for two modes of our derived orbital solution, corresponding to positive (red) and negative (blue) $\Delta RV_{\rm b-A}$ values at epoch J2024.0. The axes of Ω, $\omega_\star$, and $\lambda_{\rm ref,\star}$ extend beyond the nominal range of [0°, 360°) so that each mode of the orbital solution does not split into multiple peaks due to the modulus of 360°.

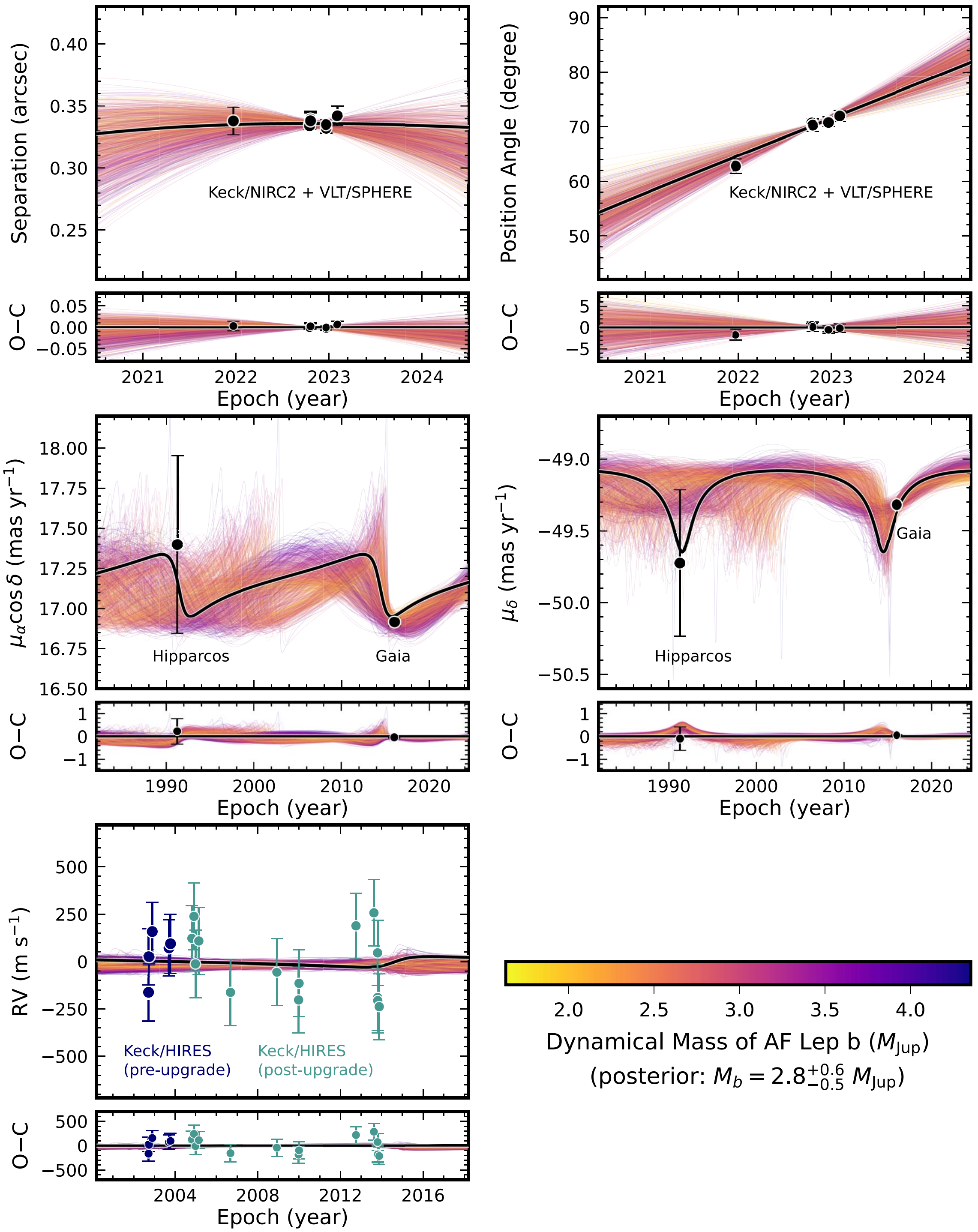

Figure 18. Fitted orbits compared to the observed relative astrometry (top), the absolute astrometry (middle), and the host star's relative RVs (bottom left). In each panel, we present the observed data (top) and residuals (bottom) as filled circles, and the best-fit orbital solution as black solid lines. Predictions of 1000 random orbits are color-coded by the dynamical mass of AF Lep b, estimated to be $2.7^{+0.6}_{-0.5}$ $M_{\rm Jup}$ by our analysis.

Appendix C
Evolution-based Properties of AF Lep b Assuming a Younger Age Than the Host Star

Table 7 presents the physical properties of AF Lep b inferred by various evolution models. Input parameters of this analysis include the directly measured mass ($M = 2.8^{+0.6}_{-0.5}\ M_{\rm Jup}$, Section 4) and an age of 14 ± 3 Myr, which is 10 Myr younger than that of the host star, assuming a slightly later epoch of planet formation.

Table 7
Properties of AF Lep b Based on Evolution Models (Assuming Planet Is 10 Myr Younger Than the Host Star)

Evolution Model	$T_{\rm eff}$ (K)	$\log(L_{\rm bol}/L_\odot)$ (dex)	$\log(g)$ (dex)	R ($R_{\rm Jup}$)
Hot-start Models				
Saumon & Marley (2008): cloudy ($f_{\rm sed} = 2$) and [Fe/H] = 0	754^{+72}_{-55}	$-5.22^{+0.17}_{-0.15}$	$3.56^{+0.08}_{-0.07}$	$1.400^{+0.025}_{-0.022}$
Saumon & Marley (2008): hybrid and [Fe/H] = 0	781^{+106}_{-82}	$-5.20^{+0.24}_{-0.21}$	$3.60^{+0.08}_{-0.07}$	$1.328^{+0.024}_{-0.018}$
Marley et al. (2021): cloudless and [Fe/H] = −0.5	744^{+99}_{-82}	$-5.31^{+0.23}_{-0.21}$	$3.62^{+0.08}_{-0.09}$	$1.288^{+0.018}_{-0.014}$
Marley et al. (2021): cloudless and [Fe/H] = 0	756^{+99}_{-87}	$-5.27^{+0.23}_{-0.22}$	$3.60^{+0.08}_{-0.09}$	$1.312^{+0.022}_{-0.016}$
Marley et al. (2021): cloudless and [Fe/H] = +0.5	767^{+95}_{-85}	$-5.23^{+0.22}_{-0.22}$	$3.58^{+0.08}_{-0.09}$	$1.339^{+0.026}_{-0.020}$
Spiegel & Burrows (2012): cloudless and [Fe/H] = 0	742^{+101}_{-89}	$-5.29^{+0.23}_{-0.23}$	$3.59^{+0.09}_{-0.09}$	$1.329^{+0.023}_{-0.017}$
Spiegel & Burrows (2012): hybrid and [Fe/H] = +0.5	723^{+98}_{-86}	$-5.34^{+0.23}_{-0.23}$	$3.59^{+0.09}_{-0.09}$	$1.329^{+0.023}_{-0.017}$
Phillips et al. (2020): cloudless and [Fe/H] = 0	760^{+99}_{-91}	$-5.26^{+0.23}_{-0.23}$	$3.60^{+0.08}_{-0.09}$	$1.318^{+0.027}_{-0.020}$
Baraffe et al. (2003): cloudless and [Fe/H] = 0	791^{+101}_{-90}	$-5.20^{+0.22}_{-0.22}$	$3.60^{+0.08}_{-0.09}$	$1.317^{+0.023}_{-0.020}$
Cold-start Models				
Marley et al. (2021): cloudless and [Fe/H] = −0.5	665^{+41}_{-44}	$-5.52^{+0.11}_{-0.12}$	$3.62^{+0.09}_{-0.10}$	$1.278^{+0.013}_{-0.010}$
Spiegel & Burrows (2012): cloudless and [Fe/H] = 0	520^{+21}_{-22}	$-5.96^{+0.07}_{-0.08}$	$3.64^{+0.10}_{-0.10}$	$1.253^{+0.012}_{-0.010}$
Spiegel & Burrows (2012): hybrid and [Fe/H] = +0.5	528^{+24}_{-26}	$-5.93^{+0.08}_{-0.09}$	$3.64^{+0.10}_{-0.10}$	$1.253^{+0.012}_{-0.010}$

Appendix D
Retrievals on All $K1/K2/L'$ Photometry with Different Spectroscopic Data Sets and Parameter Priors

Figure 19 presents the results of all retrieval runs that incorporate all the $K1/K2/L'$ photometry, with different sets of spectra and parameter priors. As described in Section 7, the three spectral sets include (1) the Mesa et al. (2023) spectrum, (2) the De Rosa et al. (2023) spectrum, and (3) both spectra. The three sets of parameter priors include (1) the default priors summarized in Table 5, (2) a constrained prior on the planet's mass and default priors for the remaining parameters, and (3) constrained priors on both the planet's mass and radius with default priors for the remaining parameters. Retrievals with constrained priors on both M and R are already shown in Figures 7–9, so Figure 19 presents the results for the remaining six retrieval runs. Median values and confidence intervals of all parameters inferred by these retrievals are summarized in Table 6.

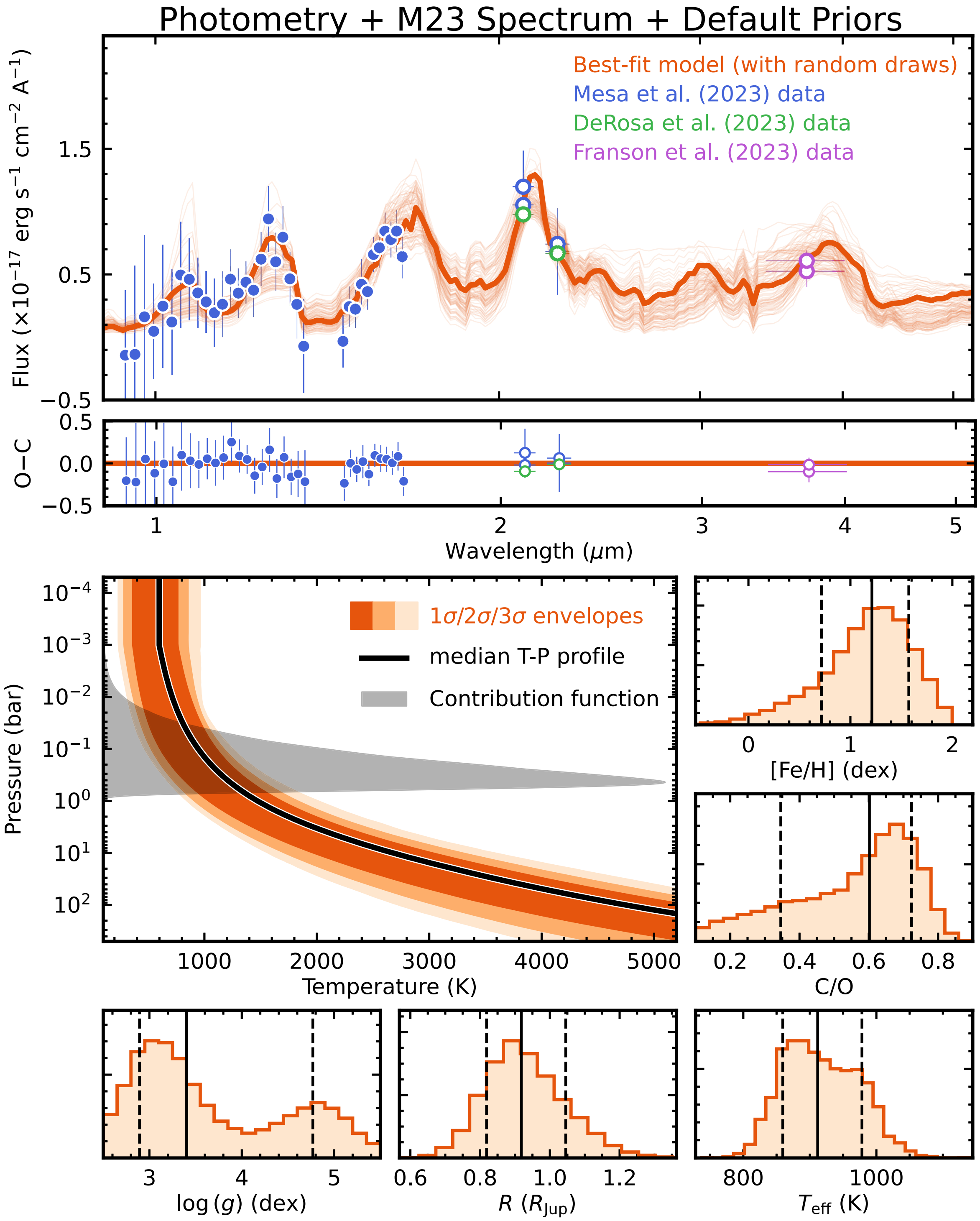

Figure 19. Results of the retrieval analysis on $K1/K2/L'$ photometry and the Mesa et al. (2023) spectrum of AF Lep b, with the default parameter priors listed in Table 5. The format is the same as that of Figure 7.

(The complete figure set (6 images) is available.)

Appendix E
Retrievals on Different Spectroscopic Data Sets and Parameter Priors of AF Lep b, with Photometry Excluded

Figure 20 presents the results of the additional nine retrieval runs that incorporate different sets of spectra and parameter priors (the same as those described in Appendix D), but with all the $K1/K2/L'$ photometry of AF Lep b excluded.

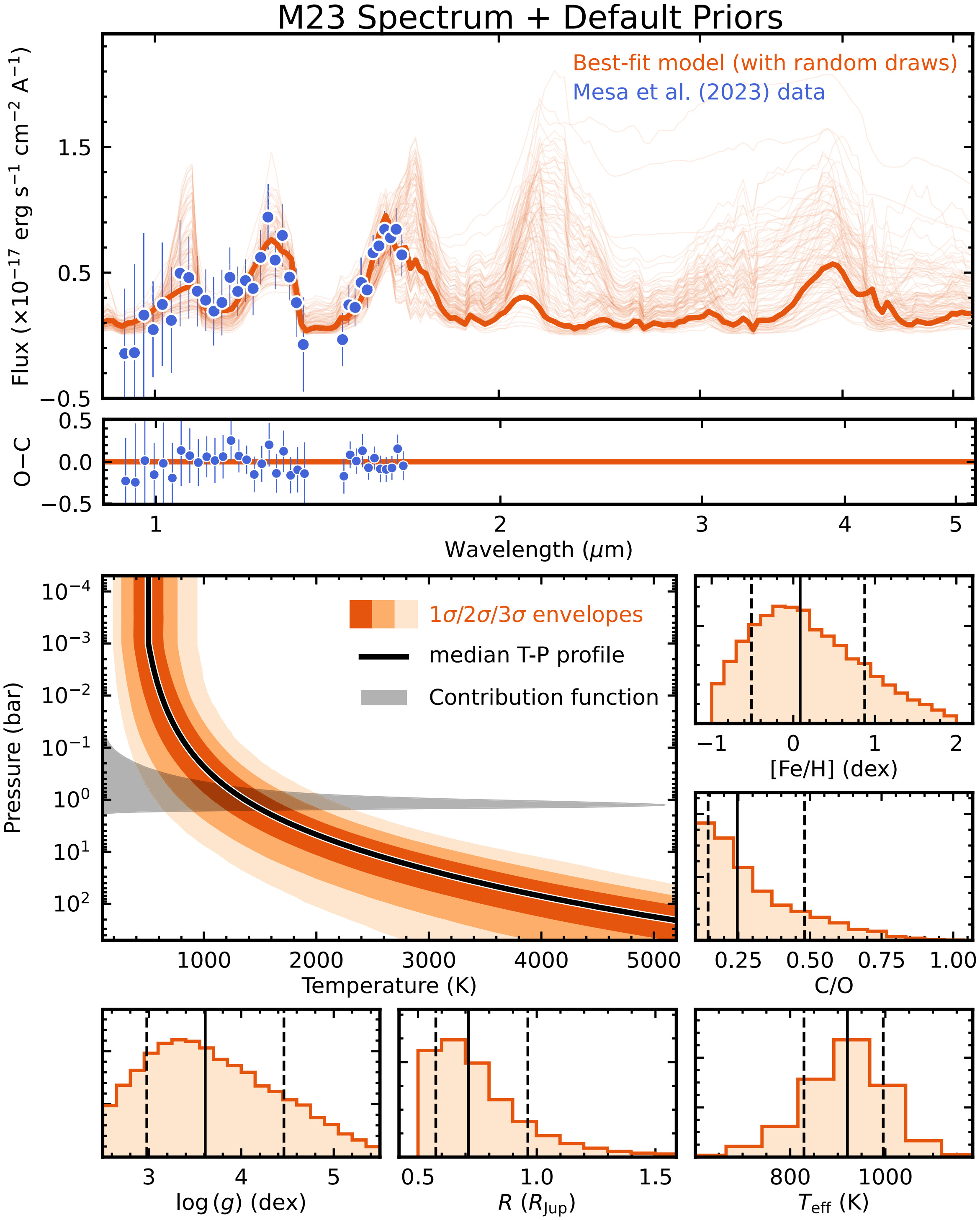

Figure 20. Results of the retrieval analysis on the Mesa et al. (2023) spectrum of AF Lep b, with the default parameter priors listed in Table 5. The format is the same as that of Figure 7.

(The complete figure set (9 images) is available.)

ORCID iDs

Zhoujian Zhang (张周健) https://orcid.org/0000-0002-3726-4881
Paul Mollière https://orcid.org/0000-0003-4096-7067
Keith Hawkins https://orcid.org/0000-0002-1423-2174
Catherine Manea https://orcid.org/0000-0002-0900-6076
Jonathan J. Fortney https://orcid.org/0000-0002-9843-4354
Caroline V. Morley https://orcid.org/0000-0002-4404-0456
Andrew Skemer https://orcid.org/0000-0001-6098-3924
Mark S. Marley https://orcid.org/0000-0002-5251-2943
Brendan P. Bowler https://orcid.org/0000-0003-2649-2288
Aarynn L. Carter https://orcid.org/0000-0001-5365-4815
Kyle Franson https://orcid.org/0000-0003-4557-414X
Zachary G. Maas https://orcid.org/0000-0002-0475-3662
Christopher Sneden https://orcid.org/0000-0002-3456-5929

References

Ackerman, A. S., & Marley, M. S. 2001, ApJ, 556, 872
Ahrer, E.-M., Stevenson, K. B., Mansfield, M., et al. 2023, Natur, 614, 653
Alexander, R., Pascucci, I., Andrews, S., Armitage, P., & Cieza, L. 2014, in Protostars and Planets VI, ed. H. Beuther et al. (Tucson, AZ: Univ. Arizona Press), 475
Alibert, Y., Mousis, O., & Benz, W. 2005, ApJL, 622, L145
Ali-Dib, M., Cumming, A., & Lin, D. N. C. 2022, MNRAS, 509, 1413
Allard, F., Hauschildt, P. H., Alexander, D. R., Tamanai, A., & Schweitzer, A. 2001, ApJ, 556, 357
Allard, F., Homeier, D., & Freytag, B. 2012, RSPTA, 370, 2765
Allard, N. F., Spiegelman, F., & Kielkopf, J. F. 2016, A&A, 589, A21
Allard, N. F., Spiegelman, F., Leininger, T., & Molliere, P. 2019, A&A, 628, A120
Allende Prieto, C., & Lambert, D. L. 1999, A&A, 352, 555
Ammons, S. M., Robinson, S. E., Strader, J., et al. 2006, ApJ, 638, 1004
Anders, F., Khalatyan, A., Chiappini, C., et al. 2019, A&A, 628, A94
Anders, F., Khalatyan, A., Queiroz, A. B. A., et al. 2022, A&A, 658, A91
Anderson, E., & Francis, C. 2012, AstL, 38, 331
Atreya, S. K., Crida, A., Guillot, T., et al. 2016, arXiv:1606.04510
August, P. C., Bean, J. L., Zhang, M., et al. 2023, ApJL, 953, L24
Azzam, A. A. A., Tennyson, J., Yurchenko, S. N., & Naumenko, O. V. 2016, MNRAS, 460, 4063
Astropy Collaboration, Price-Whelan, A. M., Sipőcz, B. M., et al. 2018, AJ, 156, 123
Astropy Collaboration, Robitaille, T. P., Tollerud, E. J., et al. 2013, A&A, 558, A33
Bailer-Jones, C. A. L., Rybizki, J., Fouesneau, M., Demleitner, M., & Andrae, R. 2021, AJ, 161, 147
Baraffe, I., Chabrier, G., Allard, F., & Hauschildt, P. H. 2002, A&A, 382, 563
Baraffe, I., Chabrier, G., Barman, T. S., Allard, F., & Hauschildt, P. H. 2003, A&A, 402, 701
Baraffe, I., Homeier, D., Allard, F., & Chabrier, G. 2015, A&A, 577, A42
Beatty, T. G., Morley, C. V., Curtis, J. L., et al. 2018, AJ, 156, 168
Bell, C. P. M., Mamajek, E. E., & Naylor, T. 2015, MNRAS, 454, 593
Best, W. M. J., Dupuy, T. J., Liu, M. C., Siverd, R. J., & Zhang, Z. 2020b, The UltracoolSheet: Photometry, Astrometry, Spectroscopy, and Multiplicity for 3000+ Ultracool Dwarfs and Imaged Exoplanets, v1.0.1, Zenodo, doi:10.5281/zenodo.4169085
Best, W. M. J., Liu, M. C., Magnier, E. A., & Dupuy, T. J. 2021, AJ, 161, 42
Best, W. M. J., Magnier, E. A., Liu, M. C., et al. 2018, ApJS, 234, 1
Biersteker, J. B., & Schlichting, H. E. 2019, MNRAS, 485, 4454
Blanco-Cuaresma, S. 2019, MNRAS, 486, 2075
Blanco-Cuaresma, S., Soubiran, C., Heiter, U., & Jofré, P. 2014, A&A, 569, A111
Boley, A. C., & Durisen, R. H. 2010, ApJ, 724, 618
Bonavita, M., Fontanive, C., Gratton, R., et al. 2022, MNRAS, 513, 5588
Borysow, A. 2002, A&A, 390, 779
Borysow, A., & Frommhold, L. 1989, ApJ, 341, 549
Borysow, A., Frommhold, L., & Moraldi, M. 1989, ApJ, 336, 495
Borysow, A., Jorgensen, U. G., & Fu, Y. 2001, JQSRT, 68, 235
Borysow, J., Frommhold, L., & Birnbaum, G. 1988, ApJ, 326, 509
Boucher, A., Lafreniére, D., Pelletier, S., et al. 2023, MNRAS, 522, 5062
Bowler, B. P., Endl, M., Cochran, W. D., et al. 2021, ApJL, 913, L26
Bowler, B. P., Tran, Q. H., Zhang, Z., et al. 2023, AJ, 165, 164
Brandt, T. D. 2018, ApJS, 239, 31
Brandt, T. D. 2021, ApJS, 254, 42
Brandt, T. D., Dupuy, T. J., Bowler, B. P., et al. 2020, AJ, 160, 196
Brandt, T. D., Dupuy, T. J., Li, Y., et al. 2021, AJ, 162, 186
Brogi, M., Emeka-Okafor, V., Line, M. R., et al. 2023, AJ, 165, 91
Brown-Sevilla, S. B., Maire, A. L., Mollière, P., et al. 2023, A&A, 673, A98
Brown-Sevilla, S. B., Maire, A. L., Mollière, P., et al. 2023, A&A, 673, A98
Buchner, J., Georgakakis, A., Nandra, K., et al. 2014, A&A, 564, A125
Burgasser, A. J., Burrows, A., & Kirkpatrick, J. D. 2006, ApJ, 639, 1095
Burningham, B., Faherty, J. K., Gonzales, E. C., et al. 2021, MNRAS, 506, 1944
Burningham, B., Marley, M. S., Line, M. R., et al. 2017, MNRAS, 470, 1177
Burningham, B., Pinfield, D. J., Leggett, S. K., et al. 2009, MNRAS, 395, 1237
Burrows, A., Marley, M., Hubbard, W. B., et al. 1997, ApJ, 491, 856
Butler, R. P., Vogt, S. S., Laughlin, G., et al. 2017, AJ, 153, 208
Casagrande, L., Schönrich, R., Asplund, M., et al. 2011, A&A, 530, A138
Chabrier, G., Baraffe, I., Allard, F., & Hauschildt, P. 2000, ApJ, 542, 464
Chan, Y. M., & Dalgarno, A. 1965, PPS, 85, 227
Chandler, C. O., McDonald, I., & Kane, S. R. 2016, AJ, 151, 59
Changeat, Q., Edwards, B., Al-Refaie, A. F., et al. 2022, ApJS, 260, 3
Charnay, B., Bézard, B., Baudino, J. L., et al. 2018, ApJ, 854, 172
Choi, J., Dotter, A., Conroy, C., et al. 2016, ApJ, 823, 102
Claudi, R. U., Turatto, M., Gratton, R. G., et al. 2008, Proc. SPIE, 7014, 70143E
Coles, P. A., Yurchenko, S. N., & Tennyson, J. 2019, MNRAS, 490, 4638
Cridland, A. J., van Dishoeck, E. F., Alessi, M., & Pudritz, R. E. 2020, A&A, 642, A229
Currie, T., Brandt, G. M., Brandt, T. D., et al. 2023, Sci, 380, 198
Cushing, M. C., Roellig, T. L., Marley, M. S., et al. 2006, ApJ, 648, 614
Cutri, R. M., Skrutskie, M. F., van Dyk, S., et al. 2003, yCat, II/246
Cutri, R. M., Wright, E. L., Conrow, T., et al. 2021, yCat, II/328
Dahn, C. C., Harris, H. C., Vrba, F. J., et al. 2002, AJ, 124, 1170
Dalgarno, A., & Williams, D. A. 1962, ApJ, 136, 690
De Rosa, R. J., Nielsen, E. L., Wahhaj, Z., et al. 2023, A&A, 672, A94
Debras, F., & Chabrier, G. 2019, ApJ, 872, 100
Delorme, P., Meunier, N., Albert, D., et al. 2017, in SF2A-2017: Proc. Annual Meeting of the French Society of Astronomy and Astrophysics, ed. C. Reylé et al. (Paris: SF2A), 347
Demarque, P., Woo, J.-H., Kim, Y.-C., & Yi, S. K. 2004, ApJS, 155, 667
Dohlen, K., Langlois, M., Saisse, M., et al. 2008, Proc. SPIE, 7014, 70143L
Dotter, A. 2016, ApJS, 222, 8
Drazkowska, J., Bitsch, B., Lambrechts, M., et al. 2022, in ASP Conf. Ser. 534, Protostars and Planets VII, ed. S. Inutsuka et al. (San Francisco, CA: ASP), 717
Dupuy, T. J., & Kraus, A. L. 2013, Sci, 341, 1492
Dupuy, T. J., & Liu, M. C. 2012, ApJS, 201, 19
Dupuy, T. J., Liu, M. C., & Ireland, M. J. 2009, ApJ, 692, 729
Do, Ó. C. R., O'Neil, K. K., Konopacky, Q. M., et al. 2023, AJ, 166, 48
El-Badry, K., Rix, H.-W., & Heintz, T. M. 2021, MNRAS, 506, 2269
Emsenhuber, A., Mordasini, C., Burn, R., et al. 2021, A&A, 656, A69
Fabricius, C., Luri, X., Arenou, F., et al. 2021, A&A, 649, A5
Feltzing, S., Holmberg, J., & Hurley, J. R. 2001, A&A, 377, 911
Feroz, F., & Hobson, M. P. 2008, MNRAS, 384, 449
Feroz, F., Hobson, M. P., & Bridges, M. 2009, MNRAS, 398, 1601
Feroz, F., Hobson, M. P., Cameron, E., & Pettitt, A. N. 2019, OJAp, 2, 10
Filippazzo, J. C., Rice, E. L., Faherty, J., et al. 2015, ApJ, 810, 158
Finnerty, L., Schofield, T., Sappey, B., et al. 2023, AJ, 166, 31
Fletcher, L. N., Orton, G. S., Teanby, N. A., Irwin, P. G. J., & Bjoraker, G. L. 2009, Icar, 199, 351
Foreman-Mackey, D. 2016, JOSS, 1, 24
Foreman-Mackey, D., Hogg, D. W., Lang, D., & Goodman, J. 2013, PASP, 125, 306
Fortney, J. J., Marley, M. S., Saumon, D., & Lodders, K. 2008, ApJ, 683, 1104
Fortney, J. J., & Nettelmann, N. 2010, SSRv, 152, 423
Fouesneau, M., Andrae, R., Dharmawardena, T., et al. 2022, A&A, 662, A125
Franson, K., Bowler, B. P., Bonavita, M., et al. 2023a, AJ, 165, 39
Franson, K., Bowler, B. P., Zhou, Y., et al. 2023b, ApJL, 950, L19
Frelikh, R., Jang, H., Murray-Clay, R. A., & Petrovich, C. 2019, ApJL, 884, L47
Fu, G., Sing, D. K., Lothringer, J. D., et al. 2022, ApJL, 925, L3
Gaarn, J., Burningham, B., Faherty, J. K., et al. 2023, MNRAS, 521, 5761
Gao, P., Thorngren, D. P., Lee, E. K. H., et al. 2020, NatAs, 4, 951
Ginzburg, S., & Chiang, E. 2020, MNRAS, 498, 680
Girardi, L., Bressan, A., Bertelli, G., & Chiosi, C. 2000, A&AS, 141, 371
Gizis, J. E., Faherty, J. K., Liu, M. C., et al. 2012, AJ, 144, 94
Glebocki, R., & Gnacinski, P. 2005, yCat, III/244

Golimowski, D. A., Leggett, S. K., Marley, M. S., et al. 2004, AJ, 127, 3516
Gonzales, E. C., Burningham, B., Faherty, J. K., et al. 2020, ApJ, 905, 46
Gonzales, E. C., Burningham, B., Faherty, J. K., et al. 2021, ApJ, 923, 19
Gonzales, E. C., Burningham, B., Faherty, J. K., et al. 2022, ApJ, 938, 56
Gray, R. O., Corbally, C. J., Garrison, R. F., et al. 2006, AJ, 132, 161
Greenbaum, A. Z., Pueyo, L., Ruffio, J.-B., et al. 2018, AJ, 155, 226
Guillot, T., & Gladman, B. 2000, in ASP Conf. Ser. 219, Disks, Planetesimals, and Planets, ed. G. Garzón et al. (San Francisco, CA: ASP), 475
Gustafsson, B., Edvardsson, B., Eriksson, K., et al. 2008, A&A, 486, 951
Gaia Collaboration, Brown, A. G. A., Vallenari, A., et al. 2018, A&A, 616, A1
GRAVITY Collaboration, Nowak, M., Lacour, S., et al. 2020, A&A, 633, A110
Gaia Collaboration, Prusti, T., de Bruijne, J. H. J., et al. 2016, A&A, 595, A1
Gaia Collaboration, Vallenari, A., Brown, A. G. A., et al. 2023, A&A, 674, A1
Hargreaves, R. J., Gordon, I. E., Rey, M., et al. 2020, ApJS, 247, 55
Hawkins, K., Lucey, M., & Curtis, J. 2020, MNRAS, 496, 2422
Heiter, U., Lind, K., Bergemann, M., et al. 2021, A&A, 645, A106
Helled, R., Anderson, J. D., Podolak, M., & Schubert, G. 2011, ApJ, 726, 15
Helled, R., & Bodenheimer, P. 2010, Icar, 207, 503
Helled, R., & Bodenheimer, P. 2014, ApJ, 789, 69
Helled, R., Bodenheimer, P., Podolak, M., et al. 2014, in Protostars and Planets VI, ed. H. Beuther et al. (Tucson, AZ: Univ. Arizona Press), 643
Helled, R., Podolak, M., & Kovetz, A. 2006, Icar, 185, 64
Helled, R., & Schubert, G. 2009, ApJ, 697, 1256
Hoch, K. K. W., Konopacky, Q. M., Theissen, C. A., et al. 2023, AJ, 166, 85
Høg, E., Fabricius, C., Makarov, V. V., et al. 2000, A&A, 355, L27
Hood, C. E., Fortney, J. J., Line, M. R., & Faherty, J. K. 2023, ApJ, 953, 170
Hunter, J. D. 2007, CSE, 9, 90
Husser, T. O., Wende-von Berg, S., Dreizler, S., et al. 2013, A&A, 553, A6
Järvinen, S. P., Arlt, R., Hackman, T., et al. 2015, A&A, 574, A25
Jones, E., Oliphant, T., Peterson, P., et al. 2001, SciPy: Open source scientific tools for Python, http://www.scipy.org/
Karalidi, T., Marley, M., Fortney, J. J., et al. 2021, ApJ, 923, 269
Kervella, P., Arenou, F., Mignard, F., & Thévenin, F. 2019, A&A, 623, A72
Kervella, P., Arenou, F., & Thévenin, F. 2022, A&A, 657, A7
Kirkpatrick, J. D., Gelino, C. R., Faherty, J. K., et al. 2021, ApJS, 253, 7
Konopacky, Q. M., Barman, T. S., Macintosh, B. A., & Marois, C. 2013, Sci, 339, 1398
Kurucz, R. L. 1992, in Proc. IAU Symp. 149, The Stellar Populations of Galaxies, ed. B. Barbuy & A. Renzini (Dordrecht: Kluwer), 225
Kurucz, R. L. 1993, Kurucz CD-ROM (Cambridge, MA: Smithsonian Astrophysical Observatory)
Kuzuhara, M., Currie, T., Takarada, T., et al. 2022, ApJL, 934, L18
Lacy, B., & Burrows, A. 2023, ApJ, 950, 8
Lavie, B., Mendonça, J. M., Mordasini, C., et al. 2017, AJ, 154, 91
Leconte, J. 2018, ApJL, 853, L30
Leggett, S. K., Marley, M. S., Freedman, R., et al. 2007, ApJ, 667, 537
Li, S. L., Agnor, C. B., & Lin, D. N. C. 2010, ApJ, 720, 1161
Lin, D. N. C., & Ida, S. 1997, ApJ, 477, 781
Lindegren, L., Bastian, U., Biermann, M., et al. 2021, A&A, 649, A4
Line, M. R., Brogi, M., Bean, J. L., et al. 2021, Natur, 598, 580
Line, M. R., Marley, M. S., Liu, M. C., et al. 2017, ApJ, 848, 83
Line, M. R., Teske, J., Burningham, B., Fortney, J. J., & Marley, M. S. 2015, ApJ, 807, 183
Liu, M. C., Dupuy, T. J., & Allers, K. N. 2016, ApJ, 833, 96
Liu, M. C., Leggett, S. K., & Chiu, K. 2007, ApJ, 660, 1507
Liu, M. C., Magnier, E. A., Deacon, N. R., et al. 2013, ApJL, 777, L20
Liu, S.-F., Agnor, C. B., Lin, D. N. C., & Li, S.-L. 2015, MNRAS, 446, 1685
Liu, S.-F., Hori, Y., Müller, S., et al. 2019, Natur, 572, 355
Lodders, K., & Fegley, B. 2006, in Astrophysics Update 2, ed. J. W. Mason (Chichester: Praxis), 1
Lothringer, J. D., Rustamkulov, Z., Sing, D. K., et al. 2021, ApJ, 914, 12
Luck, R. E. 2018, AJ, 155, 111
Lueber, A., Kitzmann, D., Bowler, B. P., Burgasser, A. J., & Heng, K. 2022, ApJ, 930, 136
Lunine, J. I., Hubbard, W. B., & Marley, M. S. 1986, ApJ, 310, 238
MacDonald, R. J., & Batalha, N. E. 2023, RNAAS, 7, 54
Madhusudhan, N., Amin, M. A., & Kennedy, G. M. 2014, ApJL, 794, L12
Madhusudhan, N., Bitsch, B., Johansen, A., & Eriksson, L. 2017, MNRAS, 469, 4102
Maíz Apellániz, J., & Weiler, M. 2018, A&A, 619, A180
Mamajek, E. E. 2009, in AIP Conf. Ser. 1158, Exoplanets and Disks: Their Formation and Diversity, ed. T. Usuda, M. Tamura, & M. Ishii (Melville, NY: AIP), 3
Marley, M. S., Fortney, J., Seager, S., & Barman, T. 2007a, in Protostars and Planets V, ed. B. Reipurth, D. Jewitt, & K. Keil (Tucson, AZ: Univ. Arizona Press), 733
Marley, M. S., Fortney, J. J., Hubickyj, O., Bodenheimer, P., & Lissauer, J. J. 2007b, ApJ, 655, 541
Marley, M. S., Gómez, P., & Podolak, M. 1995, JGR, 100, 23349
Marley, M. S., & Robinson, T. D. 2015, ARA&A, 53, 279
Marley, M. S., Saumon, D., Cushing, M., et al. 2012, ApJ, 754, 135
Marley, M. S., Saumon, D., Visscher, C., et al. 2021, ApJ, 920, 85
Marley, M. S., Seager, S., Saumon, D., et al. 2002, ApJ, 568, 335
Marsden, S. C., Petit, P., Jeffers, S. V., et al. 2014, MNRAS, 444, 3517
Masseron, T., Merle, T., & Hawkins, K., 2016 BACCHUS: Brussels Automatic Code for Characterizing High accUracy Spectra, Astrophysics Source Code Library, ascl:1605.004
Masseron, T., Plez, B., Van Eck, S., et al. 2014, A&A, 571, A47
McQuillan, A., Mazeh, T., & Aigrain, S. 2014, ApJS, 211, 24
Mesa, D., Gratton, R., Kervella, P., et al. 2023, A&A, 672, A93
Miles, B. E., Biller, B. A., Patapis, P., et al. 2023, ApJL, 946, L6
Miller, N., & Fortney, J. J. 2011, ApJL, 736, L29
Mollière, P., Molyarova, T., Bitsch, B., et al. 2022, ApJ, 934, 74
Mollière, P., Stolker, T., Lacour, S., et al. 2020, A&A, 640, A131
Mollière, P., van Boekel, R., Bouwman, J., et al. 2017, A&A, 600, A10
Mollière, P., van Boekel, R., Dullemond, C., Henning, T., & Mordasini, C. 2015, ApJ, 813, 47
Mollière, P., Wardenier, J. P., van Boekel, R., et al. 2019, A&A, 627, A67
Montalto, M., Piotto, G., Marrese, P. M., et al. 2021, A&A, 653, A98
Mordasini, C., Klahr, H., Alibert, Y., Miller, N., & Henning, T. 2014, A&A, 566, A141
Mordasini, C., Marleau, G. D., & Mollière, P. 2017, A&A, 608, A72
Morley, C. V., Fortney, J. J., Marley, M. S., et al. 2012, ApJ, 756, 172
Morton, T. D., 2015 isochrones: Stellar model grid package, Astrophysics Source Code Library, ascl:1503.010
Moses, J. I., Tremblin, P., Venot, O., & Miguel, Y. 2022, ExA, 53, 279
Mousis, O., Lunine, J. I., & Aguichine, A. 2021, ApJL, 918, L23
Mukherjee, S., Batalha, N. E., Fortney, J. J., & Marley, M. S. 2023, ApJ, 942, 71
Mukherjee, S., Fortney, J. J., Batalha, N. E., et al. 2022, ApJ, 938, 107
Nasedkin, E., Mollière, P., Wang, J., et al. 2023, arXiv:2308.01343
Nielsen, E. L., De Rosa, R. J., Macintosh, B., et al. 2019, AJ, 158, 13
Nielsen, E. L., Rosa, R. J. D., Rameau, J., et al. 2017, AJ, 154, 218
Öberg, K. I., Murray-Clay, R., & Bergin, E. A. 2011, ApJL, 743, L16
Ohno, K., & Fortney, J. J. 2022, arXiv:2211.16877
Ohno, K., & Fortney, J. J. 2023, ApJ, 946, 18
Oliphant, T. 2006, NumPy: A guide to NumPy (USA: Trelgol Publishing), http://www.numpy.org/
Owen, T., Mahaffy, P., Niemann, H. B., et al. 1999, Natur, 402, 269
Paletou, F., Böhm, T., Watson, V., & Trouilhet, J. F. 2015, A&A, 573, A67
Pawellek, N., Wyatt, M., Matrà, L., Kennedy, G., & Yelverton6, B. 2021, MNRAS, 502, 5390
Pearce, L. A., Kraus, A. L., Dupuy, T. J., et al. 2020, ApJ, 894, 115
Pearce, T. D., Launhardt, R., Ostermann, R., et al. 2022, A&A, 659, A135
Pérez, F., & Granger, B. E. 2007, CSE, 9, 21
Phillips, M. W., Tremblin, P., Baraffe, I., et al. 2020, A&A, 637, A38
Piette, A. A. A., & Madhusudhan, N. 2020, MNRAS, 497, 5136
Piso, A.-M. A., Pegues, J., & Öberg, K. I. 2016, ApJ, 833, 203
Plez, B., 2012 Turbospectrum: Code for spectral synthesis, Astrophysics Source Code Library, ascl:1205.004
Polyansky, O. L., Kyuberis, A. A., Zobov, N. F., et al. 2018, MNRAS, 480, 2597
Pych, W. 2004, PASP, 116, 148
Radigan, J., Lafrenière, D., Jayawardhana, R., & Artigau, E. 2014, ApJ, 793, 75
Rajan, A., Rameau, J., De Rosa, R. J., et al. 2017, AJ, 154, 10
Rice, M., & Brewer, J. M. 2020, ApJ, 898, 119
Richard, C., Gordon, I. E., Rothman, L. S., et al. 2012, JQSRT, 113, 1276
Rothman, L. S., Gordon, I. E., Barber, R. J., et al. 2010, JQSRT, 111, 2139
Ruffio, J.-B., Konopacky, Q. M., Barman, T., et al. 2021, AJ, 162, 290
Sahlmann, J., Ségransan, D., Queloz, D., & Udry, S. 2011, in IAU Symp. 276, The Astrophysics of Planetary Systems: Formation, Structure, and Dynamical Evolution, ed. A. Sozzetti, M. G. Lattanzi, & A. P. Boss (Cambridge: Cambridge Univ. Press), 117
Samland, M., Mollière, P., Bonnefoy, M., et al. 2017, A&A, 603, A57
Santos, N. C., Adibekyan, V., Figueira, P., et al. 2017, A&A, 603, A30
Saumon, D., & Marley, M. S. 2008, ApJ, 689, 1327
Schlafly, E. F., & Finkbeiner, D. P. 2011, ApJ, 737, 103
Schlaufman, K. C. 2018, ApJ, 853, 37

Schneider, A. C., Cushing, M. C., Kirkpatrick, J. D., et al. 2014, AJ, 147, 34
Schneider, A. D., & Bitsch, B. 2021a, A&A, 654, A71
Schneider, A. D., & Bitsch, B. 2021b, A&A, 654, A72
Schröder, C., Reiners, A., & Schmitt, J. H. M. M. 2009, A&A, 493, 1099
Siess, L., Dufour, E., & Forestini, M. 2000, A&A, 358, 593
Skemer, A. J., Morley, C. V., Zimmerman, N. T., et al. 2016, ApJ, 817, 166
Sousa-Silva, C., Al-Refaie, A. F., Tennyson, J., & Yurchenko, S. N. 2015, MNRAS, 446, 2337
Spiegel, D. S., & Burrows, A. 2012, ApJ, 745, 174
Suárez, G., & Metchev, S. 2022, MNRAS, 513, 5701
Tagliaferri, G., Cutispoto, G., Pallavicini, R., Randich, S., & Pasquini, L. 1994, A&A, 285, 272
Takeda, G., Ford, E. B., Sills, A., et al. 2007, ApJS, 168, 297
Tayar, J., Claytor, Z. R., Huber, D., & van Saders, J. 2022, ApJ, 927, 31
Teske, J. K., Thorngren, D., Fortney, J. J., Hinkel, N., & Brewer, J. M. 2019, AJ, 158, 239
Thorngren, D., & Fortney, J. J. 2019, ApJL, 874, L31
Thorngren, D. P., Fortney, J. J., Murray-Clay, R. A., & Lopez, E. D. 2016, ApJ, 831, 64
Tremblin, P., Amundsen, D. S., Chabrier, G., et al. 2016, ApJL, 817, L19
Tremblin, P., Padioleau, T., Phillips, M. W., et al. 2019, ApJ, 876, 144
Tsuji, T., Ohnaka, K., Aoki, W., & Nakajima, T. 1996, A&A, 308, L29
Valenti, J. A., & Fischer, D. A. 2005, ApJS, 159, 141
Vos, J. M., Biller, B. A., Bonavita, M., et al. 2019, MNRAS, 483, 480
Vos, J. M., Faherty, J. K., Gagné, J., et al. 2022, ApJ, 924, 68
Vousden, W. D., Farr, W. M., & Mandel, I. 2016, MNRAS, 455, 1919
Wahl, S. M., Hubbard, W. B., Militzer, B., et al. 2017, GeoRL, 44, 4649
Wang, J., Kolecki, J. R., Ruffio, J.-B., et al. 2022, AJ, 163, 189
Wang, J., Wang, J. J., Ma, B., et al. 2020, AJ, 160, 150
Wang, J., Wang, J. J., Ruffio, J.-B., et al. 2023, AJ, 165, 4
Wang, J. J., Ruffio, J.-B., De Rosa, R. J., et al., 2015 pyKLIP: PSF Subtraction for Exoplanets and Disks, Astrophysics Source Code Library, ascl:1506.001
Wende, S., Reiners, A., Seifahrt, A., & Bernath, P. F. 2010, A&A, 523, A58
White, R. J., Gabor, J. M., & Hillenbrand, L. A. 2007, AJ, 133, 2524
Whiteford, N., Glasse, A., Chubb, K. L., et al. 2023, MNRAS, 525, 1375
Williams, J. P., & Cieza, L. A. 2011, ARA&A, 49, 67
Wong, M. H., Mahaffy, P. R., Atreya, S. K., Niemann, H. B., & Owen, T. C. 2004, Icar, 171, 153
Wright, N. J., Drake, J. J., Mamajek, E. E., & Henry, G. W. 2011, ApJ, 743, 48
Xuan, J. W., Wang, J., Ruffio, J.-B., et al. 2022, ApJ, 937, 54
Yurchenko, S. N., Mellor, T. M., Freedman, R. S., & Tennyson, J. 2020, MNRAS, 496, 5282
Zahnle, K. J., & Marley, M. S. 2014, ApJ, 797, 41
Zalesky, J. A., Line, M. R., Schneider, A. C., & Patience, J. 2019, ApJ, 877, 24
Zalesky, J. A., Saboi, K., Line, M. R., et al. 2022, ApJ, 936, 44
Zhang, Y., Snellen, I. A. G., & Mollière, P. 2021a, A&A, 656, A76
Zhang, Y., Snellen, I. A. G., Bohn, A. J., et al. 2021b, Natur, 595, 370
Zhang, Z., Liu, M. C., Best, W. M. J., Dupuy, T. J., & Siverd, R. J. 2021c, ApJ, 911, 7
Zhang, Z., Liu, M. C., Claytor, Z. R., et al. 2021d, ApJL, 916, L11
Zhang, Z., Liu, M. C., Marley, M. S., Line, M. R., & Best, W. M. J. 2021e, ApJ, 916, 53
Zhang, Z., Liu, M. C., Marley, M. S., Line, M. R., & Best, W. M. J. 2021f, ApJ, 921, 95
Zhang, Z., Bowler, B. P., Dupuy, T. J., et al. 2023, AJ, 165, 73
Zhang, Z., Liu, M. C., Hermes, J. J., et al. 2020, ApJ, 891, 171
Zhou, J.-L., & Lin, D. N. C. 2007, ApJ, 666, 447
Zhou, Y., Apai, D., Schneider, G. H., Marley, M. S., & Showman, A. P. 2016, ApJ, 818, 176
Zhou, Y., Bowler, B. P., Apai, D., et al. 2022, AJ, 164, 239
Zinn, J. C. 2021, AJ, 161, 214
Zúñiga-Fernández, S., Bayo, A., Elliott, P., et al. 2021, A&A, 645, A30